NMR Structural Studies of Fatty Acid-Binding Proteins

by

Fouad Francis

A dissertation submitted to the Graduate Faculty in Biochemistry in partial fulfillment in the requirements for the degree of the Doctor of Philosophy, The City University of New York

2007

ProQuest Information and Learning Company
300 North Zeeb Road
P.O. Box 1346
Ann Arbor, MI 48106-1346

This manuscript has been read and accepted by the Graduate Faculty in Biochemistry in satisfaction of the dissertation requirement for the degree of Doctor of Philosophy.

4/25/2007 — Ruth Stark

Date — Dr. Ruth Stark
Chair of Examining Committee

4/20/2007 — Lesley Davenport

Date — Dr. Lesley Davenport
Executive Officer

Dr. Fred Naider — Fred Naider

Dr. Judith Storch — Judith Storch

Dr. Themis Lazaridis — Themis Lazaridis

Dr. Ranajeet Ghose — Ranajeet Ghose

Supervisory Committee

THE CITY UNIVERSITY OF NEW YORK

Abstract

NMR Structural Studies of Fatty Acid-Binding Proteins

By

Fouad Francis

Mentor: Prof. Ruth Stark

Solution-state NMR has been used to assess the binding of L-FABP to various ligands that differ in size, chain length, and hydrophobicity. ^{15}N HSQC NMR spectra of holo-L-FABPs containing two ligand equivalents display large chemical shift perturbations for long-chain fatty acids such as oleate, palmitate, eicosapentaenoate, as well as lysophosphatidylcholine, when compared with the unliganded (apo) protein. Similar perturbation patterns for oleate, palmitate, and lysophosphatidylcholine, suggest that binding of these ligands occurs in analogous regions within the binding cavity of L-FABP. However, a difference in the chemical shift perturbation for eicosapentaenoate residues suggests a different binding orientation. By contrast, the short-chain fatty acid caprylate causes a more modest perturbation primarily in the portal region, supporting a shallow interaction with respect to the cavity and yielding K_d values of 0.3-2.2 mM measured at various protein sites. Addition of both heme and protoporphyrin, previously reported as strongly binding ligands for L-FABP, causes protein denaturation. However, heme denaturation can be reversed by the addition of oleate. Absence of any changes in the HSQC spectra of apo-LFABP with water-insoluble cholesterol and observance of considerable changes with water-soluble deoxycholate (bile salt) suggests an electrostatic requirement for sterol binding.

Introducing residual dipolar couplings (RDC) as angular constraints achieves refinement of the solution-state tertiary structure of apo-L-FABP, improving values of backbone RMSD from 1.04 to 0.72 for apo-L-FABP . In addition, a better apo-L-FABP structure refined with RDCs is indicated by a decrease in the percentage of disallowed regions (1.2 to 0.2 %) in the Ramachandran plot . In particular, unambiguous orientations for residues forming the portal "lid" region of the protein were determined, suggesting a more open conformation for the portal region of apo-L-FABP as compared with the holo protein.

Isotropically tumbling bicelles (q = 0.5) were used as mimetic media for lipid membranes in the study of protein-membrane interactions of both L-FABP and I-FABP with high-resolution NMR. HSQC titration spectra for both proteins were compared with their apo counterparts. The largest chemical shift perturbations were located in the portal region (helix II) of both L-FABP and I-FABP, in addition to the C-D and E-F turns for L-FABP, and C-D and E-F beta strands for I-FABP. Preparation of a stable protein-bicelle complex permitted sequence-specific resonance assignments to be made for a model membrane-associated I-FABP system.

DEDICATION

I would like to dedicate this thesis to my father, mother, and brother and his family for their support, encouragement, and motivation.

ACKNOWLEDGEMENTS

My deepest gratitude goes to Prof. Ruth Stark for this opportunity to pursue the Ph.D in the Biochemistry program and all her help, guidance and encouragement. I also thank Dr. Hsin Wang for his help and patience in guiding graduate students through the program. I appreciate the help of all my committee members: Dr. Fred Naider, Dr. Judith Storch, Dr. Themis Lazaridis, and Dr. Ranajeet Ghose for their suggestions and participation in setting the path on this Ph.D. journey.

Also, I appreciate the help of my colleagues Yan He, Rima Estephan, and Xiaomin Yang.

My gratitude also goes to the CUNY Ph.D program in Biochemistry and CUNY College of Staten Island for providing the field to be able to pursue my dream of being a scientist.

TABLE OF CONTENTS

Chapter II (Materials and Methods)

LIST OF ABBREVIATIONS

($\Delta\delta$)	change in chemical shift
2D HSQC	two-dimensional heteronuclear single quantum correlation
3D TOCSY	three-dimensional total correlation spectroscopy
3D NOESY	three-dimensional nuclear Overhauser effect spectroscopy
Å	angstrom, 10^{-10} m
ADC	analog-to-digital converter
ADIFAB	acrylodan-derivatized intestinal fatty acid-binding protein
A-FABP	adipocyte fatty acid-binding protein
A-LBP	adipose lipid-binding protein
ANS	1-anilino-8-naphtalene sulfonate
B-FABP	brain fatty acid-binding protein
C_8E_5	octyl-penta-ethylene glycol
$C_{12}E_5$	dodecyl-penta-ethylene glycol
CHAPSO	(3-(cholamidopropyl) dimethylammonio-2- hydroxy-1-propanesulfonate
CoA	coenzyme A
CPM	counts per minute
CRABP II	cellular retinoic acid binding protein type II
CRABP I	cellular retinoic acid binding protein type I
CRBP II	cellular retinol binding protein type II

CRBP I	cellular retinol binding protein type I
DAUDA	11-(dansylamino)undecanoic acid
DHA	docosahexaenioc acid
DHPC	dihexanoylphosphatidylcholine
DIODPC	1,2-di-O-dodecyl-sn-glycero-3-phosphocholine
DIOHPC	1,2-di-O-hexyl-sn-glycero-3-phosphocholine
DIOMPC	1,2-di-O-myristoyl-sn-glycero-3-phosphocholine
DMPC	dimyristoylphosphatidylcholine
DMPG	dimyristoylphosphatidylglycerol
DOPG	dioleylphosphatidylglycerol
DSS	sodium 2,2-Dimethyl-2-Silapentane-5-Sulfonate
ER	endoplasmic reticulum
EPA	eicosapentaenoic acid
EDTA	ethylenediaminetetraacetic acid
FA	fatty acid
FABP	fatty acid-binding protein
FID	free induction decay
FT	Fourier transform
H-FABP	heart fatty acid-binding protein
iLBPs	intracellular lipid binding proteins
INEPT	insensitive nuclei enhanced by polarization transfer

IPTG	isopropyl-β-D-thiogalactoside
K_d	dissociation constant
kDa	kilo Dalton
K-FABP	keratinocyte fatty acid-binding protein
LB	Luria Broth
L-FABP	liver fatty acid-binding protein
LDL	low-density lipoprotein
lysoPA	lysophosphatidic acid
lysoPC	lysophosphatidylcholine
lysoPE	lysophosphatidylethanolamine
lysoPG	lysophosphatidylglycerol
MHz	megahertz, 10^6 hertz
nM	nanomolar, 10^{-9} M
NMR	nuclear magnetic resonance
OD	optical density
OLA	oleate
PPAR	peroxisome proliferator-activated receptor
QLS	quasielastic light scattering
RBP	retinal binding protein
RDCs	residual dipolar couplings

rf	radio frequency
SDS-PAGE	sodium dodecyl sulfate-polyacrylamide gel electrophoresis
TEMED	N,N,N',N'-tetramethylethylenediamine
UV	ultraviolet
VLC-PUFA	very long chain polyunsaturated fatty acid

NUMBER LIST OF TABLES PAGE

NUMBER **LIST OF FIGURES** **PAGE**

Chapter 1: Background and Objectives

1) Fatty acid-binding proteins

Inter- and intracellular long-chain fatty acid transport, which enable these essential metabolites to perform their different physiological functions, require substantial solubility in the aqueous medium (Vorum et al., 1992). A number of specific proteins have been identified that can bind fatty acids reversibly and non-covalently, thereby greatly enhancing their aqueous solubility and facilitating both their extracellular and intracellular translocation. Fatty acid-binding proteins (FABPs) are 14-15 kDa water-soluble proteins that are thought to mediate intracellular fatty acid transport (Glatz et al., 1996; Storch et al., 2000). To date, 14 members of the FABP gene family have been identified and shown to display a characteristic pattern of tissue distribution (Table 1.1) (Storch et al., 2000; Chmurzynska et al. 2006). Whereas most of the FABPs are found in a single tissue or cell type, H-FABP and L-FABP are expressed in several tissues. The former is found in muscle cells (heart and skeletal), kidney, stomach, mammary glands, and ovaries; the latter is expressed in kidney, small intestine, and colon in addition to the liver (Table 1.1) (Zschiesche et al., 1995; Glatz, et al., 1996; Myers-Payne et al., 1996).

a) Biological function

The function of cellular FABPs is not restricted to intracellular transport and solubilization of fatty acids but also involves trapping, selection of specific types of fatty acids, and compartmentalization, as well as direct involvement in fatty acid metabolism as co-factors. For example, a functional relationship has been found between FABPs (L-FABP, K-FABP, and A-

FABP) and activation of nuclear receptors involved in gene transcription of fatty acid metabolic enzymes, e.g., peroxisome proliferator-activated receptors (PPARs) (Tan et al., 2002). FABPs are also thought to regulate lipid metabolism, signal transduction pathways and cellular protection by maintaining the concentrations of free cytosolic fatty acids below toxic levels (Kaikaus et al., 1990; Vancura et al., 1992). Moreover, they have been implicated in cellular growth and differentiation (Sorof et al., 1994).

In cultured cells, saturated and unsaturated fatty acids have been found to act as primary and secondary messengers that reversibly induce the expression of lipid-related genes (Amri et al., 1996) and the release, for example, of arachidonic acid from phospholipid membranes. These signaling pathways involve both membrane-associated and cytoplasmic FABPs (Figure 1.1). These proteins may also be involved in regulation of the synthesis of lipophilic compounds (eicosanoids in the case of L-FABP) through signal transduction pathways. Moreover, a relationship has been suggested between the presence of an L-FABP analog protein (amino-azo dye-binding protein A) and cell proliferation (Ketterer et al., 1967). Some studies have also suggested that L-FABP mediates mitogenesis of rat hepatocytes (Sorof et al., 1994). Finally, other types of FABPs, such as A-FABP, H-FABP, and B-FABP, have also been found to be involved in cell growth and differentiation.

b) Ligand transport and membrane interactions

It has been proposed that FABPs facilitate long-chain fatty acid transport through the cell by increasing their solubility (Tipping et al., 1981). In the absence of FABP, the fatty acid partitions into membranes and undergoes substantial lateral diffusion within the plane of the membrane,

which slows its rate of movement. FABPs and intracellular lipid-binding proteins (iLBPs) are divided into two general classes based on their ligand transfer mechanism to membranes (Figure 1.2): 1) diffusion of ligand through the aqueous phase and subsequent association with the acceptor membrane occurs for liver FABP (L-FABP) and cellular retinol-binding protein type II (CRBP II); 2) a collision-mediated process in which the FABP and the acceptor membrane are in direct contact occurs for intestinal FABP (I-FABP), adipose FABP (A-FABP), heart FABP (H-FABP), kidney FABP (K-FABP), and cellular retinol-binding protein type I (CRBP I) (Kim et al., 1992; Herr et al., 1996; Hsu et al., 1996; Gericke et al., 1997; Thumser et al., 2000). FABP proteins that follow the first mechanism may have diminished ability to interact with membranes and therefore bind only fatty acids that are already in aqueous solution. The best-studied example of this class is liver FABP (Hsu et al., 1996; Thumser et al., 2000; Corsico et al., 2004). The second mechanism involves an interaction between a positively charged region of the binding protein and negative charges on the membrane surface, resulting in a conformational change that permits direct transfer of fatty acid between the protein binding site and the membrane (Herr et al., 1996; Gericke et al., 1997; Corsico et al., 1998; Storch et al., 2000). It has been proposed that FABPs with a diffusional transfer mechanism (e.g., L-FABP in hepatocytes) act in cells with large intracellular transport distances between their membranes so that diffusion of the fatty acid across the aqueous layer is rate-limiting. Conversely, those with collisional mechanisms may facilitate dissociation in cells with shorter transport requirements (e.g., H-FABP in the cardiac myocyte) (Weisiger and Zucker, 2002).

c) Molecular structure

FABPs display an amino acid sequence homology that ranges between 20 and 70%, and they all show a high degree of similarity with respect to their tertiary structures. They, together with the broader family of iLBPs, share a common structural motif consisting of 10 antiparallel β-strands and two short α-helices located between the first and second of these β-strands (Figure 1.3). The β-strands form two five-stranded sheets, where one sheet is arranged in a perpendicular orientation to the other sheet to form a barrel-like structure that surrounds a solvent-filled cavity in which an amphiphilic ligand can bind (Banaszak et al., 1994). The fatty acid(s) may enter the binding cavity through a portal area enclosed by a cap composed of two α-helices. This flexible region of the protein behaves as a portal 'lid' that may open and close upon entry and release of ligand from the binding cavity (Lucke et al., 1992). In general, the FABP β-barrel structure is found to be very consistent in all FABPs, as was proposed from studies involving chemical modification and targeted mutagenesis (Herr et al., 1996; He, 2000 Ph.D. Thesis). Also, in general, the holo-protein is more stable than its apo- counterpart, as evidenced by visual comparison of its 2D NMR spectra over time and by its longer time to precipitate (Richieri et al., 1996).

The first crystal structure of an FABP was determined for serum retinol-binding protein (RBP) (Newcomer et al., 1984). Subsequently, crystal structures have been determined for apo-I-FABP (Scapin et al., 1992), holo-Myelin-FABP (MP2) (Cowan et al., 1993); holo-A-FABP (Lalonde et al., 1994), apo-H-FABP (Young et al., 1994) and holo-L-FABP (Thompson et al., 1997). FABP structures have also been determined using multidimensional triple-resonance

NMR methods. The solution structures determined using NMR include I-FABP (Hodsdon et al., 1996; Zhang et al., 1997), CRBP II (Lu et al., 1999), and L-FABP (He et al., 2007).

2) Liver Fatty Acid-Binding Protein: Unique Properties and Ligand Binding

Liver fatty acid-binding protein (L-FABP) was the first of the family of iLBPs to be cloned and purified from recombinant sources. L-FABP is expressed abundantly in both the liver and the small intestine, where it constitutes 2-5% of the total concentration of cytoplasmic proteins (Ockner et al., 1972). In addition to the liver and intestine, L-FABP may also be found, to a lesser extent, in kidney and colon, all tissues with highly active fatty acid metabolism.

a) Biological function

L-FABP has long been reported to facilitate cellular uptake, transport, and metabolism of poorly soluble lipids. It was later found to have a role in cell growth and differentiation, through its ability to bind mitogenic lipids *in vivo* and transport them to nuclear receptors. L-FABP may also interact directly with certain enzymes involved in phospholipid and triglyceride synthesis (Glatz et al., 1996).

b) Distinctive structural and binding features

Among the family of FABPs, L-FABP has several distinctive features in addition to its diffusional mechanism of ligand transfer. L-FABP has a broad ligand specificity: in addition to the high-affinity binding of long-chain fatty acids, it has been reported to bind heme, bilirubin,

lysophospholipids, eicosanoids, bile salts, acyl-CoA thioesters, bromosulphothalein, hexachlorophene, cyclopentenone and prostaglandins (Vincent et al., 1985; Storch et al., 1993; Banaszak et al., 1994; Glatz et al., 1996; Richieri et al., 2000). While most of the FABPs are reported to bind one long-chain fatty acid per protein molecule, L-FABP has been found to bind two fatty acids (Thompson et al., 1997). A complete crystallographic structure of rat L-FABP, with two bound oleic acid molecules in its cavity, was determined to 2.3 Å resolution (Thompson et al., 1997). The two fatty acid molecules can be accommodated in a cavity that is relatively large compared with the rest of the iLBPs; using the crystallographic coordinates for holo-L-FABP, the solvent-accessible volume of the ligand-binding cavity in L-FABP is estimated to be 610 $Å^3$, as compared with 450 $Å^3$ in holo-A-LBP and 353 $Å^3$ in apo-I-FABP (Table 1.2) (Thompson et al., 1999). Subsequently, solution-state NMR data reported for both apo- and holo-L-FABP have enabled some comparisons with the structure of the holo-protein in the crystalline state (Wang et al., 1998; Wang et al., 2002).

c) Ligand affinities

Binding studies using the acrylodan-derivatized intestinal fatty acid-binding protein (ADIFAB) fluorescent probe have indicated high binding affinities (K_d < 500 nM) of L-FABP to long-chain fatty acids and lower affinities for other hydrophobic ligands (Jakoby et al., 1993; Richieri et al., 2000). However L-FABP, as well as other FABPs, is predicted to exhibit weak binding for both medium- and short-chain fatty acids, due to an increase in FA aqueous solubility for shorter hydrophobic chains. Studies have been conducted using fluorescence-based methods with 11-(dansylamino)undecanoic acid (DAUDA), 1-anilino-8-naphtalene sulfonate (ANS), and

intrinsic fluorescence binding assays in order to investigate the binding of very long chain polyunsaturated fatty acids (VLC-PUFA) (> 20-carbon chains) to L-FABP and their possible role in directing, regulating, and processing these fatty acids biosynthetically (Rolf et al., 1995). Among these VLC-PUFA are eicosanoids (20-carbon polyunsaturated fatty acids), potent messenger substances that regulate a wide variety of processes including gastric acid secretion, blood pressure control, and inflammation (Sprecher et al., 2000). However, inconsistent data were obtained for the stoichiometry of binding to L-FABP, and their binding site(s) within the cavity remain ambiguous.

Fluorescence displacement assays have shown 10-fold lower L-FABP affinity for lysophospholipids as compared with oleic acid (Thumser et al., 1995). However, the existence of one or more ligand-binding site for lysophospholipids within the protein cavity remains controversial. Crystal structure models have placed one of the bulky polar anionic ligands of L-FABP adjacent to the α- helical region of the protein, thus allowing for solvent exposure (Thompson et al., 1999). It has been proposed, through DAUDA displacement assays on L-FABP mutants, that the polar polyanionic groups of Acyl CoA and lysophospholipids lie in the portal extending into the solvent and interact electrostatically with K20, K31, and K33 of helix-II (Davies et al., 2002). Thumser et al. (1994) have found that the L-FABP interactions lack specificity for the polar group of the non-acyl moiety adjacent to the phosphate in lysophosphatidylcholine (lysoPC), lysophosphatidylethanolamine (lysoPE), lysophosphatidic acid (lysoPA), and lysophosphatidylglycerol (lysoPG) (Figure 1.4), possibly ruling out the interaction of the head groups of these lipids with protein residues (Thumser et al., 1994). There have been no studies reported to date on L-FABP binding to diacylphospholipids.

The importance of heme-binding proteins emerged after the discovery of heme's ability to produce an increase in oxygen free radicals in endothelial cells (Balla et al., 1991). Twenty years ago, Styliani et al. (1985) discovered a small cytosolic protein in the rat liver that bound heme with high affinity and shared a sequence homology to L-FABP. This report prompted a drive to investigate protein binding of heme and its non-metallic protoporphyrin analog (Epstein et al., 1994; Tipping et al., 1976; Bass et al., 1985; Wilkinsen et al., 1987; Ballou et al., 1983). Because of L-FABP's ability to accommodate a large variety of ligands and its high concentration in liver cells (Banaszak et al., 1994), its binding to heme was investigated; a tenfold higher LFABP affinity to heme compared with oleate was reported (Styliani et al., 1985).

Intra-and intercellular transport of cholesterol occurs via various mechanisms (Liscum et al., 1992). Due to cholesterol's insolubility in aqueous media, there may be a role for protein-mediated transport. L-FABP has been a candidate in studies to elucidate the role of carrier proteins in cholesterol transport. These studies have gained momentum from the finding that L-FABP may be able to accommodate a variety of hydrophobic ligands within its binding cavity. However, cholesterol's binding to L-FABP has remained controversial. Nemecz et al. (1991) reported, using a Lipidex-1000 assay and other methods, that L-FABP is able to bind one equivalent of cholesterol and the fluorescent sterol dehydroergosterol. However, other groups were not able to confirm this binding. Subsequent studies aimed at probing cholesterol interactions with L-FABP have instead found binding to bile salts, with relative affinities that depend inversely on their water solubility (Wilkinsen et al., 1987; Rolf et al., 1995; Thumser et al., 1996).

d) Oleate binding geometry and proposed mechanism

Oleate (OLA) binding to L-FABP has been studied by X-ray crystallography (Thompson et al., 1997). The crystal structure has provided a basis for further structural analysis aimed at examining the broader specificity and the unusual stoichiometry observed with hydrophobic ligands bound to L-FABP. In the crystal structure of L-FABP with two bound oleates (Figure 1.5), one fatty acid molecule (OLA 129) has a roughly U-shaped conformation deep within the binding cavity. The carboxylate of this oleate is not accessible to solvent, although it is involved in a hydrogen bond network with bound waters. The second oleate molecule bound to L-FABP (OLA 128) has an extended conformation with its carboxylate moiety located near the surface of the L-FABP molecule. The buried carboxyl group of OLA 129 is involved in an extensive hydrogen-bonding network. The cavity residues involved in this network are R122, for which a role in FA electrostatic stabilization has been identified (Borchers et al., 1993; Thumser et al., 1994), S39, and S124. This network also involves interactions with six bound waters within the binding cavity. Additional amino acids found close to OLA 129 are I41, F63, E72, T73, T93, and T102. OLA 128 is located near residues forming the portal and is also a part of hydrogen-bonding network that includes K31, Y54, S56, D88 and bound water. Hydrophobic interactions have been proposed between the two oleates, in which the alkyl chain of OLA 128 is stabilized hydrophobically by OLA 129 which lies deep within the cavity. A binding model has been suggested for the two oleates in which the first (innermost) site is occupied to form a hydrophobic surface that facilitates binding of the second oleate.

e) Project objective: ligand specificity of L-FABP

Our goal in this study is to use NMR methods to determine the effect of changes in FA saturation, chain length, and head group on the tertiary structure and binding sites of L-FABP to ligands with different headgroups and degrees of unsaturation (e.g., oleate, palmitate, and lysophosphatidylcholine). Comparisons are also made between L-FABP binding to fatty acids and its reported binding to non-fatty acid ligands such as hemes and cholesterol, exploring how the bulky ligands can be accommodated in its cavity. These comparisons, which are referenced to data from both X-ray crystallography and NMR for L-FABP with two bound oleates, aim ultimately at relating its unique ligand-binding diversity with its functions. This endeavor is timely because ten years after the determination of its crystal structure, our understanding of L-FABP intracellular functions has been extended from a hydrophobic ligand transporter to include regulatory roles in lipid metabolic pathways (Glatz et al., 1996; Lawrence et al., 2000; Wolfrum et al., 2001).

3) Nuclear Magnetic Resonance Spectroscopy (NMR)

The nuclear magnetic resonance (NMR) spectroscopy phenomenon occurs when an oscillating magnetic field causes net energy absorption for the nuclei of certain atoms that lie in a second static magnetic field. This phenomenon can be beneficial in studying physical, chemical, and biological properties of matter and can be applied to various areas of science. While solution-state NMR techniques are used to examine molecular structure and dynamics in organic or aqueous solution, solid-state NMR spectroscopy is used for analogous structural studies of amorphous and crystalline solids. The first NMR signals were observed independently by two

groups of physicists in 1945: Bloch, Hansen, and Packard at Stanford University (Bloch et al., 1946) and Purcell, Torrey, and Pound at Harvard University (Purcell et al., 1946). Subsequently, the development of NMR techniques has accelerated; biological NMR often complements and sometimes rivals X-ray crystallography for the determination of protein structure (Garbuzynskiy et al., 2005).

a) Principles and theory

Nuclei of many elemental isotopes such as ^{1}H, ^{15}N, and ^{13}C have a spin that can have quantum numbers that are integral (e.g. I = 1, 2, 3 ...) or fractional (e.g. I = 1/2, 3/2, 5/2 ...). Nuclei with spin>0 are called NMR active and possess a magnetic moment μ. However, nuclei with spin equal to zero have no magnetic moment. When an I= ½ nucleus is subjected to a nonzero external magnetic field (B_0), two spin states are possible: spin state +1/2 of lower energy is aligned with the external field, while spin state -1/2 with higher energy is opposed to it. The difference in energy between the two states depends on the external magnetic field strength, is typically ≤ 0.4 Joule/mole, and is given by the equation $\mu B_x / I$ (I = ½, μ is the magnetic moment of the nucleus, and B_x is the value of magnetic field strength) (Figure 1.6). The spinning nucleus precesses in the magnetic field with a frequency that is proportional to the strength of the magnetic field: $\omega_o = \gamma B_o$, where ω_o is called the Larmor frequency with units of radians per second and **γ** is a constant known as the gyromagnetic ratio that is proportional to the magnetic moment through the equation ($\gamma = 2\pi\mu/hI$). If a radiofrequency (rf) energy with a frequency that is equal to the Larmor frequency is directed along its x-axis, the precessing nucleus will absorb energy and the magnetic moment will flip to its I = -1/2 state (Figure 1.7). In NMR experiments,

when the oscillating magnetic field is turned off, nuclei precessing in phase lose energy to other atoms and nuclei in the solution (lattice), generating thermal (enthalpic) energy. This relaxation is called spin-lattice relaxation. However, another concurrent relaxation process called spin-spin relaxation leads to an energy exchange that diminishes the phase coherence through random processes (entropic relaxation). As the excited nuclei relax, their resonance signals are collected by the computer and subjected to a Fourier transform (FT), a mathematical procedure that converts the complex time domain signal into a frequency domain presentation (Figure 1.8). (Slichter, 1978; Bovey et al., 1988; Abraham et al., 1993; Cavanagh et al., 1996; Van Holde et al., 1998).

b) Chemical shifts and spin-spin couplings

Nuclei spinning in the magnetic field produce a local current that can oppose or add to the applied field B_0. The change of the magnetic field as a result of these local fields, which reflects a particular chemical structure, is called nuclear shielding. Bonded groups of nuclei also interact with each other, and the effect of this interaction is called spin-spin coupling or J coupling. For example, the energy level diagram for the spin-spin interaction of acetaldehyde protons and their ^{1}H NMR spectrum is depicted in Figure 1.9. The CHO absorption line is split into 4 absorption lines centered on δ_A, and the CH_3 absorption line is split into 2 lines centered on δ_B. The distance (in Hz) between two split absorption lines is called the J coupling constant or the spin-spin splitting and is a measure of the magnetic interaction between the two groups of nuclei (aldehyde and methyl protons) (Bovey et al., 1988; Van Holde et al., 1998).

c) Instrumentation

The typical hardware of a Fourier transform (FT) spectrometer includes several components: 1) the magnet consists of a superconducting solenoid and shims immersed in liquid helium. Magnets with higher magnetic field strength (^{1}H resonance frequency 600-900 MHz) produce NMR spectra with higher resolution (Figure 1.10); 2) the field- frequency lock system consists of a transmitter and receiver that measure the resonance frequency of deuterium or other lock nuclei; 3) the rf transmitter consists of frequency synthesizers, amplifiers, and associated electronics for producing pulses of monochromatic rf electromagnetic radiation with defined phase and amplitude; 4) the rf receiver includes a preamplifier, phase-sensitive detector, and analog-to-digital converter (ADC); 5) the probe has functions that include converting the radiofrequency power from the transmitter into oscillating magnetic fields that are applied to the sample and converting the oscillating magnetic fields which are generated by the nuclear spins of the sample into signals detected by the receiver; 6) the room-temperature shim coils maintain the spatial homogeneity of the magnetic field by adjusting the electric current (Roberts et al., 1993; Cavanagh et al., 1996).

d) Multi-dimensional NMR experiments

Figure 1.11 shows the ^{1}H NMR spectrum of apo-L-FABP. Even for a small protein with 127 amino acids, extensive resonance overlap makes their assignment challenging. In multidimensional FT NMR spectral crowding is relieved and bonded interactions are delineated by spreading these resonance signals over two or more dimensions. Examples of these experiments (discussed further below) are 2D HSQC (Heteronuclear Single Quantum

Correlation), ^{15}N-edited 3D TOCSY (Total Correlation SpectroscopY) -HSQC and ^{15}N-edited 3D NOESY (Nuclear Overhauser Effect SpectroscopY) -HSQC , which correlate the nuclei of interest (amide protons, amide nitrogen, and side chain protons) through bonds and through space, respectively.

(i) Two-dimensional HSQC (Heteronuclear Single Quantum Coherence)

HSQC (Heteronuclear Single Quantum Coherence) correlates a nucleus (e.g., nitrogen of an NH group) with a directly attached nucleus (e.g., proton) (Mandal et al., 2004). Each signal in the ^{15}NH HSQC spectrum of a uniformly ^{15}N-enriched protein represents a proton that is bound to a nitrogen atom (Figure 1.12). The spectrum contains the signals of the HN protons in the protein backbone. Since there is only one backbone HN per amino acid (though none for Pro), each HSQC signal represents one single amino acid. The HSQC spectrum also contains signals from the NH_2 groups of the side chains of Asn and Gln, which can easily be distinguished as doublets in the HN dimension; additionally there are signals from the aromatic HN protons of Trp and His, with the Trp protons located downfield at about 10 ppm.

The ^{15}N-edited HSQC experiment employs two Insensitive Nuclei Enhanced by Polarization Transfer (INEPT) magnetization transfers (Morris et al., 1979) (Figure 1.13). The first one creates antiphase heteronuclear coherence ($I_Y \rightarrow 2I_Z S_Y$), and the second is used to convert this coherence back to observable magnetization ($2I_Z S_Y \rightarrow I_Y$). The pulse sequence in Figure 1.13 is summarized by the following: 1) ^{1}H antiphase magnetization ($2I_X S_Z$) during τ is generated by a 90° pulse; 2) a refocusing 180° pulse on both spins is introduced in the middle of the τ period; 3) coherence transfer to the directly attached ^{15}N is achieved by simultaneous 90° pulses on both

spins ($2I_Z S_Y$); 4) refocusing the evolution of heteronuclear J_{IS} coupling is done by a 180° pulse on the *I*-spin (^{1}H); 5) a 90° pulse on each spin transfers the magnetization back to ^{1}H as antiphase *I*-spin magnetization ($2I_Y S_Z$); 6) antiphase in-phase conversion of ^{1}H proton magnetization ($2I_Y S_Z \rightarrow I_X$) is achieved by a final spin-echo period (Bovey et al., 1988; Van Holde et al., 1998).

HSQC has long been used in structural and functional studies of proteins, for example, in examining protein-ligand binding interactions or monitoring the folding or refolding of proteins. Because of its high sensitivity to ligand interaction over a wide affinity range, and its ability to map the protein binding site(s) in a residue-specific manner, perturbation of chemical shifts (or linewidths) can be monitored usefully during progressive ligand addition to the apo protein.

(ii) Three-dimensional NOESY (Nuclear Overhauser Effect Spectroscopy)

The NOESY experiment takes advantage of the exchange of z- magnetization using through-space dipolar interactions between pairs of nuclei separated by less than 5 Å. The intensity of a cross peak reflects the relative distance between the spins that are correlated, since there is an inverse sixth-power dependence of the pairwise dipolar interaction on the distance between the two coupled nuclei. A typical *IS* (*I* = ^{1}H, *S* = ^{15}N) 3D NOESY–HSQC experiment, with a pulse sequence shown in Fig. 1.14, is basically a concatenation of a homonuclear ^{1}H-NOESY and a heteronuclear HSQC experiment. Magnetization is transferred to the I spin (HN) during the NOESY mixing period. An HSQC sequence then transfers magnetization via J coupling from the I (HN) spin to the directly bonded S spin (^{15}N), and then back to the I spin (HN) for detection (Cavanagh et al., 1996). The NOESY experiment has become indispensable for conformational analysis and structural elucidation of biomolecules. For instance, the high-resolution structures

of both apo- and holo- L-FABP have been calculated in our lab from intramolecular NOE restraints, J-coupling constants, and residual dipolar couplings (described below; He et al., 2007).

(iii) Three-dimensional TOCSY (Total Correlation Spectroscopy)

For homonuclear NMR in solution, the total correlation spectroscopy (TOCSY) experiment is a typical example in which the magnetization transfer is based on scalar (spin-spin) coupling. The transfer of magnetization usually proceeds beyond directly coupled nuclei and passes through the more extensive scalar-coupled network of a covalently linked molecular chain (Cavanagh et al., 1996). The pulse sequence of the 3D TOCSY experiment is illustrated in Figure 1.15.

In addition to enabling structure calculation from NOE restraints, cross-peaks from 3D TOCSY-HSQC and 3D NOESY-HSQC (Figure 1.16a) can supplement sequence-specific resonance assignments of the HN backbone derived from comparisons of HSQC with reference spectra. Data sets from these experiments can be used to clarify ambiguous assignments of amide peaks that are not identifiable by visual inspection due to overlap, broadening, weak signals, or large chemical shift perturbations. These 3D experiments resolve cross peaks between ^{1}H spins according to the chemical shift of the ^{15}N bonded directly to the ^{1}H spins, with TOCSY-HSQC providing intraresidue correlations and NOESY-HSQC providing interresidue correlations, respectively. For example, Figure 1.16b shows the peaks of the C_{α} protons of Gly 37 (i) in TOCSY-HSQC and their correlation with those of Val 38 (i+1) in the NOESY-HSQC spectra of ^{15}N-apo-L-FABP. Identifying these correlations along the protein's primary sequence allows for

sequential assignments of the protein residues and confirms the assignments derived from related protein samples by visual inspection.

(iv) Other multidimensional experiments

In order to obtain complete backbone and side-chain resonance assignments, a series of multi-dimensional NMR experiments is also required (Figure 1.17). HNCACB (Kay et al., 1994) and CBCA (CO)NH (Grzesiek and Bax 1992) experiments are used to obtain sequence-specific backbone assignments of the protein chain. CBCA(CO)NH correlates the amide ^{1}HN and ^{15}N of one residue (i) with the $^{13}C^{\alpha}$ and $^{13}C^{\beta}$ of the preceding residue through $J_{C}{}^{\alpha}{}_{C}{}^{\beta}$, $J_{C}{}^{\alpha}{}_{C}{}^{o}$, and J_{NH} magnetization transfer (Figure 1.18). HNCACB, however, correlates the amide ^{1}HN and ^{15}N of one residue (i) with the $^{13}C^{\alpha}$ and $^{13}C^{\beta}$ of the same residue (i) and the preceding one through $^{1}J_{NC}{}^{\alpha}$ and $^{2}J_{NC}{}^{\alpha}$, respectively. Since the interresidue (through two bond) coupling is of smaller magnitude than the one-bond intraresidue coupling, a strip of the HNCACB spectrum corresponding to a given residue, contains four peaks: two peaks ($^{13}C^{\alpha}$ and $^{13}C^{\beta}$) for the intraresidue correlation and two peaks of weaker intensity for the interresidue correlation, with each HN-N slice containing C^{α} and C^{β} with opposite signs for both residue (i) and its preceding one (i-1) (for example $^{13}C^{\alpha}$ is black and positive and $^{13}C^{\beta}$ is green and negative). Due to the smaller two-bond J coupling, peaks for the (i-1) residues are usually weaker, a property that is advantageous in determining the amino acid order for these sequence-specific assignments. In favorable cases, complete backbone sequential assignments can be made using only these two experiments.

Side-chain resonance assignments can be obtained by other sets of NMR experiments. Specifically, HCCH-TOCSY (Kay et al., 1993) correlates the protons and carbons of the aliphatic side chain and H(CCO)NH-TOCSY correlates side chain protons with the amide proton and nitrogen of the following residue (Figure 1.17) (Cavanagh et al., 1996).

4) Weakly Aligning Media For NMR Structural Analysis

New NMR methods have been developed during the last ten years to augment NOE-derived distance restraints used for structure determination. One of these methods uses residual dipolar couplings (RDCs), which provide crucial constraints that lead to structural refinement of macromolecules such as DNA and proteins (Tjandra et al., 1997).

a) Theory

In non-liquid crystal (isotropic) solutions, rotational motions of macromolecules average dipolar couplings to zero. However, in liquid crystalline media, the bond vectors of proteins (or DNA) align weakly with respect to the magnetic field (Figure 1.19), resulting in a residual coupling (RDC) that adds or subtracts to the through-bond *J* scalar couplings (Tjandra et al., 1997). The residual dipolar couplings observed in dilute liquid crystals can be described with the following formula (Lipsitz and Tjandra 2004):

$$D^{AB}(\theta,\phi) = D_a^{AB}\left[(3\cos^2\theta - 1) + 3/2R\sin^2\phi\cos 2\phi)\right] \qquad \text{Equation 1.1,}$$

where θ and φ are the angles between the dipolar coupling (bond) vector and the magnetic field direction and the projection angle of that vector onto the x-y plane, respectively (Figure 1.19). *R*

and D_a represent the cylindrical and axial components of the molecular alignment tensor, respectively, that can be calculated from the following equation (Clore et al., 1998):

$$D_a^{AB} = -\mu_0 (h / 2\pi)\gamma_A\gamma_B) / (4\pi^2 r^3_{AB}) \qquad \text{Equation 1.2.}$$

D_a depends on gyromagnetic ratios of the nuclei γ_A and γ_B, the magnetic permittivity of vacuum μ_0, and the distance between the nuclei r_{AB}. h is Planck's constant.

The angular constraints contained in residual dipolar couplings are complementary to the NOE data, which reflect short-range constraints. However, RDC's provide information about the orientation of any bond vector with respect to the magnetic field tensor, regardless of its location on the macromolecule's tertiary structure. A small set of RDC constraints is sufficient to introduce a high degree of refinement, and in conjunction with NOE restraints, is able to provide local and global structural determinants for biological macromolecules (Mauffret et al., 2002).

Of all the possible types of dipolar couplings (e.g., NCO, NCA, COCA, HNCA, HNCO and HACA; Figure 1.20), the relatively large (-20 to +10 Hz) NH residual dipolar coupling (Prestegard et al., 2000; Bax et al., 2001) is often used because of the large chemical shift dispersion of the amides. In the current study, NH RDCs were used to refine the structure of apo-L-FABP, for which the orientation of the helices with respect to the β-clam could not be determined with confidence from NOE measurements alone. For this purpose, RDC measurements of the NH bond vector for 57 residues of apo-L-FABP were converted into polar angles (θ) using equation 1.1 (Figure 1.19). Since these angles are correlated to the same magnetic tensor, the orientations of the bond vectors for these residues could be determined unambiguously.

b) Mechanism of alignment

As the particles in liquid crystals or the filaments of a matrix are oriented in a magnetic field, they induce a weak alignment of proteins or other solutes. This happens primarily due to a steric obstruction that will affect the populations of the different rotational states. Additionally, orientation may occur due to opposing surface charges between the protein and the liquid crystal particle (Hansen et al., 1998). If the chemical shifts of the protein resonance signals change significantly in the anisotropic medium there is the possibility that the structure has changed, which can invalidate the interpretation of residual dipolar couplings. Hence, the criteria for good aligning media, in addition to weak alignment in the magnetic field, include the presence of minimal interactions so that the macromolecule maintains its native tertiary structure.

c) Weakly aligning media

The first liquid crystal medium used to refine NMR-derived protein structures was bilayered micelles (bicelles) (Tjandra et al., 1997). Commonly used lipids are dimyristoylphosphatidylcholine (DMPC) and dihexanoylphosphatidylcholine (DHPC). Typically, concentrations of bicellar aligning media are ~ 3-5 % (w/v) (Tjandra et al., 1997), but the bicelle concentration can be adjusted for different degrees of protein alignment or for different protein sizes. These bicelles can also be modified (e.g., changes in surface charge), thus altering their pH and temperature stability ranges (Prestegard et al., 2001). For example, it was found that acidic (DMPG/DMPC/DHPC) bicelles have a reduced pH stability range (5.5-7.0) compared with their neutral (DMPC/DHPC) counterparts (Struppe et al., 2000). Also, a wider temperature stability range (10-55 $^{\circ}$C) was observed for ether-linked bicelles

(DIOMPC/DIOHPC) over their ester-linked (DMPC/DHPC) counterparts (27-40 °C), which is attributed to reduced vulnerability of the former lipids to hydrolysis (Prestegard et al., 2004; Aussenac et al., 2005). Other aligning media include rod-shaped viruses (bacteriophage Pf1), purple membranes, cellulose crystallites, a mixture of cetylpyridinium halide, *n*-hexanol and sodium halide and polyacrylamide gels (Hansen et al., 1998; Prosser et al., 1998; Sass et al., 1999; Barrientos et al., 2000; Sass et al., 2000; Tycko et al., 2000; Pääkkönen, 2003).

As noted above, DMPC/DHPC and phages are unstable at low pH due to hydrolysis (Hansen et al., 1998). Cetylpyridinium chloride/hexanol are only stable at high salt concentrations. In addition, purple membrane fragments and lipid bicelles may interact too strongly with the protein or DNA (e.g., FABPs with bicelles) to be suitable media for RDC measurements (Ruckert and Otting, 2000; Sass et al., 2000).

d) PEG aligning media

The residual dipolar couplings for apo-L-FABP were measured using liquid crystalline media composed of a mixture of *n*-dodecyl-poly (ethylene glycol)/ *n*-hexanol (Figure 1.21) (Ruckert and Otting, 2000), which is stable and easy to make. The resulting liquid crystals are uncharged, insensitive to both pH and salt content, non- or minimally binding to macromolecules, and usable at temperatures ranging between -10 °C and 40 °C (Figures 1.21 and 1.22). Within its stability range, a liquid crystalline phase of this system consists of planar bilayers of *n*-alkyl chains oriented parallel to the magnetic field. These alkyl-poly (ethylene glycol) molecules are usually denoted as C_mE_n, where m refers to the number of carbons in the *n*-alkyl group and n refers to

the number of glycol units in the poly(ethylene glycol) moiety (Clore et al., 1998; Ruckert and Otting, 2000).

e) Project objective: refinement of solution-state structure of apo-L-FABP

Whereas the tertiary structure of holo-L-FABP with the bound oleate ligand has been determined from both X-ray (Thompson et al., 1997) and NMR data (He et al., 2007), the structure of apo-LFABP is more challenging to determine because the protein does not form suitable crystals. Tertiary structures of apo-L-FABP had been calculated in our group from extensive NOE measurements, but the resulting 'open lid ' barrel structure was suspect because the protein was incompletely folded. Thus, our goal is to use RDC's to refine and critically evaluate the apo-L-FABP structure. In the current project, the apo structure of L-FABP is compared with and without residual dipolar couplings in $C_{12}E_5$/hexanol aligning media at 30 °C and pH 7.0.

5) Membrane mimetic media

a) Biological membranes

The biological membrane is a key structural element of all living cells that is composed of lipids and proteins (and in some cases attached carbohydrates). These membranes perform crucial physiological functions (e.g., respiration, photosynthesis, signal transduction, and compartmentalization) that are mainly attributed to their structural features. The structure of lipid membranes consists of an amphipathic lipid layer of hydrophilic polar groups lining the exterior and hydrophobic alkyl chains forming the core (Andersson, 2004).

b) Membrane mimetics

Many interesting features of biomembranes have been explored using diverse experimental and theoretical approaches, for instance characterization of the interaction of peptides and proteins with model membranes. For this purpose, artificial mixtures of lipids and/or detergents are utilized to mimic the key physical properties of actual biomembranes. The specific choice of membrane mimetic depends both on the biomembrane that is being mimicked and on the experimental procedures to be applied (Jing et al., 2005).

(i) Micelles

Micelles have been used as membrane mimetics since the early days of NMR structure determination (Brown et al., 1977; Wuthrich et al., 1980). Micelles are used today because micelle-associated proteins often undergo isotropic reorientation in solution, making it feasible to perform multidimensional solution-state NMR experiments on these samples. Even though the micelles mimic the molecular environment of biological membranes adequately and the resulting protein complex often exhibits high-resolution NMR spectra, they are not ideal as membrane mimetics because of their high curvature and absence of bilyer structure, which could cause changes in the tertiary structures of associated proteins. Moreover, most enzymes are inactive in micellar solutions.

(ii) Vesicles and bilayers

Unilamellar and multibilayer vesicles formed by synthetic phospholipids are popular

membrane models at the next level of complexity. They are commonly used in biophysical studies that address questions pertinent to membrane interactions with drugs. Phospholipid vesicles may exist in unilamellar or multilamellar forms, and the size of the vesicles varies depending on the preparation procedures. Because of their relatively large size (R~ 7-14 nm for small unilamellar vesicles) and slow tumbling, lipid vesicles are usually not suitable for NMR structural studies of integral membrane proteins. They are, however, suitable for monitoring drug-protein interactions using the NMR properties of the drugs (Xu et al., 2002).

(iii) Bicelles

Bilayered micelles (bicelles) can potentially provide a better membrane mimetic, since they contain a well-defined phospholipid bilayer region (Figure 1.23). The size and shape of a bicelle are defined by the molar ratio of lipids to detergents, the q-value. A theoretical relation between the bicelle radius and its q-value can be calculated as follows:

$$R = \tfrac{1}{2}\, rq\, [\, \pi + (\pi^2 + 8/q)^{1/2}] \qquad \text{Equation 1.3}$$

(Vold et al., 1997), where R is the radius of the bicelle. Glover et al., (2001) have modified this equation to account for the effect of the size of the polar group of the phospholipids.

Small bicelles in isotropic solution have been characterized by several techniques and found to be disk–shaped objects containing a phospholipid bilayer region surrounded by a detergent rim (Glover et al., 2001; Luchette et al., 2001). Small bicelles (q = 0.2-0.5, R~ 3-6 nm) (Glover et al., 2001) are a favorable membrane mimetic since, in addition to their bilayer morphology, they undergo rapid reorientation in the magnetic field and thus produce narrow spectral lines. (By contrast, the bicelles used for weak alignment and RDC measurements typically have q =

3). The isotropic bicelle aggregates have been used successfully in high resolution NMR structural and dynamic investigations of peptide-membrane interactions (Vold et al., 1997; Whiles et al., 2001; Andersson et al., 2002; Chou et al., 2002; Lindberg et al., 2003).

c) Project objective: interactions of L-FABP and I-FABP with model membranes (functional aspects and media for NMR)

Even though the tertiary structures of liganded L-FABP and I-FABP are very similar (Sacchettini et al., 1989; Thompson et al., 1997), their ligand transport occurs by two different mechanisms, diffusional and collisional for L-FABP and I-FABP, respectively. The Storch group has found, through fluorescence and mutational studies, that the α-helical region of I-FABP plays a primary role in the collisional mechanism for transfer of the fatty acids to lipid membranes (Corsico et al., 2004). For L-FABP, a model has been proposed for binding to lipid membranes under conditions of low ionic strength, in which initial multiple electrostatic interactions involving the more disordered cationic residues surrounding the ligand portal trigger a conformational change followed by a possible binding of beta strands βH, βI, and βJ to the interfacial region of DOPG anionic vesicles (Davies et al., 2002) (Figure 1.24). However, these reports do not provide a clear or detailed comparison of which protein structural elements account for the contrasting interactions of these FABP's with model membranes during fatty acid transfer.

In the current study, we have several aims. Firstly, we want to develop stable membrane mimetic media that are suitable for solution-state NMR experiments. The criteria for viable media include structural and molecular resemblence to physiological lipid membranes, fast

tumbling that yields high-resolution NMR spectra, and stability over a period of time that allows execution of the NMR experiments required for structural analysis. Secondly, chemical shift perturbation analysis with two- and three-dimensional NMR is designed to investigate the regions that are highly perturbed on the tertiary structure of L-FABP and I-FABP upon bicelle titration. Such studies should provide insight into the nature of interactions that promote this protein-membrane binding.

1.1: Fatty acid-binding proteins and their tissue distribution (Chmurzynska et al. 2006).

Table 1. Expression of the various types of FABP genes

Gene name	Common name	Alternative names*	Various expression experiments	Microarray analysis (GNF Atlas 2; Su et al. 2004)
FABP1	Liver FABP	*L-FABP*	liver (Ockner et al. 1982); intestine (Lowe et al. 1985; Sweetser et al. 1987)	fetal liver, liver, pancreas, kidney, small intestine
FABP2	Intestinal FABP	*I-FABP*	intestine (Sweetser et al. 1987; Green et al. 1992)	small intestine
FABP3	Heart FABP	*H-FABP*; muscle and heart FABP; mammary-derived growth inhibitor (MDGI)	heart, skeletal muscle, brain, kidney, adrenal gland (Heuckeroth et al. 1987); mammary gland (Kurtz et al. 1994)	heart, mammary gland, blastocysts
FABP4	Adipocyte FABP	*A-FABP*	adipose tissue (Amri et al. 1991; Bernlohr et al. 1997)	adipocyte, ciliary ganglion, appendix, skin, fetal thyroid, placenta
FABP5	Epidermal FABP	*E-FABP*; psoriasis-associated FABP (*PAFABP*)	skin, tongue, adipose tissue, mammary gland, brain, intestine, kidney, liver (Krieg et al. 1993); psoriatic skin (Madsen et al. 1992)	tongue, eye, snout epidermis, digits
FABP6	Ileal FABP	*Il-FABP*; gastrotropin	ileum, ovary (Gong et al. 1994)	hypothalamus, tongue, large intestine
FABP7	Brain FABP	*B-FABP*	brain (Kurtz et al. 1994; Shimizu et al. 1997)	fetal brain, occipital lobe, amygdala, olfactory bulb
FABP8	Myelin FABP	*MP2*	peripheral nervous system (Hayasaka et al. 1991)	olfactory bulb, spinal cord, amygdala
FABP9	Testis FABP	*T-FABP*	testis (Oko and Morales 1994)	salivary gland, mammary gland

*Data retrieved from OMIM database (http://www.ncbi.nlm.nih.gov/entrez/query.fcgi?db=OMIM)

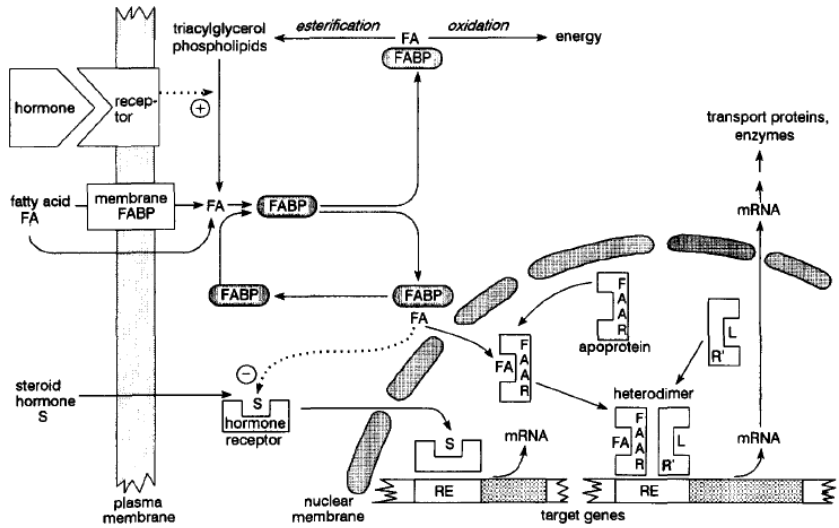

Figure 1.1: Intracellular transport of long-chain fatty acids and their role as transcription regulators for lipid metabolic pathways in response to hormonal stimuli. FA: long-chain fatty acid; FABP: fatty acid-binding protein; FAAR: fatty acid-activated receptor; L: ligand; R': nuclear receptor; RE: response element; S: steroid hormone; + activation; - inhibition (Glatz and Van der Vusse, 1996).

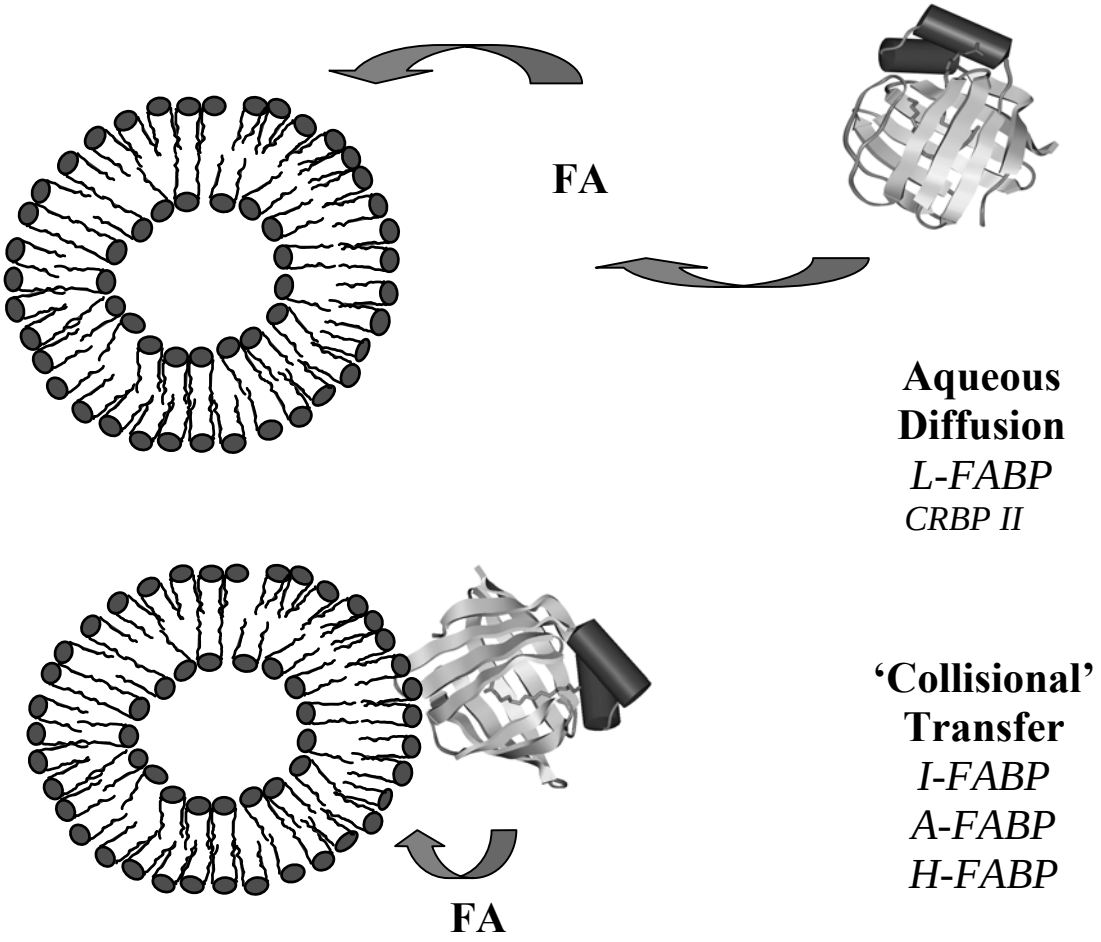

Figure 1.2: Transfer of fatty acids from FABPs to membranes occurs by two different mechanisms: diffusional transfer or a collision-mediated process (Storch et al., 2000).

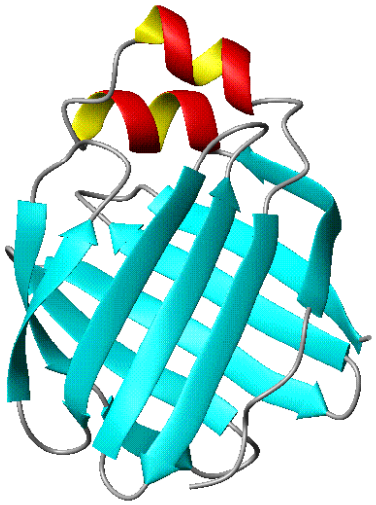

Figure 1.3: Common structural motif of iLBP proteins, consisting of 10 antiparallel β-strands arranged to form a barrel-like structure surrounding a solvent-filled cavity (blue), and two α-helical segments (red and yellow) forming, along with the turns, a flexible "lid" portal (Banaszak et al., 1994).

Table 1.2: Comparison of binding cavity properties for the crystal structure of L-FABP and iLBP family (Thompson et al., 1999). RMSDs are calculated with respect to L-FABP.

	PDB code	Cavity ($Å^2$)	($Å^3$)	rmsd (Å)
Liver Fatty Acid Binding Protein (LFABP)	1lfo	610	440	0.0
Locust Muscle Fatty Acid Binding Protein (L-MFABP)	1ftp	510	350	1.49
Myelin P2 Lipid Binding Protein (P2)	1pmp	420	330	1.34
Manduca sexta Fatty Acid Binding Protein (MFB2) ¥	1mdc	388	324	1.89
Heart Muscle Fatty Acid Binding Protein (HFABP) ¥	1hmr	391	323	1.46
Adipocyte Lipid Binding Protein (ALBP)	1adl	450	310	1.45
Cellular Retinol Binding Protein II (CRBPII)¥	1opb	372	261	1.46
Cellular Retinoic Acid Binding Protein II (CRABPII)	1cbq	470	260	1.62
Cellular Retinoic Acid Binding Protein I (CRABPI)	1cbr	410	210	1.67
Cellular Retinol Binding Protein 1 (CRBPI)¥	1crb	334	235	1.70
Intestinal Fatty Acid Binding Protein (IFABP)¥	1ifc	353	234	1.81

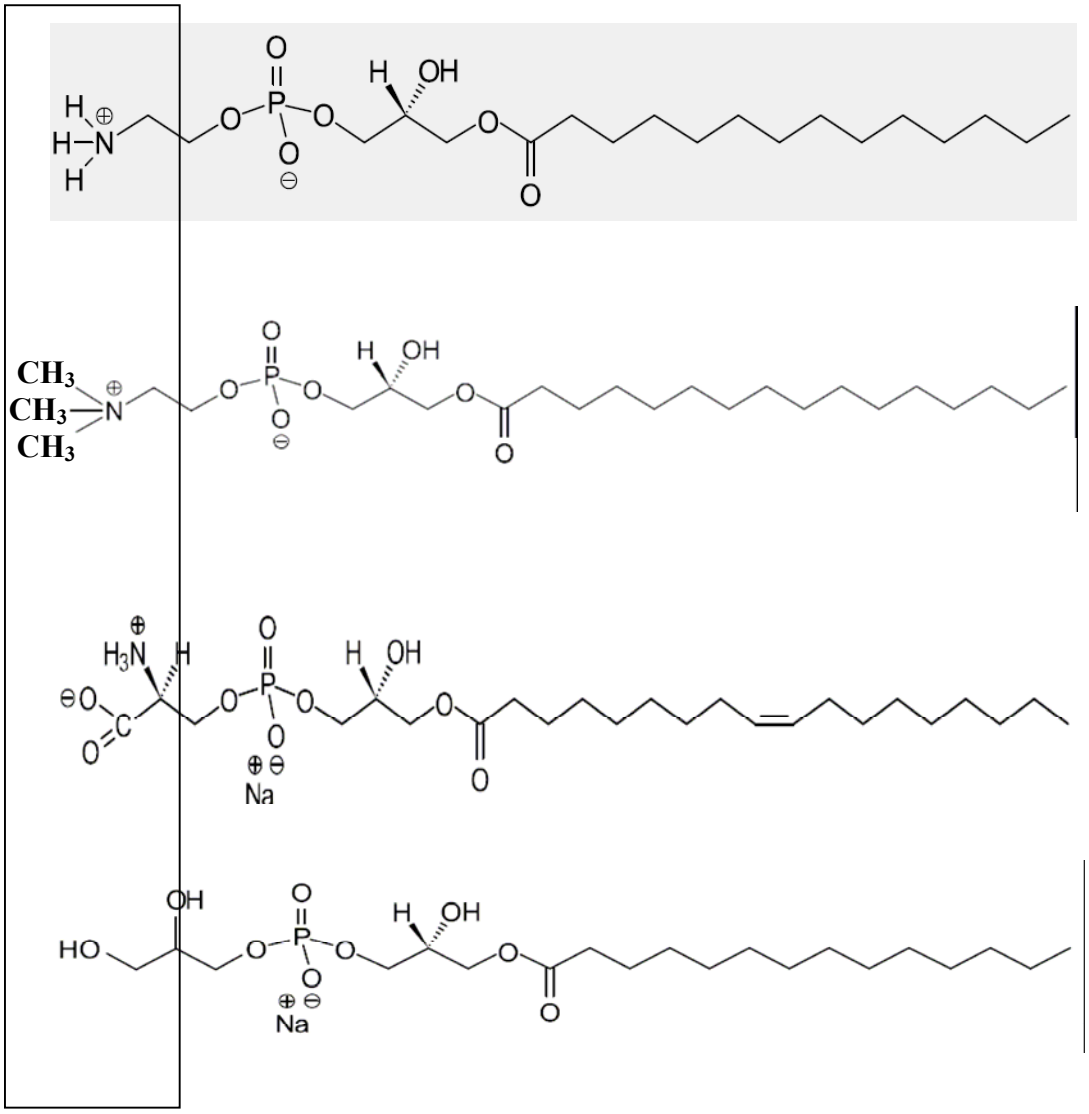

Figure 1.4: Molecular structure of lysophospholipids. Regions in rectangles represent the polar head group attached to the lysophospholipid chain:
a) ethanolamine, b) choline, c) serine, and d) glycerol. Palmitoyl, oleoyl, and myrisoyl chains are illustrated.

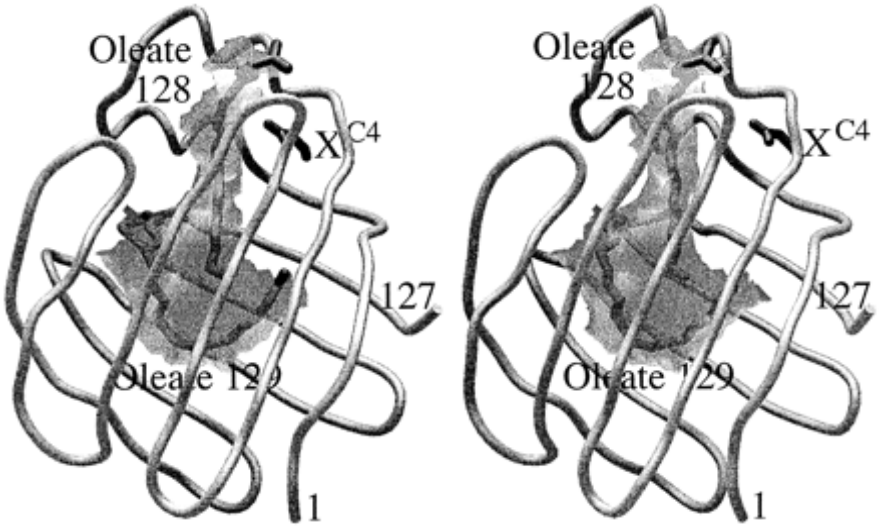

Figure 1.5: Crystal structure of L-FABP with two bound oleates (Thompson et al., 1997).

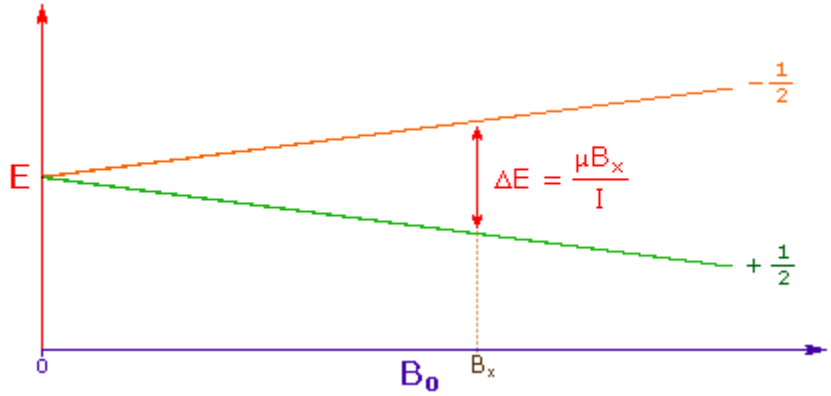

Figure 1.6: The energy profile of a 'spinning charge' with a magnetic moment (μ) in presence of an external magnetic field (B_0)
(http://www.cem.msu.edu/~reusch/VirtualText/Spectrpy/nmr/nmr1.htm).

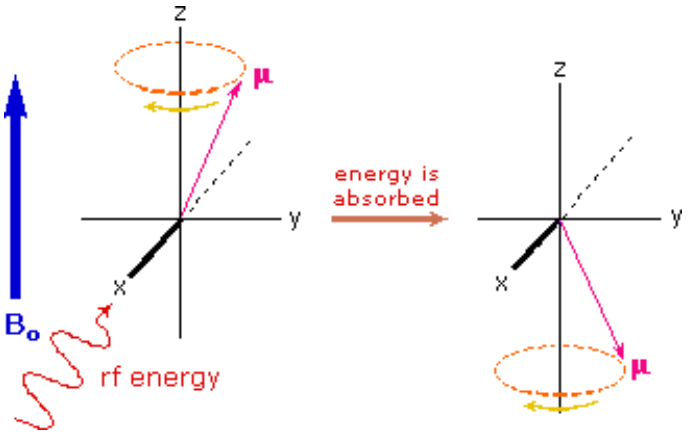

Figure 1.7: A spectral transition for a precessing nucleus with a Larmor frequency (ω_o) proportional to the strength of the magnetic field, as given by the equation: $\omega_o = \gamma B_o$. (http://www.cem.msu.edu/~reusch/VirtualText/Spectrpy/nmr/nmr1.htm).

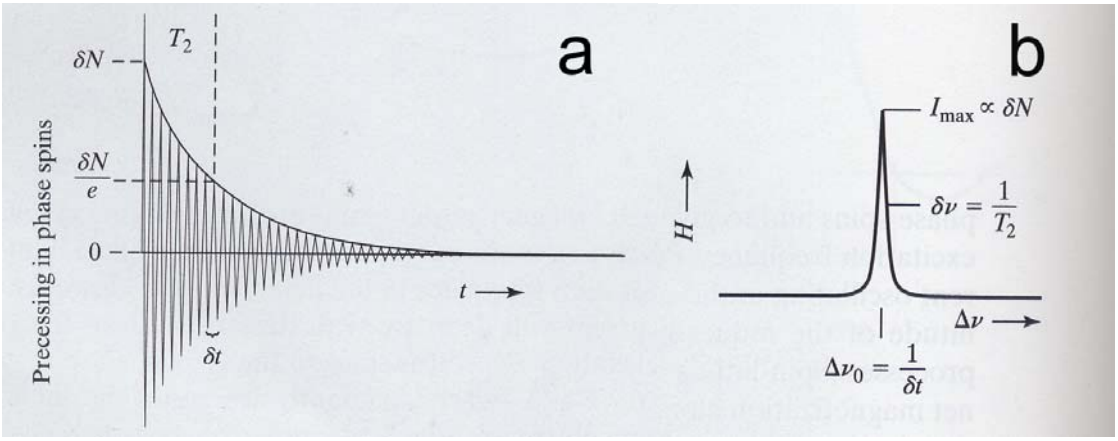

Figure 1.8: A Fourier transform (FT) converts the time domain behavior of the signal produced by the sample (a) with a single frequency ν_0 into the frequency domain (b) (Van Holde et al., 1998).

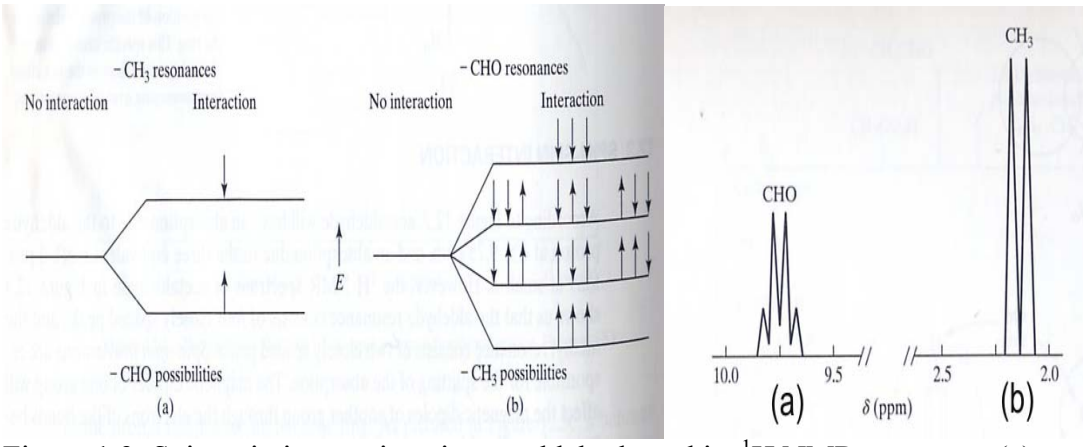

Figure 1.9: Spin-spin interactions in acetaldehyde and its ^{1}H NMR spectrum. (a) arrangements for the –CHO proton causing two resonances for $–CH_3$ and (b) arrangements for the $–CH_3$ protons causing four resonances for –CHO) (Van Holde et al., 1998).

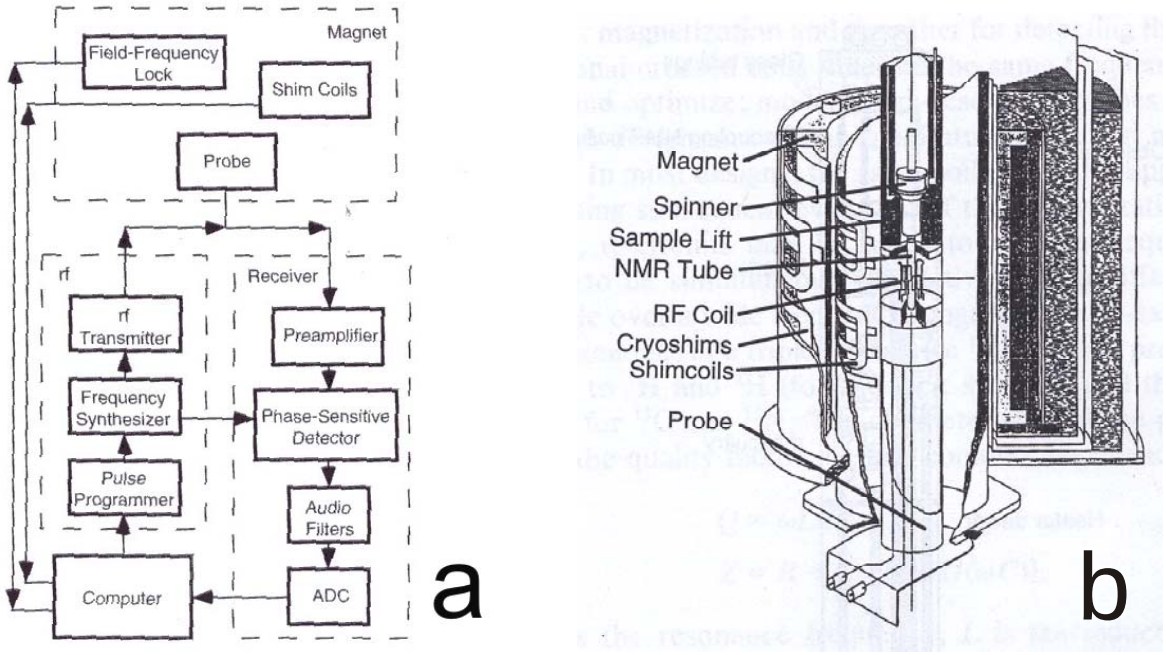

Figure 1.10: a) Block diagram of a typical Fourier Transform (FT) NMR spectrometer. b) Cutaway diagram of a superconducting magnet (Cavanagh et al., 1996).

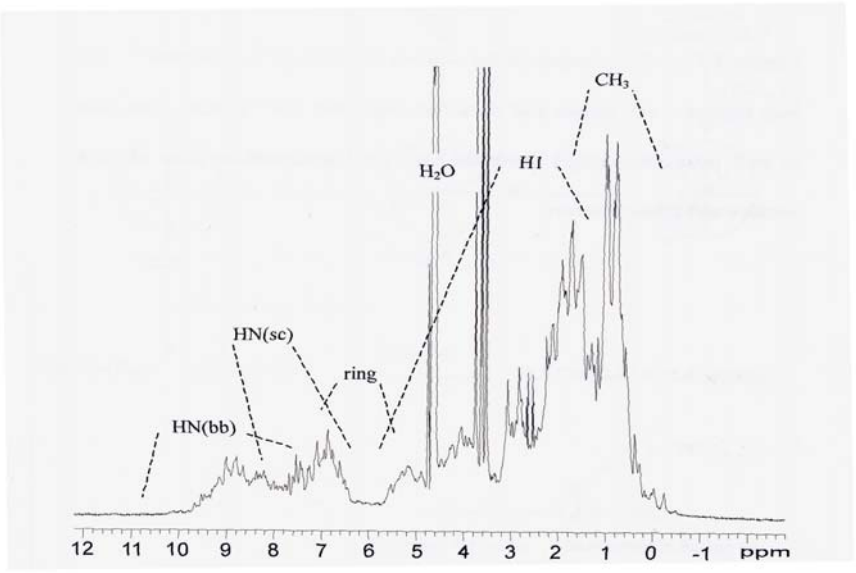

Figure 1.11: The ^{1}H 1D NMR of $^{13}C/^{15}N$ apo-L-FABP at pH 6.0 and 30 $^{\circ}C$ obtained on a 600 MHz instrument (He, 2000; *Ph.D thesis*).

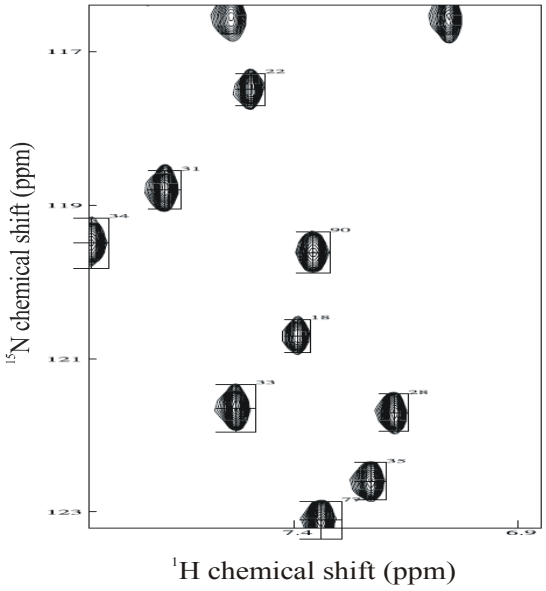

Figure 1.12: A portion of the 2D HSQC spectrum of ^{15}N L-FABP at 20 $^{\circ}C$ and pH 7.0 obtained on a 600 MHz NMR instrument. Amide protons (HN) are represented by the x-axis, while the amide nitrogens (N) are represented by the y-axis (102104_ff_apolfabp_20C_gNhsqc, Varian 600 MHz data).

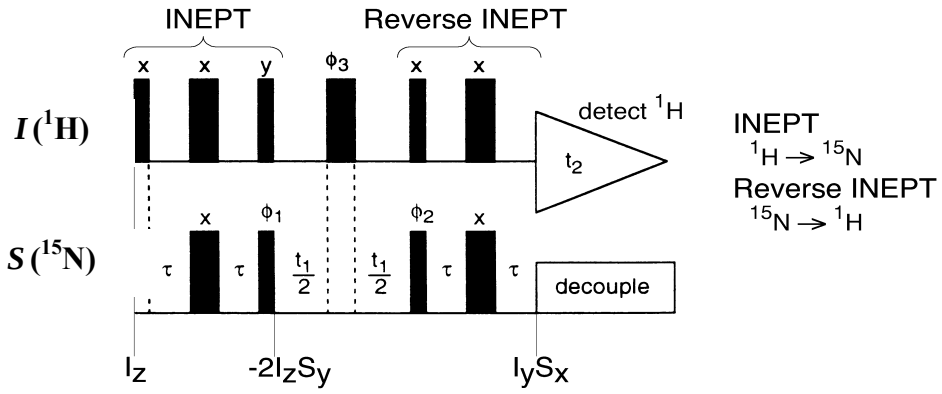

Figure 1.13: Pulse sequence for ^{1}H-^{15}N HSQC experiment using INEPT sequence to transfer magnetization from ^{1}H $\rightarrow$ ^{15}N and back again for detection (^{15}N $\rightarrow$ ^{1}H) (Mandal et al., 2004).

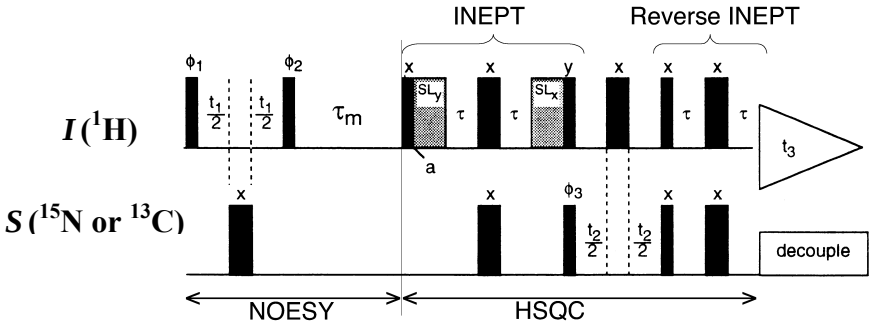

Figure 1.14: Pulse sequence for the 3D ^{1}H-^{15}N NOESY-HSQC experiment (Cavanagh et al., 1996).

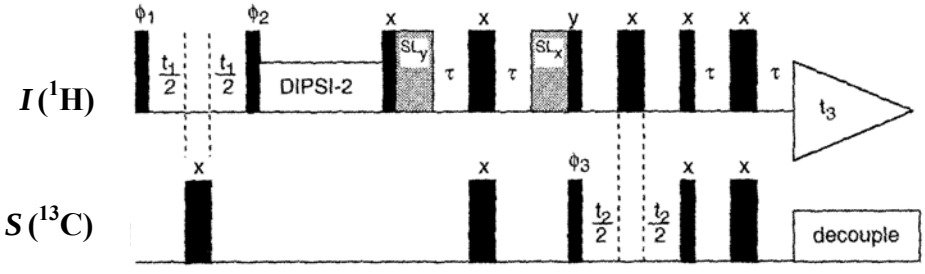

Figure 1.15: Pulse sequence for sensitivity-enhanc
ed three-dimensional Total Correlation Spectroscopy (TOCSY) (Cavanagh et al., 1996).

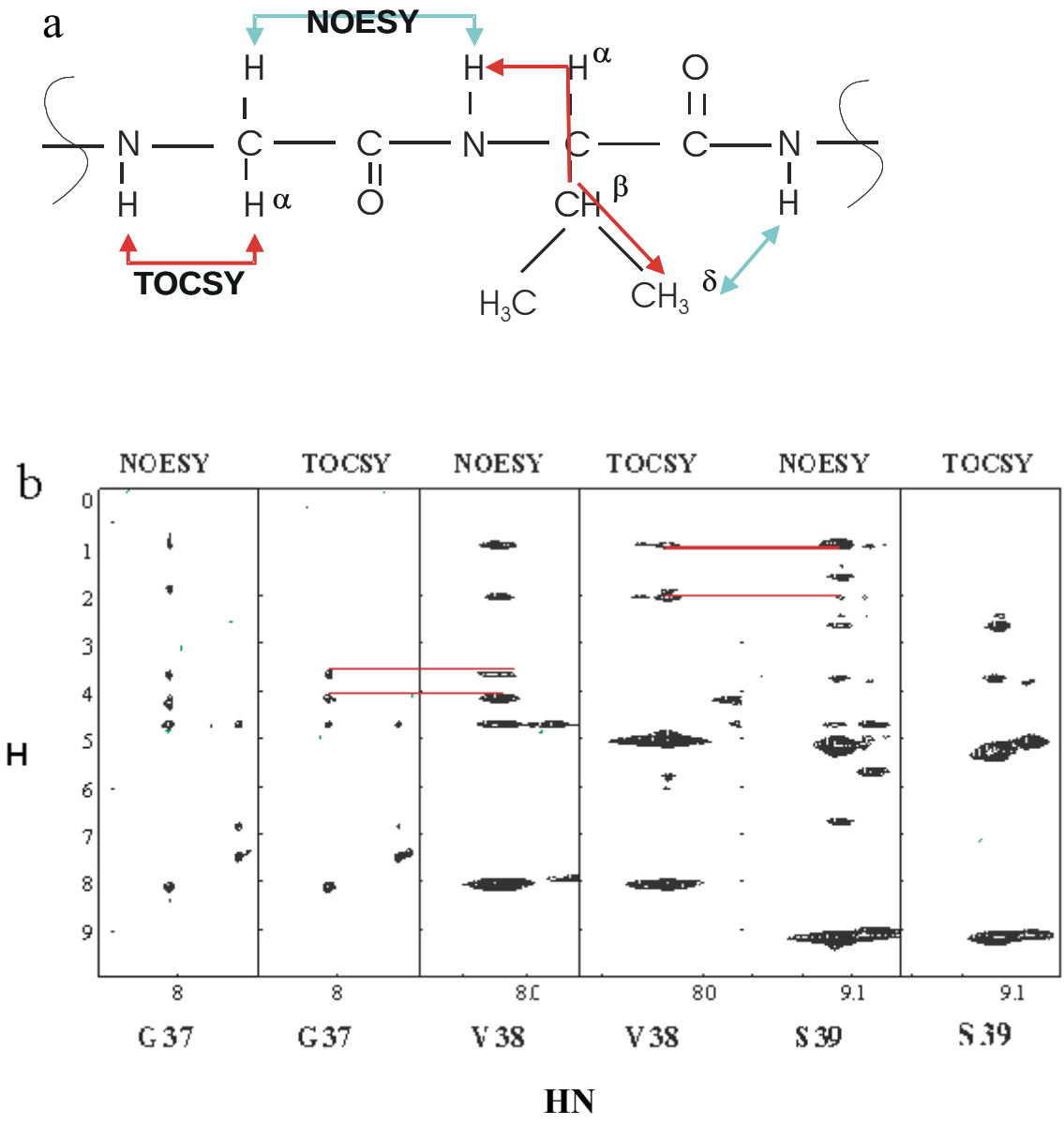

Figure 1.16: a) Segment of polypeptide chain illustrating correlations measured by 3D TOCSY-HSQC and NOESY-HSQC. b) Strip plot of sequential links from TOCSY-HSQC and NOESY-HSQC spectra of ^{15}N-apo-L-FABP at pH 7.

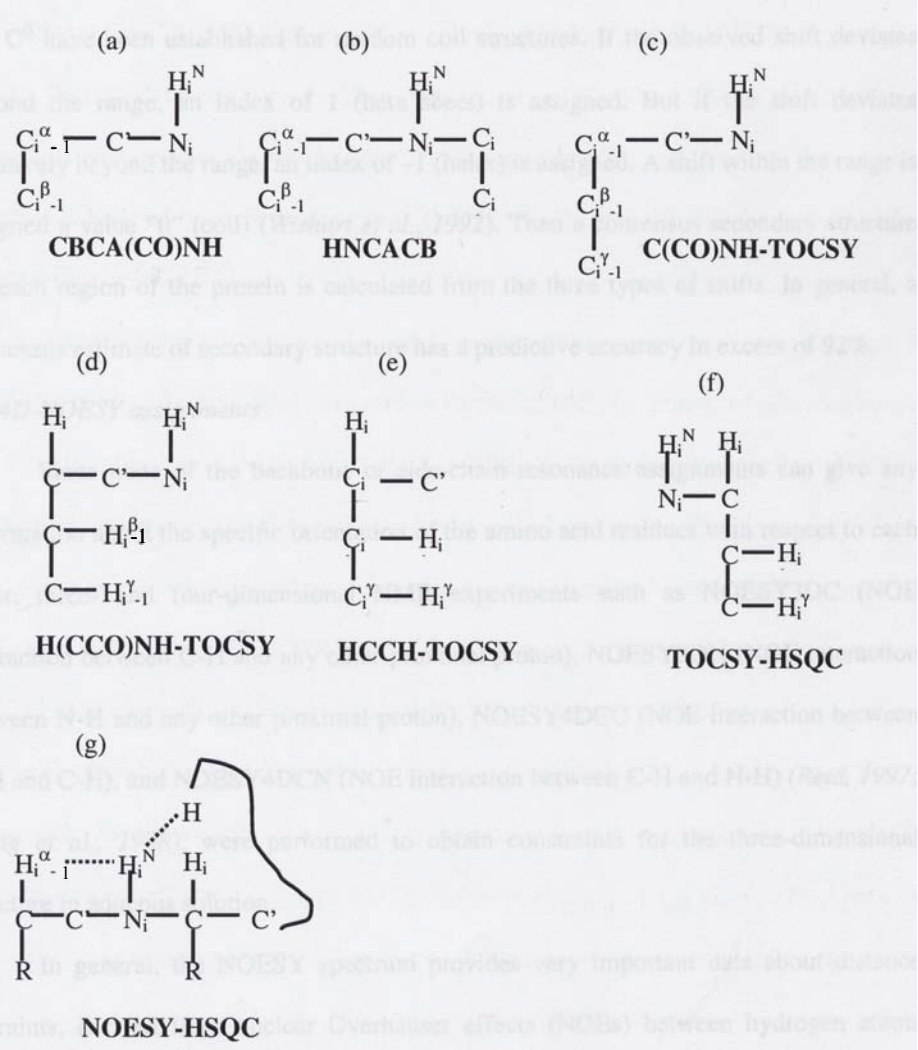

Figure 1.17: 3D experiments for I-FABP sequence-specific resonance assignments. $^{1}HN_i$, and $^{15}N_i$ represent the nuclear spins for residue (i) amide proton and amide nitrogen, respectively. $^{1}H_i^{\eta}$ and $^{13}C_i^{\eta}$ represent the nuclear spins of side chain protons and carbons, respectively. $^{13}C_i^{\eta}$ represent the ^{13}C nuclear spins ($\eta = \alpha, \beta, \gamma$, etc.) (He, 2000; *Ph.D. thesis*).

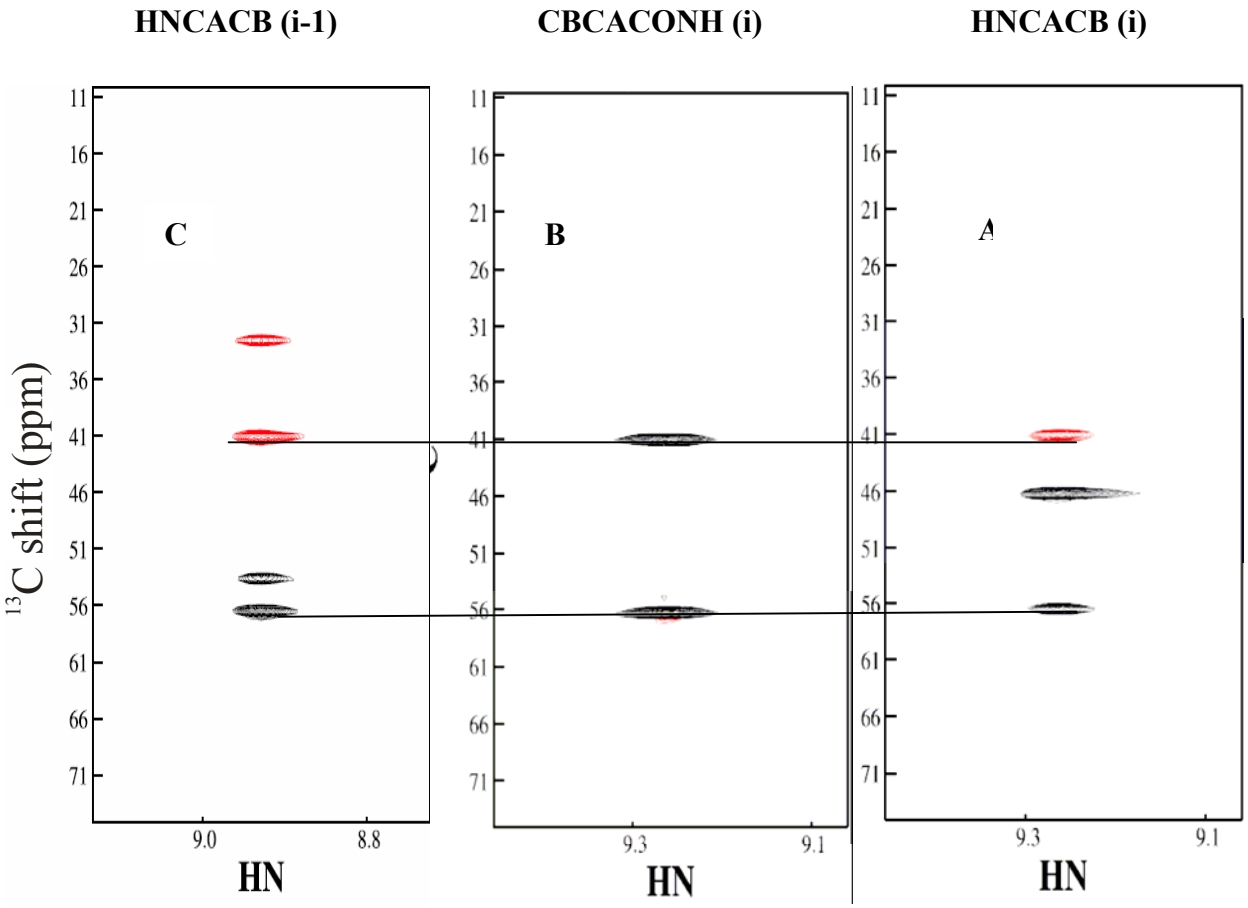

Figure 1.18: Strip plot of sequential links for residue (i) from spectra of ^{13}C ^{15}N-apo-I-FABP at pH 7 from a) HNCACB; b) CBCACONH; and their correlation with c) HNCACB for the preceding residue (i-1).

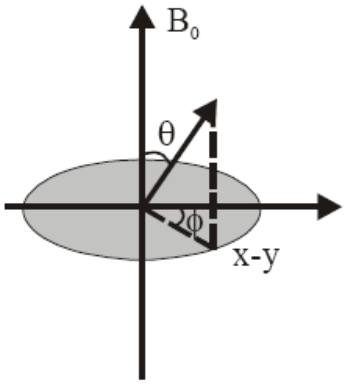

Figure 1.19: Bond vector alignment in the magnetic field for measurements of residual dipolar couplings. Angle θ is the angle between the dipolar coupling vector and the magnetic field, φ is the projection angle of the dipolar coupling vector. B_0 denotes the direction of the magnetic field (Tjandra et al., 1997).

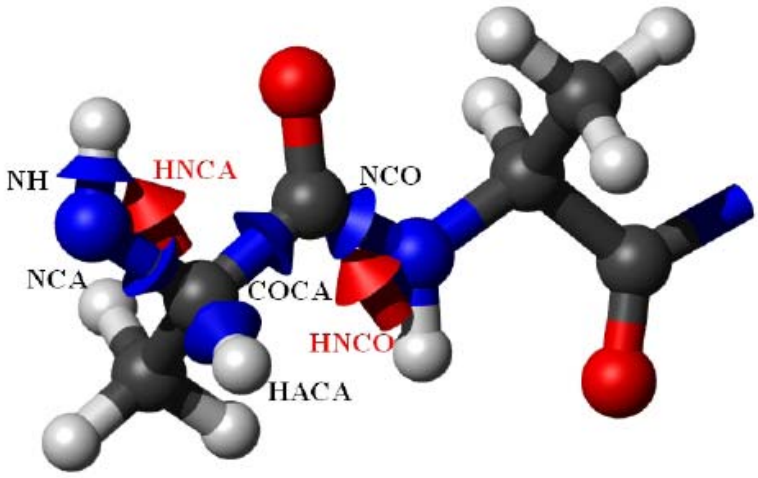

Figure 1.20: Arrows show some residual dipolar couplings that can be measured from the polypeptide backbone (Pääkkönen, 2003).

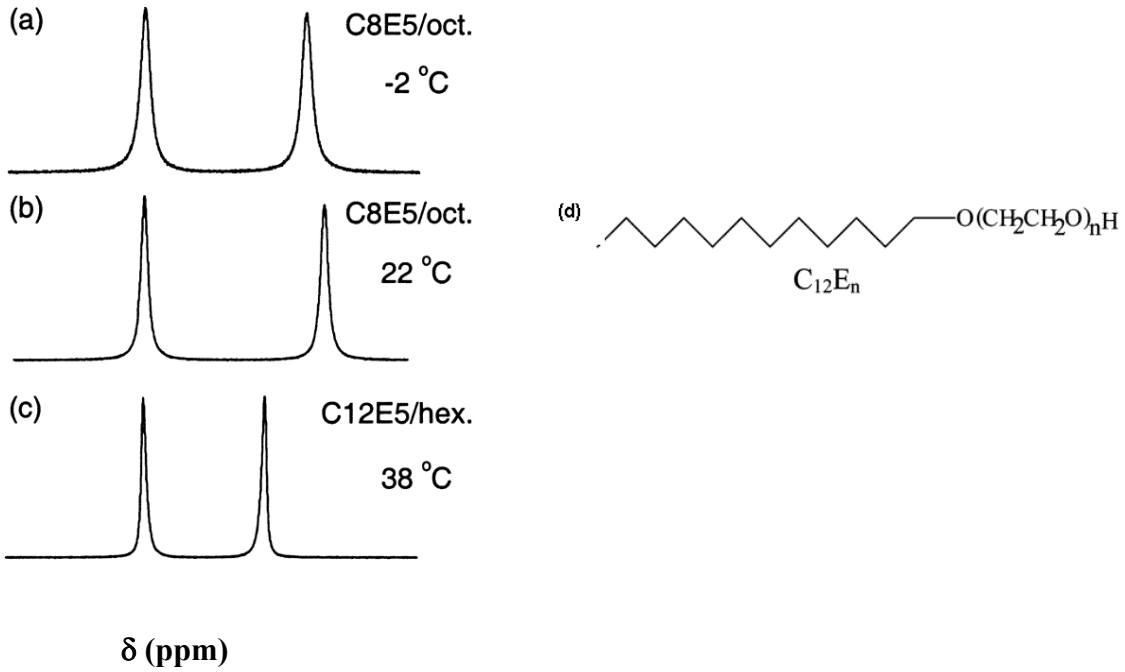

Figure 1.21: a-c) Quadrupolar splitting observed in the ^2H NMR spectra of the solvent in different dilute liquid crystalline systems: a) C_8E_5/octanol at –2 °C, b) C_8E_5/octanol at 22 °C, and c) $C_{12}E_5$/hexanol at 38 °C. d) Molecular structure of *n*-dodecyl-poly (ethylene glycol. All samples are in 90% H_2O/10% D_2O, pH 7 (Ruckert and Otting, 2000).

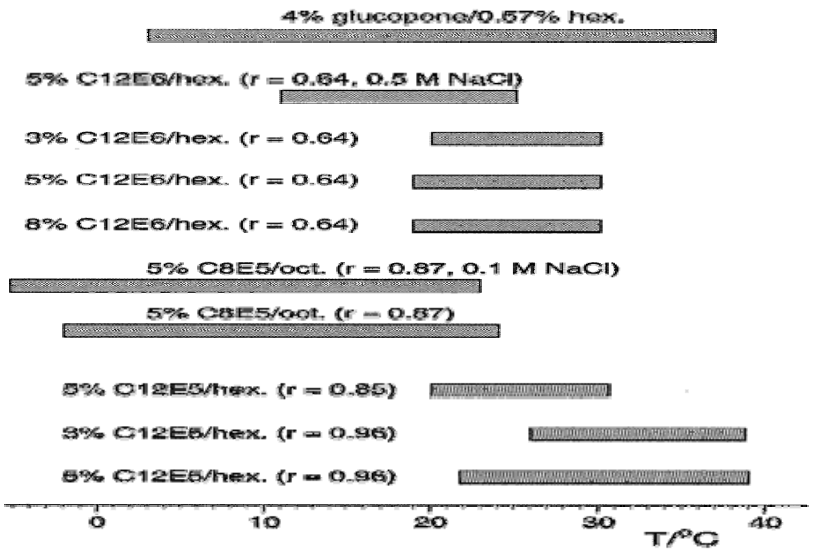

Figure 1.22: Temperature range for stable lamellar phases composed of C_mE_n/alcohol/H_2O (Ruckert and Otting, 2000).

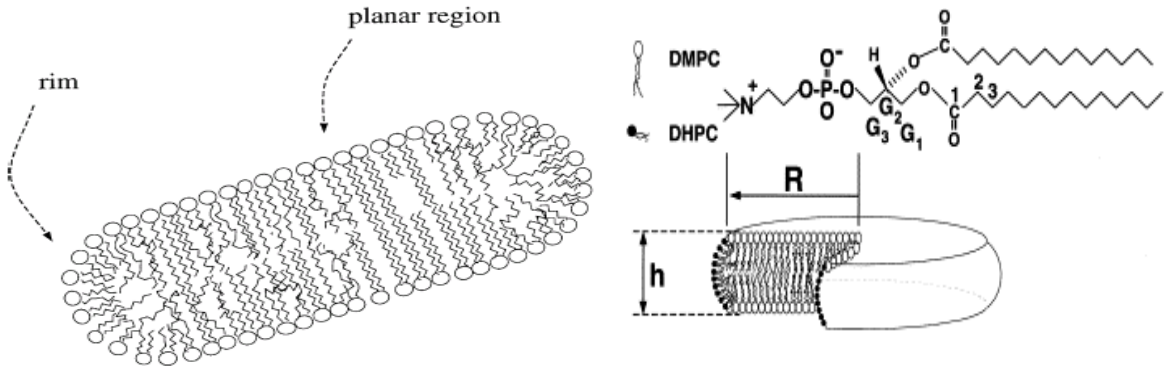

Figure 1.23: Cross sectional representation of a phospholipid bicelle. Bilayer region is composed of long-chain phospholipids, while the rim region is made of short-chain phospholipids. R is the radius of the bicellar disc and h is its bilayer thickness (Whiles et al., 2001).

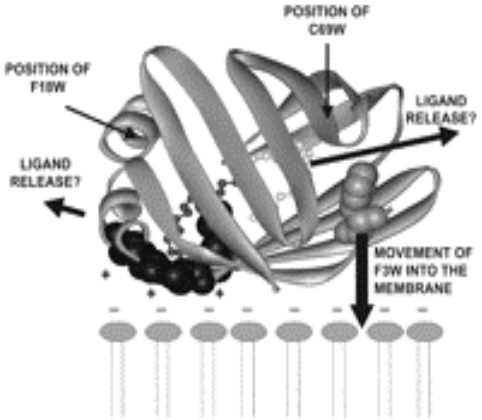

Figure 1.24: Model illustrating the possible interaction of liver FABP with an ionic phospholipid interface. The initial interaction of the cationic residues Lys-31, Lys-36, and Lys-57 is proposed to result in protein unfolding and N-terminal movement to the phospholipid interface. The conformational change disrupts the ligand binding cavity of the liver FABP, resulting in release of ligand (DAUDA) (Davies et al., 2002).

Chapter 2: Materials and Methods

Materials

^{15}N ammonium chloride, isopropyl-β-D-thiogalactoside (IPTG), Luria Broth (LB), ampicillin, Lipidex-1000, L-α-lysophosphatidylcholine (16:0 and 18:0), caprylic acid, palmitic acid, oleic acid, eicosapentaenoic acid (EPA), heme, protoporphyrin IX, cholesterol, deoxycholate, *n*-alkyl-poly (ethylene glycol), hexanol, and octanol were purchased from Sigma-Aldrich (St. Louis, MO) and used as received. Reagents (Coomassie Brilliant Blue G-250, acrylamide, N, N'-methylene-bis-acrylamide, glycerol, bromophenol blue, ammonium persulfate, N, N, N', N'-tetramethylethylenediamine (TEMED), sodium dodecylsulfate (SDS), and β-mercaptoethanol were also purchased from Sigma-Aldrich for sodium dodecyl sulfate-polyacrylamide gel electrophoresis (SDS-PAGE). The MEM vitamins solution was purchased from Invitrogen-Gibco (Carlsbad, CA). ^{3}H-oleic acid was purchased from Perkin-Elmer Life Sciences, Inc. (Boston, MA). The Sephadex^{TM} G-50 medium was purchased from Fisher Scientific (Atlanta, GA). Amicon YM-10 and Centricon 10 membranes were purchased from Millipore, Inc. (Burlington, MA). The lipids dimyristoylphosphatidylcholine (DMPC), dimyristoylphosphatidylglycerol (DMPG), dihexanoylphosphatidylcholine (DHPC), dimyristoylphosphatidylcholine (DMPC), and 1,2-di-O-hexyl-*sn*-glycero-3-phosphocholine (DIOHPC) were purchased from Avanti Polar Lipids (Birmingham, AL).

Methods

1) Protein Expression and Purification

a) Cell Culture and Protein Expression

The pET11d-I-FABP and pET11a-L-FABP expression vectors containing the cDNA of I-FABP and L-FABP, respectively, were transformed into *E. coli* host strain BL21 (DE3). For both L-FABP and I-FABP expression, 30 µl ampicillin (200 µg/ml) was spread on an agar plate (30 ml, LB/agar = 3:5 (w/w)), onto which transformed cells were streaked from –70 °C stock using a sterile toothpick. The plate was incubated at 37 °C for 14 hours. After incubation, an individual colony was picked, inoculated into 50 ml of LB containing ampicillin (1µl/1ml LB), and allowed to grow (for ~ 4-6 hours) in a shaker at 37 °C and 200 rpm to a late log phase with OD_{600} ~0.6. Cells were kept at 4 °C until the next day when they were transferred into 2 L of LB with ampicillin (1µl/1ml LB) and allowed to grow again (for ~ 2-3 hours) at 37 °C and 200 rpm to a late log phase with OD_{600} ~0.6. Cells were then centrifuged, resuspended in M9 salt and transferred into 1 L of ^{15}N (and ^{13}C in some experiments) labeled minimal media containing 200 ml of M9 salt (0.01M KH_2PO_4, 0.02M Na_2HPO_4, 0.05M NaCl, pH 7.2), 1g $^{15}NH_4Cl$, 8 ml of 50 % glucose (w/w) (or 4 g of [U-^{13}C]- glucose), 1 ml 2M $MgSO_4$, 0.2 ml 0.5M $CaCl_2$, 10 ml MEM vitamins, and 1 ml ampicillin (200µg/1ml). Cells in minimal media were then shaken at 37 °C and 200 rpm for 1 hour, after which protein expression was induced by adding 4 ml of IPTG from a 250 mM stock to yield a final IPTG concentration of 1 mM. The cell culture was then incubated at 37 °C and 200 rpm for 3 hours, after which the cells were harvested (Marley et al.

2001). 100 µl aliquots were collected before and after induction in order to examine the protein expression using SDS-PAGE. Cells were then stored at –70 °C.

b) Cell Lysis and Protein Purification

Cell pellets were thawed in an ice bath and resuspended completely in 25 ml of $T_{10}E_1K_{100}$ lysis buffer (10 mM Tris, 1 mM EDTA, 100 mM KCl, pH 7.5). Cell membranes were then broken in a Branson bath sonicator (50 % duty cycle) at 4 °C. Sonication was repeated 8 times for 30 seconds with 1 minute resting periods. Solutions were then ultracentrifuged for 45 minutes at 20,000 rpm and 10 °C. The resulting pellets were kept at –70 °C while assessing the completeness of lysis of the cells by SDS-PAGE. Meanwhile, 20 µl of [^{3}H] oleate (5 Ci/mmol) was added to the protein-containing supernatant in order to track the derived protein within the eluting fractions described below. The solution was kept at room temperature for at least 20 minutes before loading it into a size-exclusion purification column (Sephadex G-50) pre-equilibrated with a KCl-phosphate buffer (0.15 M KCl, 0.05 M K_3PO_4, and 0.02 % NaN_3, pH 7.4) at 4 °C. Fractions of 9 ml each were collected and the protein concentration of each fraction was measured by UV spectroscopy, referenced to the KCl-phosphate buffer at A_{280} and using extinction coefficients of 6400 $M^{-1}cm^{-1}$ and 16900 $M^{-1}cm^{-1}$ for L-FABP and I-FABP, respectively (Storch et al., 2000). The radioactivity was also measured for each fraction that had an absorbance > 0.01. Fractions with the highest ratio of CPM (counts per minute) to protein concentration, indicating highest FABP purity, were pooled and concentrated by ultrafiltration using an Amicon YM-10 membrane (Figure 2.1). 100 µl aliquots were collected from the protein concentrate before and after G-50 purification to check the protein purity using SDS-PAGE

(Figure 2.2). The protein concentrate was loaded into an anion-exchange chromatographic column (DE-52) that was pre-equilibrated with 10 mM Tris phosphate buffer (Tris-base and Tris-HCl adjusted to pH 8.3 with H_3PO_4 at room temperature). Measurements of protein concentration and radioactivity for each fraction were repeated as described in the size-exclusion chromatography step. Fractions with the highest protein purity were pooled and concentrated to ~ 30 ml for [^{3}H] oleate delipidation.

c) Delipidation

After checking the purity of the protein, the concentrate from chromatographic purification was applied to a Lipidex-1000 column at 37 $^{\circ}$C (Glatz et al. 1985) and pre-equilibrated with KCl-phosphate buffer (0.15 M KCl, 0.05 M K_3PO_4, and 0.02 % NaN_3, pH 7.4). Protein concentration was measured by UV absorbance for the eluted fractions. All protein-containing fractions were combined and concentrated to ~30-40 ml. Two 100 µl aliquots were collected before and after each delipidation step and measured for radioactivity using a scintillation counter. Delipidation was considered complete when $CPM_{final} / CPM_{initial} < 0.03$ (> 97 % fatty acid delipidation). I-FABP and L-FABP required 1-2 and 2-3 delipidation steps, respectively, to be stripped from [^{3}H] oleate. After each delipidation step the Lipidex-1000 column was regenerated by washing the beads (composed of hydroxyalkoxypropyl Sephadex type II) from bound fatty acid as follows. 1) The beads were washed with 1 L solutions of 15, 30, 50, and 100 % methanol/water (v/v); 2) The beads were soaked in 100 % methanol for at least 30 minutes. During this last step fresh beads, pre-soaked for 10 minutes in methanol, can be added to the regenerated beads. 3) Washing was done with 1 L solutions of 50, 30, and 15 % methanol/water (v/v). 4) The beads

were washed three times with KCl-phosphate buffer (0.15 M KCl, 0.05 M K_3PO_4, and 0.02 % NaN_3, pH 7.4) before loading them onto the preheated column at 37 °C.

2) NMR and QLS Experiments

a) NMR sample preparation

Protein (L-FABP or I-FABP) was concentrated to ~ 600 µl and the desired concentration in a phosphate buffer containing 100 mM NaCl, 50mM NaH_2PO_4, 5 µM EDTA, and 0.02% NaN_3 at pH 7.0 using a Centricon 10 ultrafiltration membrane and transferred to an NMR tube. For ^{15}N-edited NMR experiments (^{15}N HSQC, ^{15}N HSQC-NOESY, and ^{15}N HSQC-TOCSY), samples were prepared in 5% D_2O and 95% H_2O to provide a signal lock. Protein concentrations ranging between 0.2 and 0.4 mM were sufficient to obtain ^{15}N HSQC and ^{15}N HSQC-NOESY spectra. However, concentrations of 0.4-1.0 mM were required for ^{15}N HSQC- TOCSY spectra. For I-FABP backbone assignment experiments in bicellar media backbone using HNCACB and CBCA(CO)NH and for side-chain assignments using HCCH-TOCSY and H(CCO)NH-TOCSY), the protein concentration ranged between 0.7 and 0.9 mM.

(i) L-FABP ligand binding

Calculated volumes from 5, 25, and 10 mM aqueous stock solutions of lyophosphatidylcholine, palmitic acid, and oleic acid, respectively, were added to three NMR samples of L-FABP, yielding protein-to-ligand ratios of 1:10, 1:2, and 1:2 for lysoPC-, palmitate-, and oleate- ^{15}N-L-FABP, respectively. In all three samples the L-FABP was concentrated from stock in a phosphate buffer containing 100 mM NaCl, 50 mM NaH_2PO_4,

5 μM EDTA, 0.02% NaN_3, and 5% D_2O at pH 7.0, to obtain a protein concentration of ~ 0.5 mM. Due to the low aqueous solubility of palmitic acid, it was dissolved in 0.1 M NaOH.

A 10 mM stock solution of caprylic acid was prepared in 25 mM NaH_2PO_4 buffer at pH 7.0 and titrated into ^{15}N-L-FABP in buffer (50 mM NaH_2PO_4, 100 mM NaCl in 0.5 ml of a 5% deuterated NMR sample), at a protein concentration of ~0.5 mM, yielding 1:1, 1:2, 1:4, and 1:10 protein-to-FA ratios.

A 20 mM stock solution of eicosapentaenoic acid (EPA) was prepared in NaH_2PO_4 buffer containing 0.1 N NaOH and titrated into ^{15}N–LFABP at a concentration of ~0.5 mM in buffer (50 mM NaH_2PO_4, 100 mM NaCl in 0.5 ml of a 5% deuterated NMR sample at pH 7.0), to yield 1:0.5, 1:1, 1:2, 1:4 and 1:5 protein-to-FA ratios.

For investigations of heme and oleate binding to L-FABP, calculated volumes of heme and oleic acid were added from a 3.2 mM stock solution in 10 mM NaOH and a 10 mM stock in 1 mM NaOH, respectively, to an NMR sample of ^{15}N–LFABP (60 μM protein in a phosphate buffer containing 50 mM NaH_2PO_4, 100 mM NaCl in 0.5 ml of a 5% deuterated NMR sample). The final protein-to-ligand ratios were 1:2 and 1:6 for L-FABP: heme and L-FABP: oleate, respectively. To remove azide for selected experiments, the protein solution was run on a PD-10 column and then concentrated with a Centricon-10 membrane. Protoporphyrin IX was dissolved in 10 mM NaOH to make a 0.746 mM stock solution and added to an NMR sample containing ^{15}N apo–L-FABP at a concentration of 47.7 μM to obtain protein-to-ligand ratios of 1:2.

For sterol binding investigations, deoxycholate was added from a 10 mM aqueous stock solution to ^{15}N–L-FABP (same buffer as above) to yield an NMR sample with a 1:2 protein-to-ligand ratio. Cholesterol was dissolved in $CDCl_3$ to yield a 12 mM stock, from which an aliquot

was added to the bottom of an NMR tube and dried with N_2 gas. ^{15}N–L-FABP was then added to the NMR sample to yield a 1:10 protein-to-cholesterol ratio.

For phospholipid binding investigations, DHPC was added from a 10 mM aqueous stock solution to ^{15}N–L-FABP, yielding an NMR sample with 1:10 protein-to-ligand ratio. DMPC was dissolved in $CDCl_3$ to yield a 1 mM stock, from which an aliquot was added to the bottom of an NMR tube and dried with N_2. ^{15}N–L-FABP was then added to the NMR sample, yielding a 1:10 protein-to-DMPC ratio.

(ii) Weakly aligning media

The liquid crystalline phase of *n*-dodecyl-pentaethylene glycol ($C_{12}E_5$) (Figure 1.19d) was prepared by dissolving $C_{12}E_5$ in 90% H_2O/10% D_2O, adjusting the pH to 7.0, and adding a calculated volume of hexanol with vigorous shaking to obtain a final composition of 15 % $C_{12}E_5/H_2O$ (w/w) and a $C_{12}E_5$/hexanol molar ratio of 0.96. The liquid crystalline phase of C_8E_5 was prepared by dissolving C_8E_5 in 90% H_2O/10% D_2O containing 0.1 M NaCl, adjusting the pH to 7.0, and adding a calculated volume of octanol, with vigorous shaking, to obtain a final composition of 15 % C_8E_5/H_2O (w/w) and a C_8E_5/octanol molar ratio of 0.87.

For weak alignment of apo-L-FABP, A 15 % (w/w) solution of a q = 3.0 DMPC/DHPC bicelle was added to an NMR sample containing ^{15}N-apo-L-FABP to yield a final lipid concentration of 5 % (w/w) and examined at 10 $^{\circ}$C, 20 $^{\circ}$C, and 30 $^{\circ}$C. Also, in separate experiments, $C_{12}E_5$/hexanol was added to ^{15}N-apo-L-FABP in a phosphate buffer (50 mM NaH_2PO_4, 100 mM NaCl in a 0.5 ml NMR sample) to yield a final $C_{12}E_5$/hexanol concentration

of 5 % (w/w) and a protein concentration of 0.4 mM. For weak alignment of holo-L-FABP, $C_{12}E_5$/hexanol and C_8E_5/octanol were added to 2 OLA holo-oleate ^{15}N- L-FABP samples, each in a phosphate buffer (50 mM NaH_2PO_4, 100 mM NaCl in 0.5 ml NMR sample) to yield final $C_{12}E_5$/hexanol and C_8E_5/octanol concentrations of 5 % (w/w) and final protein concentrations of 0.5 mM. All NMR experiments were conducted at 30 $^{\circ}$C.

(iii) Bicelle preparation

Stock solutions of bicelles (20 % total lipid w/w in water) were prepared with the desired ratio (q = number of moles of long-chain phospholipids/number of moles of short chain phospholipids), by adding calculated weights of DMPC (for neutral bicelles) or DMPC and DMPG (for acidic bicelles) to distilled water to obtain a homogeneous slurry by 2-3 cycles of heating to 40 $^{\circ}$C and cooling in an ice bath. An aqueous solution of DHPC, prepared and kept at 4 $^{\circ}$C overnight, was then added to the slurry and mixed by two cycles of centrifugation and vortex-induced resuspension in order to obtain a clear homogeneous solution with the desired q. The stock was kept in the freezer until use. The bicelles were made anionic by adding DMPG, so that (DMPG) /[(DMPG)+(DMPC)] = 1/3 (Davies et al. 1999). Ether-linked bicelles were made by replacing DHPC and DMPC by DIOHPC and DIOMPC, respectively. For magnetic alignment, bicelles were made with q equal to 3.0 (q = [DMPC] / [DHPC] = 3.0). For membrane-mimetic invetigations both neutral and acidic bicelles were prepared, with q equal to 0.5 for NMR experiments and q values of 0.2, 0.5, and 1.0 for quasielastic light scattering (QLS) measurements.

(iv) Bicelle titration

Titrations of 0.1, 0.2, 0.4, and 0.8 mole equivalent of acidic or neutral bicelles were made into an NMR sample containing ^{15}N-L-FABP or ^{15}N-I-FABP in a low salt phosphate buffer (10 mM NaH_2PO_4, 50 mM NaCl in 0.5 ml of 5% D_2O at pH 7.0) or a high salt phosphate buffer (50 mM NaH_2PO_4, 100 mM NaCl in 0.5 ml 5% D_2O at pH 7.0) at 10 ° C and 20 ° C. Molar equivalents with respect to protein assumed that 1 isotropic bicelle with q = 0.5 contained ~100 molecules of total lipids, as calculated from the bicelle dimensions and the volumes of DMPC and DHPC (Andersson, 2005; Nagle and Tristram-Nagle, 2000).

For resonance assignments of I-FABP in a bicellar medium, 0.4 equivalent of neutral bicelles were added to an NMR sample containing ^{13}C, ^{15}N-I -FABP in a low salt phosphate buffer (10 mM NaH_2PO_4, 50 mM NaCl in 0.5 ml of 5% D_2O at pH 7.0).

b) NMR experiments

All data were collected on a four-channel Varian ^{UNITY}INOVA 600 MHz spectrometer (Varian NMR Inc., Palo Alto, CA) equipped with a triple-resonance probe and z-axis pulsed field gradients, unless otherwise noted. In all experiments, the ^{1}H carrier frequency was placed on resonance with the H_2O signal. The H_2O signal, and thus the carrier frequency, was calculated from the equation: $\delta(H_2O) = 7.83 - T/96.9$ ppm (Cavanagh et al., 1996), where T is the absolute temperature and δ is the resonance frequency in ppm.

(i) HSQC

For L-FABP ligand-binding experiments, data were collected at 30 ° C. The ^{1}H carrier frequency was placed on resonance with the H_2O signal at 4.71 ppm for solvent suppression by presaturation experiments. Chemical shift referencing was made to DSS (sodium 2,2-dimethyl-2-silapentane-5-sulfonate), which corresponds to 0 ppm for ^{1}H (Wishart et al., 1995). Two-dimensional ^{15}N-edited HSQC acquisition parameters (spectral widths (sw_1) and (sw_2) in Hz, numbers of complex points (t_1) and (t_2)) are summarized for apo-L-FABP with oleic, palmitic, caprylic, and eicosapentaenoic acids, lysophosphatidylcholine, cholesterol, deoxycholate, heme, and protoporphyrin IX (Table 2.1).

For membrane mimetic experiments with L-FABP and I-FABP, data were collected at 10 ° C and 20 ° C, respectively, with the ^{1}H carrier frequency placed at 4.91 and 4.81 ppm, respectively, for solvent suppression. Two-dimensional ^{15}N-HSQC data were acquired for apo-L-FABP, holo (oleate)-L-FABP, and apo-I-FABP with spectral widths of 4000 and 2000 Hz, 1024 and 512 complex points in the ^{1}HN and ^{15}N dimensions, respectively.

(ii) IPAP-HSQC

For measurements of residual dipolar couplings (RDCs) of L-FABP in $C_{12}E_5$/hexanol and C_8E_5/octanol weakly aligning media, NMR spectra were recorded on a Varian spectrometer operating at a ^{1}H resonance frequency of 600 MHz for ^{1}H. IPAP (in phase-anti-phase)-HSQC experiments (Ottiger et al., 1998) were run at 30 $^{\circ}C$; the liquid crystalline state was identified by the quadrupolar splittings observed in the ^{2}H NMR spectra (Figure 1.19 a-c). One-bond ^{1}H-^{15}N

coupling constants were measured from ^{15}N HSQC spectra and recorded without decoupling, in the presence and absence of weakly aligning media (Ottiger et al. 1998).

(iii) TOCSY

Three-dimensional ^{15}N-HSQC-TOCSY (Heteronuclear Single Quantum Coherence- Total Correlation Spectroscopy) experiments were recorded and examined in conjunction with HSQC data sets to supplement the backbone amide assignments made by inspection. NMR data were acquired with spectral widths of 4000, 8000, and 2000 Hz, and 512, 256, and 128 complex points in the ^{1}HN, ^{1}HA, and ^{15}N dimensions, respectively, for apo-L-FABP with EPA. Data were acquired in caprylic acid titration experiments, as well as in bicelle titrations, for both L-FABP and I-FABP with spectral widths of 4500, 9000, and 2000 Hz, and 512, 256, and 128 complex points in the ^{1}HN, ^{1}HA, and ^{15}N dimensions, respectively. All experiments were run with a 60 ms mixing time to allow magnetization transfer among J-coupled protons.

(iv) NOESY

Three-dimensional ^{15}N-HSQC-NOESY (Heteronuclear Single Quantum Coherence- Nuclear Overhauser Effect Spectroscopy) experiments were also recorded and examined in conjunction with HSQC data sets to supplement the backbone amide assignments. Data were acquired with spectral widths of 4000, 8000, and 2000 Hz, and 512, 256, and 128 complex points in the ^{1}HN, ^{1}HA, and ^{15}N dimensions, respectively, for apo-L-FABP with EPA. Data were acquired in caprylic acid titration experiments, as well as in bicelle titration experiments, for both L-FABP and I-FABP, with spectral widths of 4500, 9000, and 2000 Hz, and 512, 256, and 128 complex

points in the ^{1}HN, ^{1}HA, and ^{15}N dimensions, respectively. All experiments were run with a 150 ms mixing time to allow cross relaxation between protons within 5 Å of each other in space.

(v) Multi-dimensional NMR experiments for backbone and side-chain resonance assignments

For resonance assignments of I-FABP in bicelle media, data were collected on a Bruker 800 MHz instrument (Bruker Biospin, Billerica, MA) at 20 ° C at the New York Structural Biology Center (NYSBC) with the ^{1}H carrier frequency placed at 4.806 ppm. Data for the three-dimensional NMR experiments used in making backbone and side-chain assignments were acquired with spectral widths ((sw_1), (sw_2), and (sw_3) in Hz and numbers of complex points (t_1), (t_2), (t_3)) as summarized in Table 2.2.

c) QLS

Bicelles for quasielastic light scattering were prepared as described above for NMR experiments. Samples with q = 0.2, 0.5, and 1.0 were prepared to a final concentration of 2.8 – 3.0 % (w/w) with assistance from Dr. Yongjun Zhang and Prof. Shuiqin Zhou. Before any measurement, the sample was syringe filtered to remove dust using a 0.2 μm Supor®filtration membrane (Pall Life Sciences, East Hills, NY). QLS measurements were performed at 10 °C with an Ar-ion laser (Lexel Instruments, Fremont, CA) operating at 488 nm and with a regulated laser input power of 45 mW. The time autocorrelation function of scattered light intensity at 90° was measured with a BI-9000AT digital correlator (Brookhaven Instruments, Holtsville, NY). The mean radius and size distribution were determined for each bicelle solution using CONTIN algorithms (Koppel et al. 1972; Provencher et al. 1982; Morrison et al. 1985).

3) Data Processing and Analysis

a) Data processing and viewing using NMRPipe and NMRView programs

Raw data from the spectrometer were converted via the multidimensional spectral processing program NMRPipe (Delaglio et al. 1995), and then imported to NMRView (Johnson et al. 1994), a program used widely for the visualization and analysis of NMR data. The first step was the conversion of the 2D data of the spectrometer-formatted input file to an NMRPipe-formatted output file that contains information such as the number of data points, acquisition mode and spectral width (Figure 2.3). The FID data of the NMRPipe script output were then inspected with the NMRDraw program for phase correction. The second step was processing the FID output data of NMRPipe using a special processing script (Figure 2.4). This script, which includes parameters such as zero filling, linear prediction, phase correction (P0 and P1 values corrected in NMRDraw), as well as Fourier transform commands, used the FID output data of NMRPipe as an input. After processing, the data were output in a ".dat" file format. For 3D and 4D spectral processing, the first step was similar to that for the 2D conversion to the NMRPipe script. However, the second processing script was written by the use of a 2D in-memory transpose called xyz2pipe. An NMRView readable ".nv" format was created from the ".dat" file format that is output from script processing of the NMRPipe program (Figure 2.5).

b) Chemical shift assignments

Chemical shift assignments of the HSQC spectra started by "peak picking". This process assigns a number to each resonance signal in the two-dimensional spectrum and includes it within a "peaklist". After peak picking, resonance signals were correlated with their counterparts in a reference spectrum, in which each resonance is assigned to an amino acid of the protein sequence and a chemical group of that moiety (e.g. NH of Val 38) (Hodsdon et al., 1995; Wang et al., 1998). In addition to visual inspection, peak assignments of 2D HSQC spectra were confirmed by the 3D experiments HSQC-TOCSY and HSQC-NOESY, which display intra- and inter-residue correlations, respectively, making sequence-specific assignments possible along the protein's primary sequence. Using 3D correlations and comparison with reference data, chemical shifts were assigned for each group of vertically aligned peaks (Figure 1.16), which represent side chain protons (H_α, H_β, H_γ, …) for each backbone residue. Using both 2D and 3D data, 98-100 % of the backbone atoms were assigned to their corresponding peaks (Table 2.3). After making resonance assignments to their corresponding nuclei, data were saved in a ".str" file format.

c) Chemical shift perturbation analysis

For chemical shift perturbation analysis, the chemical shift difference between each assigned peak and its counterpart in a reference spectrum (usually the apoprotein) was measured and tabulated. The chemical shift perturbation in Hz was calculated for the combination of amide ^{1}H and ^{15}N resonances using the equation: $\Delta\delta = \text{sqrt}\,[(\Delta HN)^2+(\Delta N)^2]$ (Jakoby et al., 1993), where the HN and N perturbations are multiplied by 599.94 and 60.8, respectively. The average chemical shift perturbation for all residues was calculated by dividing the sum of the

perturbations of all the assigned residues by the number of the assigned residues in the protein sequence. Residues with perturbations greater than one standard deviation beyond the average were color coded on a tertiary structure representation using the program MOLMOL for display (Koradi, et al., 1996). A chemical shift perturbation bar plot was also used, displaying the residue numbers on the x-axis and their respective perturbation values in Hz on the y-axis (Figure 2.6).

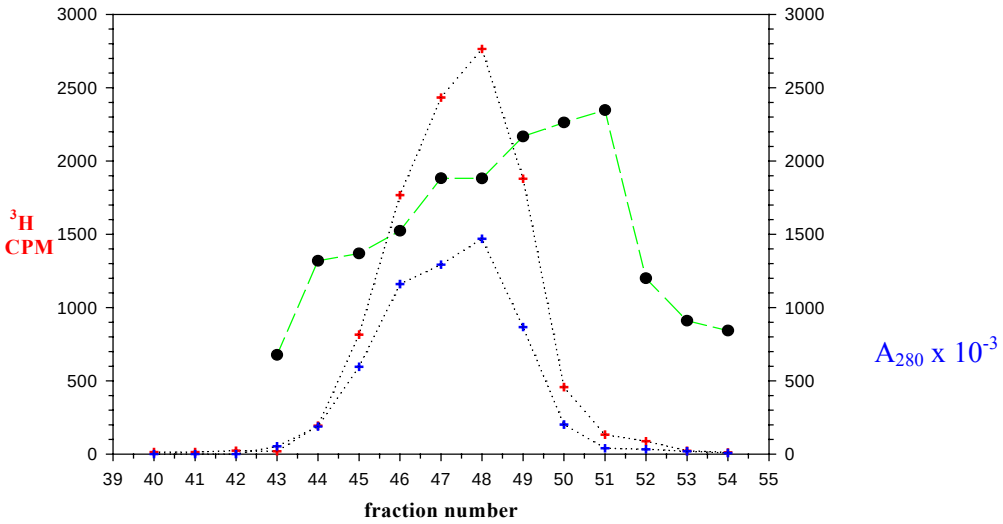

Figure 2.1: Plots of [^{3}H] oleate scintillation counts (red cross) and UV absorbance at 280 nm (blue cross) of cell lysate elution fractions 40 to 60 from a DE-52 ion-exchange chromatography column. Fractions 44-51, with the highest ratio of radioactive cell count per minute (CPM) to protein concentration (green symbols), contain the largest amounts of pure ^{15}N-I-FABP.

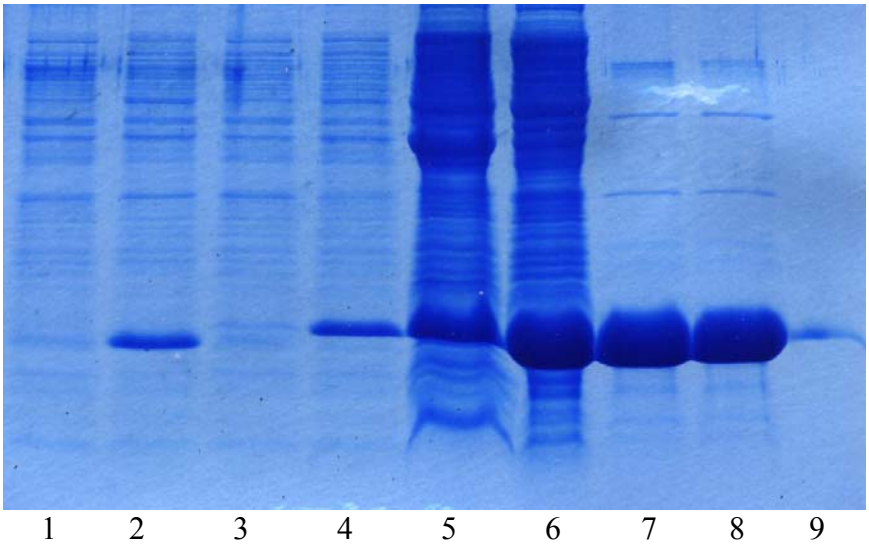

Figure 2.2: Bands from SDS-PAGE showing FABP overexpression and purification. Lanes 1 and 2: expression of ^{15}N-L-FABP before and after IPTG induction; lanes 3 and 4: expression of ^{15}N-I-FABP before and after IPTG induction; lanes 5 and 6: pellet and supernatant of the cell culture lysate of ^{15}N-I-FABP, respectively; lane 7: ^{15}N-I-FABP after G-50 purification step; lane 8: ^{15}N-I-FABP after DE-52 purification step; lane 9: a 14 kDa marker (α-lactalbumin).

```
#!/bin/csh

var2pipe -in ../../vdata/060106_ff_apoifabp_0.8eq_acidbc_hisalt.hsqc.fid/fid \
  -xN               1024  -yN                256  \
  -xT                512  -yT                128  \
  -xMODE         Complex  -yMODE         Complex  \
  -xSW          9000.900  -ySW          2200.000  \
  -xOBS          599.942  -yOBS           60.799  \
  -xCAR            4.810  -yCAR          120.540  \
  -xLAB               HN  -yLAB                N  \
  -ndim                2  -aq2D           States  \
  -out ../FID/060106_ff_apoifabp_0.8eq_acidbc_hisalt.fid
-verb –ov
```

Figure 2.3: A file for the conversion of raw FID data from an ^{15}N-edited HSQC experiment on a 600 MHz Varian instrument into an NMRPipe script.

```
#!/bin/csh

# Basic 2D Phase-Sensitive Processing:
#   Cosine-Bells are used in both dimensions.
#   Use of "ZF -auto" doubles size, then rounds to power of 2.
#   Use of "FT -auto" chooses correct Transform mode.
#   Imaginaries are deleted with "-di" in each dimension.
#   Phase corrections should be inserted by hand.

nmrPipe -in ../FID/060106_ff_apoifabp_0.8eq_acidbc_hisalt.fid\
| nmrPipe  -fn SOL -fl 32                        \
| nmrPipe  -fn SP -off 0.45 -end 1.0 -pow 2 -c 0.5    \
| nmrPipe  -fn ZF -auto                          \
| nmrPipe  -fn FT -auto                          \
| nmrPipe  -fn PS -p0 123.0 -p1 0.00 -di -verb       \
| nmrPipe  -fn EXT -left -sw            \
| nmrPipe  -fn POLY -auto -ord 0              \
| nmrPipe  -fn TP                               \
| nmrPipe  -fn LP -x1 1 -xn 128 -ord 10 -f -pred 128 -after \
| nmrPipe  -fn SP -off 0.45 -end 1.00 -pow 2 -c 0.5   \
| nmrPipe  -fn ZF -auto                          \
| nmrPipe  -fn FT -auto                          \
| nmrPipe  -fn PS -p0 -90.0 -p1 180.0 -di -verb         \
#| nmrPipe  -fn CS -ls 24 -sw                    \
  | nmrPipe  -fn TP                  \
-ov -out ../DATA/060106_ff_apoifabp_0.8eq_acidbc_hisalt.dat
```

Figure 2.4: A spectral processing script file for the conversion of FID data from an NMRPipe script for an ^{15}N-edited HSQC experiment on a 600 MHz Varian instrument into a ".dat" file format.

```
#! /bin/csh
# from Micah Gearhart <micah@scripps.edu>

set infile = $1
nmrPipe -in ../pipe/DATA/$infile.dat  \
| pipe2xyz -out MAT/$infile.nv -nv -verb
```

Figure 2.5: Conversion script for an ".dat" file format into a NMRView readable ".nv" format.

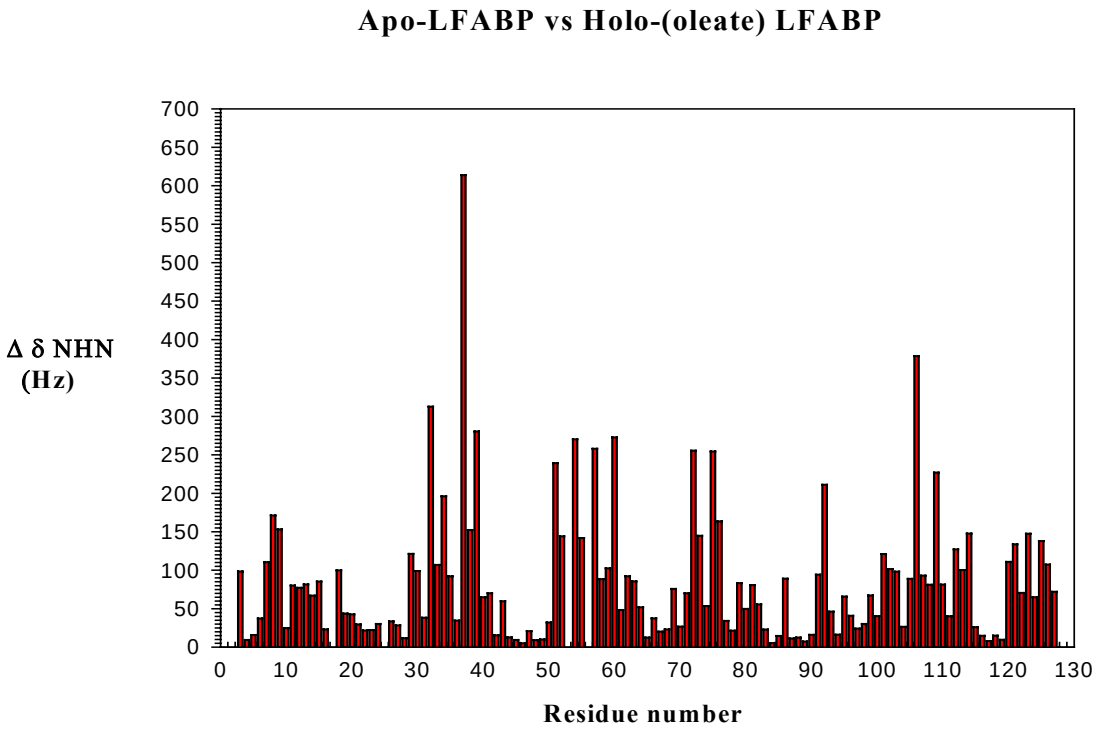

a

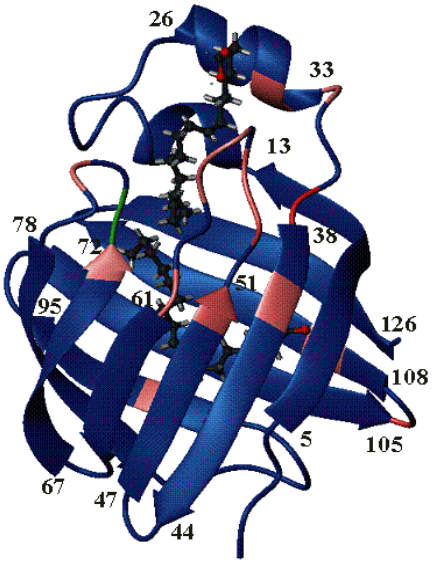

b

Figure 2.6: (a) Chemical shift perturbation bar plot of ^{15}N Apo-LFABP with 2 equivalents of added oleic acid. Calculated average perturbation is 89.2 ± 93.2 Hz. (b) Crystal structure of Holo-(oleate)-L-FABP highlighted with chemical shift perturbation as compared with apo-L-FABP at pH 7. Areas in red indicate residues with perturbation greater than one standard deviation beyond the mean.

Table 2.1: Acquisition parameters for 2D HSQC ligand-binding experiments on ^{15}N-apo-L-FABP.

N-L-FABP/ligand	Nucleus F_1/F_2	Complex data points t_1/t_2	Spectral width kHz $sw_1/sw_2/sw_3$
Oleic acid	^{1}HN/^{15}N	1024/512	4.0/2.0
Palmitic acid	^{1}HN/^{15}N	1024/512	4.0/2.0
Caprlylic acid	^{1}HN/^{15}N	1024/512	4.5/2.0
Eicosapentaenoic acid	^{1}HN/^{15}N	1024/512	4.5/2.0
Lysophosphatidylcholine	^{1}HN/^{15}N	1024/512	4.5/2.0
Cholesterol	^{1}HN/^{15}N	1024/512	4.5/2.0
Deoxycholate	^{1}HN/^{15}N	1024/512	4.5/2.0
Heme	^{1}HN/^{15}N	2048/512	4.5/2.0
Protoporphyrin IX	^{1}HN/^{15}N	2048/512	4.5/2.0

Table 2.2: Acquisition parameters for 2D and 3D experiments on ^{13}C-^{15}N-apo-I –FABP with and without bicelles

Experiment	Nucleus $F_1/F_2/F_3$	Complex data points t_1/t_2	Spectral width kHz $sw_1/sw_2/sw_3$
HNCACB	^{1}HN/^{15}N/^{13}C	1024/34/75	12.0/27.6/15.1
CBCA(CO)NH	^{1}HN/^{15}N/^{13}C	1024/34/75	12.0/27.6/15.1
HCCH-TOCSY	^{1}HN/^{15}N/^{13}C	1024/128/60	11.1/15.1/9.6
H(CCO)NH-TOCSY	^{1}HN/^{15}N/^{13}C	1024/128/60	12.0/27.6/10.9
HNCA	^{1}HN/^{15}N/^{13}C	1024/60/60	12.0/27.6/4.8
HNCO	^{1}HN/^{15}N/^{13}C	1024/64/64	12.0/27.6/10.9
2D aliphatic	^{1}HN/^{13}C	1024/128	11.2/6.4

Table 2.3: Degree of completeness for backbone resonance assignments of L-FABP with bound ligands.

apo-L-FABP w/ oleate	atom		
	HN	N	H^{α}
# Expected	123	123	-
# Assigned	123	123	-
% Completion	100	100	-

a

apo-L-FABP w/ palmitate	atom		
	HN	N	H^{α}
# Expected	123	123	-
# Assigned	122	122	-
% Completion	99.1	99.1	-

b

apo-L-FABP w/ caprylate	atom		
	HN	N	H^{α}
# Expected	123	123	130
# Assigned	121	121	119
% Completion	98.4	98.4	91.5

c

apo-L-FABP w/ EPA	atom		
	HN	N	H^{α}
# Expected	123	123	130
# Assigned	121	121	128
% Completion	98.4	98.4	98.4

d

apo-L-FABP w/ lysoPC	atom		
	HN	N	H^{α}
# Expected	123	123	-
# Assigned	122	122	-
% Completion	99.1	99.1	-

e

Chapter 3 : Results and Discussion

1) L-FABP Ligand Binding

In order to examine L-FABP ligand-binding specificity, NMR chemical shift perturbation data were acquired and mapped for L-FABP with both fatty acid and non-fatty acid molecules that have been reported to interact with and be accommodated within its binding cavity. Our strategy is to compare the results with data from X-ray crystallography for L-FABP with two bound oleates, in order to identify regions of the protein's tertiary structure that interact favorably with the putative ligand and determine ligand-binding site(s). Also, in the case of weakly binding ligands (e.g., caprylate), a binding constant can be determined from chemical shift titrations for highly perturbed L-FABP regions. Based on these data, we will be able to determine the residues that are responsible for ligand binding to L-FABP and compare their interactions with different types of ligands. This information in turn should provide insights into the relation between ligand binding of L-FABP and its various physiological roles in the cell.

The ligands examined in this study include fatty acids of short, long, and very long chain length, designed to exemplify potentially varying accommodation in the binding cavity. The binding of lysophospholipids is compared with that of long-chain fatty acids (e.g., oleate, 18:1), because both are products of lipid membrane hydrolysis and, if present in elevated concentrations, can cause cellular damage (Kaikaus et al., 1990; Vancura et al., 1992). Reported binding of non-fatty acid ligands is also examined by NMR: binding of heme to L-FABP as compared with oleate binding, L-FABP binding to sterols, and L-FABP binding to diacyl phospholipids with varying chain length.

a) Long-chain fatty acids and lysophospholipids

When parallel HSQC experiments were conducted for apo-L-FABP with two equivalents each of oleic acid, palmitic acid, and lysophosphatidylcholine (lysoPC), chemical shift perturbation analysis with apo-L-FABP as a reference (Table 3.1) revealed the most perturbed residues to be located in analogous regions of the protein's tertiary structure (Figure 3.1). The perturbations, which were localized in the portal region as well as selected regions of the internal cavity, may be large enough (mean of 0.23 and 1.84 ppm in the HN and N dimensions, respectively) to indicate possible changes in global structure (in addition to local changes in chemical environment, due for example to water occupancy or interactions with polar ligand moieties) in these perturbed regions (Kim et al., 1996). Although there are no analogous published studies with lysophospholipids for other FABPs, Davies et al. (2002) have proposed electrostatic interactions of lysophopholipids with K20, K31, and K33 of helix-II of L-FABP. The chemical shift perturbations of lysoPC-L-FABP versus palmitate-L-FABP and oleate-L-FABP were observed to be 9.8 ± 7.1 Hz and 10.9 ± 9.3 Hz, respectively, whereas the chemical shift perturbation of palmitate-FABP versus oleate-L-FABP was 13.1 ± 11.7 Hz (Figure 3.2). These small differences among the three holo-proteins along with similar locations of the perturbations to the protein structure both support the conformational similarity of L-FABP complexed to the three bound ligands.

In the HN HSQC spectrum of lysoPC-L-FABP, each residue is represented by one resonance, except for seven residues that each display two peaks. Additional sites with more than one magnetic environment may be present but could be obscured due to spectral overlap or low signal intensity. Because each of these peaks coincides with a corresponding resonance in either

oleate (18:1) -L-FABP or palmitate (16:0)-L-FABP, they may be attributed to the presence of both stearoyl (18:0)- and palmitoyl (16:0)- lysoPC reported by the vendor to be present in commercial L-α- lysophosphatidylcholine from egg yolk. The largest chemical shift perturbation was observed for Met 74 (Figure 3.3). One Met 74 peak coincides with a corresponding peak in the HSQC spectrum of palmitate-L-FABP and the other with a corresponding peak in the HSQC spectrum of oleate-L-FABP. Thus, there are likely to be two L-FABP populations, one bound to stearoyl-lysoPC and another that binds palmitoyl-lysoPC. The intensity for each resolved peak should reflect its relative amount in the sample. For example, peak intensity measurements yield 84% palmitoyl- and 16% stearoyl-lysophosholipid (peaks 1 and 2 for Met 74 in Figure 3.3), respectively (Table 3.2). These measurements indicate the ratio of stearoyl-lysoPC to palmitoyl-lysoPC is 1:5.

In order to compare our results with expectations based on the crystal structure of L-FABP with two bound oleates (Thompson et al., 1997), chemical shift perturbation data were plotted for residues that lie within 5 Å of the two oleate chains (Figure 3.4). Of these residues, only Ser39 and Glu72 of the internal binding site and Gly32, Tyr54, and Lys57 of the portal site display larger than a standard deviation beyond the mean perturbation. Moreover, some residues reported from the crystal structure to bind oleate nevertheless display small perturbations. For example, Ile41, Phe63, and Val93 of the internal binding site and Leu28 and Lys31 of the portal site have smaller than average chemical shift perturbations. It is possible that changes in water occupancy counteract some ligand-associated environmental changes or that ligands exert their effects on the side chains of proximal amino acids rather than on backbone sites.

The chemical shift perturbation values from the HSQC spectra of L-FABP with nearby residues in oleate, palmitate and lysoPC were found to agree within ~ 20 % for most residues (Table 3.3), a phenomenon that suggests similar chemical environments. A notable exception is Arg122 because it is subject to environmental perturbations from ligands at both oleate-binding sites. Comparing the chemical perturbation patterns and values for lysoPC-L-FABP with those of the holo proteins containing oleate and palmitate, it is reasonable to propose a specific interaction of L-FABP with the acyl chain of lysoPC. Evidently, its non-alkyl segment causes no additional localized perturbations beyond those caused by its alkyl part. Also, close agreement between oleate-L-FABP and palmitate-L-FABP indicates that a single degree of unsaturation has a minimal effect on perturbation for residues at both binding sites (except for Met74 in the portal site).

b) Fatty acid chain length (caprylate and EPA)

In order to examine L-FABP ligand binding to short-chain fatty acids, chemical shift perturbation values were measured for the HSQC spectra of apo-L-FABP titrated with 1, 2, 4, and 10 molar equivalents (eq) of caprylic acid (8:0). When the HSQC spectra of L-FABP with 4 and 10 equivalents of caprylate were compared, it was found that most of the shift changes were negligible after addition of 4 eq. Hence, no caprylic acid was added beyond 10 eq. When the HSQC spectrum of apo-L-FABP was compared with those at various caprylate titration stages, the average chemical shift perturbation values were: 19.8 ± 21.0, 26.2 ± 23.6, 32.3 ± 28.1, and 33.4 ± 29.8 Hz for apo-L-FABP with 1, 2, 4, and 10 molar equivalents of caprylate, respectively (Figure 3.5). By contrast, the average perturbation of holo-(oleic acid) L-FABP (3 molar

equivalents) versus apo-L-FABP was equal to 89.2 ± 93.2 (Table 3.1; Figure 3.6). The three-fold larger mean perturbation for oleate-L-FABP with respect to caprylate-L-FABP reflects a larger environmental change upon long-chain fatty acid addition. However, caprylic-L-FABP and oleic-L-FABP share 10 of 14 residues with large chemical shift perturbations (> mean perturbation + 1 standard deviation) (Table 3.4), so the ligand binding sites may be similar. These highly perturbed residues are located in the portal and adjacent β–sheet regions for the two FAs, as viewed on both perturbation plots (Figure 3.6) and the three dimensional structure (Figure 3.7).

During the titration of apo-L-FABP, the HSQC spectra of caprylate-L-FABP displayed a single peak for each residue, but more than one resonance was observed for some residues of oleate-L-FABP (Figure 3.8). These observations imply fast exchange between free and bound caprylate molecules and probably weaker caprylate binding to the protein (see below). By contrast, slow exchange between free and bound oleate molecules is manifest by doubled resonances observed in the HSQC spectra of holo-(oleate)-L-FABP. The binding constant (K_d) for caprylate-L-FABP was measured from HN chemical shift variations during titration. Residues at two sites that are proposed from X-ray data to interact with the bound oleates were monitored: 1) Solvent-exposed site (Gly32, Lys33, Thr51, Gly55, Lys57, and Glu72) (Figure 3.9a-c); 2) Internal site (Ser39, Phe63, Val83, Val92, Thr102, and Ser124) (Figure 3.9 d-f). Thus, residues with large chemical shift perturbations attributable to each ligand (Table 3.4) were compared. Binding constants were determined as 1.4 ± 0.6 mM and 0.3 ± 0.1 mM for six and seven residues with large perturbations of the internal and portal sites, respectively; plots for selected residues with the largest perturbations appear in Figure 3.9d-f. A higher K_d for the

solvent-exposed portal site, which indicates weaker interactions, may be attributed to caprylate's high water solubility and fewer FA-FA hydrophobic interactions in the region where 18-carbon OLA 129 binds. K_d is diminished at the internal site but still higher than for the corresponding oleate when measured for residues in the internal cavity (Figure 3.9d-f), which include Ser39 and Ser124. These two serines were found to form, with Arg122 and bound water, a hydrogen-bonding network that stabilizes the carboxylate groups of FAs electrostatically (Thompson et al., 1997). Thus electrostatic interactions also appear to be weaker with the caprylate ligand. These K_d values should be viewed as approximate, because binding at the first (internal) site may influence the ability of the second ligand to occupy the second (portal) site.

From these results, we can propose a mechanism for caprylate interaction with L-FABP in analogy with that of oleate, which as noted above is thought to occur by electrostatic stabilization of the carboxylate group of OLA 128 with positively charged Arg122 in the binding cavity. Moreover, hydrophobic stabilization may occur between FA alkyl chains in both binding sites (Thompson et al., 1999). Although fulfillment of the electrostatic requirement may lower the K_d values for internal site residues, the free energy of the free caprylate ligand is already low because of its substantial aqueous solubility. Binding of the shorter hydrophobic caprylate chain also results in less pronounced hydrophobic stabilization and higher K_d values for portal site residues, because there are fewer interacting methylenes on each ligand.

Previous studies using the fluorescent probe ADIFAB have shown an inverse relationship between FA aqueous solubility and binding affinity to FABPs (Richieri et al., 1994). In particular, fatty acid chain length and saturation play important roles in governing the protein-FA attractive interactions. In these studies, FABPs exhibited a decrease in their FA K_d values with

increasing chain length and decreasing unsaturation for 16:0, 18:0, 18:1, 18:2, 18:3, and 20:4 fatty acids. Our data on 16:0 palmitate and 18:1 oleate did not yield a binding constant, because the protein was present entirely in the holo form after the first addition of ligand. However, large chemical shift perturbations indicative of substantial environmental changes were observed with these long-chain fatty acids. On the other hand, our calculated K_d values (0.2 - 0.7 mM and 1.0 - 2.2 mM for internal and portal sites, respectively) for caprylic acid agree with reported binding constants for < 14 carbon fatty acids. Noting K_d values that are less than 0.03 μM for 16-18 carbon FAs (Richieri et al., 1994), these data confirm FABP's overall preference for hydrophobic long chain fatty acids.

As noted above, comparison of the NMR perturbation data for caprylic-L-FABP and oleic L-FABP suggests that protein-FA interactions occur at analogous sites. However, environmental changes of lesser magnitude are induced by the short-chain caprylate, particularly in the protein's portal region consisting of helices I and II, as well as at turns C-D and E-F (Table 3.4). These findings may indicate that the "barrel lid" of the protein is less closed (compared to that of holo oleate-L-FABP) upon caprylate entrance and binding within the cavity. In turn, that trend may result from weaker interaction between helix II and the medium-length alkyl chain of caprylate.

To further evaluate chain-length effects on FA binding to L-FABP and the possible accommodation of very long-chain species within the protein's binding cavity, eicosapentaenoic acid (EPA, 20:5) was titrated into L-FABP. As with caprylic acid, no further change in chemical shift was observed after addition of five equivalents. When the HSQC spectra of EPA-L-FABP and oleate-L-FABP were compared to that of apo-L-FABP (Figure 3.10), perturbations of 62.8 ± 61.8 Hz and 89.2 ± 93.2 Hz, respectively, were observed. Of the 121 assigned residues in EPA-

L-FABP, 13 displayed perturbations that exceeded the mean by more than one standard deviation, and eight of these coincided with the residues showing large perturbations in oleate-L-FABP (Table 3.5). As compared with oleate, lysoPC, and palmitate, the perturbation data of EPA-L-FABP show notable differences. In the portal region, the most serious discrepancies involve residues with large perturbations, especially residues Val52, Tyr54, Gly55, and Lys57 (Figure 3.4). For most of the portal site residues, these differences indicate that the portal "lid" region of EPA-L-FABP is substantially less perturbed than with the other three ligands.

These trends could be explained by the fact that the diminished hydrophobic character of EPA or the conformational restrictions imposed by multiple degrees of unsaturation undercut the hydrophobic chain-chain interactions that are thought to stabilize binding of the second oleate ligand within the protein cavity. Such a trend fits the observed increase in K_d with increasing unsaturation in the series 18:0, 18:1, 18:2, and 18:3 (Richieri et al., 1994). Also, the larger size of the 20-carbon chain of EPA could prevent proper closure of the protein's portal upon binding the second ligand. These data contrast with previous findings from fluorescence studies using ADIFAB and DAUDA probes that claimed a L-FABP-EPA binding ratio of 1:2 (Norris et al., 2002). As for the internal binding region, differences in the magnitudes of average chemical shift perturbations between apo-L-FABP and holo-L-FABP for each of oleate, palmitate, and lysoPC (ranging from 89 to 93 Hz) as compared with EPA-L-FABP (62 Hz) suggest that the very long multiply unsaturated chain of EPA may adopt an orientation that differs from the remaining ligands. OLA 129 in the crystal structure of holo-oleate-L-FABP adopts a U-shaped conformation that is analogous to bound oleate in the crystal structure of human-B-FABP (Bellandiran et al., 2000). However, the crystal structure of the same protein with

docosahexaenioc acid (DHA), a 20-carbon fatty acid with six degrees of unsaturation, has placed this fatty acid in a helical conformation in the protein's internal binding site. These observations lead us to believe that EPA (20:5) adopts a conformation, which might be helical, that differs from the oleate, palmitate, and acyl chains of lysoPC in the internal binding site. As noted above, this twist in the FA conformation could be induced by extra degrees of unsaturation that exert constraints on the FA conformation within the binding cavity. The EPA conformation and binding sites could be verified by x-ray crystallography provided that crystals could be obtained for L-FABP with EPA.

c) Heme binding

L-FABP's affinity to heme has been reported to exceed that of oleate by tenfold (Styliani et al., 1985). In the current study, we use chemical shift perturbation of HSQC spectra to examine heme binding to L-FABP as compared with the native oleate ligand.

Almost no change was observed in the ^{15}N HSQC spectrum of apo-L-FABP after adding 1 eq of heme to an NMR sample buffer containing apo-L-FABP and 0.02% sodium azide (an inhibitor of bacterial growth). The average chemical shift perturbation of 1:1 heme L-FABP for 118 assigned residues was equal to 3.9 ± 7.0 Hz (Figure 3.11). This negligible perturbation indicates few if any interactions occurring between heme and apo-L-FABP in the presence of azide. Moreover, only small changes were observed for the HSQC spectra of the protein with heme and azide after reduction of ferriheme into ferroheme using dithionite. Chemical shift perturbation for the peaks in the spectrum of ferroheme-L-FABP versus apo-L-FABP was found to be 8.5 ±7.8 Hz for 100 assigned residues. These results indicate no significant interactions are occurring between L-FABP and heme in either of its oxidation states in the presence of azide.

However, using a buffer devoid of azide, the average chemical shift perturbation of apo-L-FABP versus 1:1 ferriheme-L-FABP for 65 assigned residues was equal to 48.2 ± 44.3 Hz (Figures 3.11, 3.12.b, and Table 3.6). The remaining residues could not be assigned due to the appearance of multiple peaks for particular amino acids and to significant decreases in signal intensity. Typically, each set of multiple peaks in the HSQC spectrum included one resonance with the same chemical shift as apo-L-FABP. A number of small peaks were observed to be in a region of the HSQC spectrum that is typical of random coil, indicating that the protein has undergone a degree of denaturation upon heme addition.

Residues with the largest perturbations were Glu16, Leu24, Leu28, Ile29, Gly32, Lys33, Leu65, Gly66, Glu68, Glu77, Lys90, and Ser124. Six of these residues displayed perturbations of less than 10 Hz upon oleate addition, signifying regions that are structurally stable and undergo minimal environmental changes upon binding of that ligand. However, in the presence of heme, these residues showed large perturbations, which could indicate localized protein unfolding. Additional small peaks in the random coil region were observed after adding a second equivalent of heme, indicating a larger degree of denaturation of the protein (Figure 3.12c).

To compare the binding of heme and oleate to L-FABP under similar conditions of protein concentration, temperature, and pH, we added oleate to a solution containing L-FABP with two equivalents of heme, finding peaks with partially recovered intensities. Moreover, all sets of doubled peaks merged into single peaks (Figure 3.12d). Chemical shift values for the resulting spectra were similar to those of holo (oleate)-L-FABP (perturbation = 73.1 ± 68.6 Hz vs. apo-L-FABP and 9.0 ± 4.5 Hz vs. holo (oleate)-L-FABP, respectively). After adding another 4 equivalents of oleate, the peaks increased further in intensity; however some of the small peaks

(corresponding to unfolded protein states) were still present (Figure 3.12e). The return of the chemical shifts essentially to their values in holo (oleate)-L-FABP argues against a scenario in which the heme and oleate occupy different binding sites. In a separate experiment, addition of two equivalents of heme to an NMR sample containing holo-oleate L-FABP with no azide present produced no changes in the HSQC spectra (data not shown). These results indicate that binding to oleate is favored over heme, in contrast to the report of Styliani et al. (1985).

This disparity in results could be attributed to different experimental conditions. The 50-μM protein concentrations used in the NMR experiments are comparable to the (0.82-3.55 μM) concentrations used for the fluorescence studies. Heme stock solutions in both NMR and fluorescence experiments were prepared by dissolving heme a solution containing 0.1 N NaOH and 50 mM phosphate (pH 7.4). However, our buffer solution contains 150 mM (physiological) NaCl, whereas the heme solution in the fluorescence experiments was devoid of NaCl. A difference in salt concentration could possibly alter the binding affinities for heme and oleate to L-FABP, but the two methodologies could be compared more rigorously by conducting the heme-LFABP NMR experiments in a buffer devoid of NaCl.

In order to investigate whether protoporphyrin, which is an iron-free form of heme, binds to apo-L-FABP, two equivalents were added in the absence of azide. Strong signs of protein denaturation were observed: loss of peak intensity, diminished chemical shift dispersion (Figure 3.13b), and sample precipitation. However, addition of two equivalents of oleate to the mixture did not restore the protein's native structure (Figure 3.13c). These results may indicate too large a degree of L-FABP unfolding with protoporphyrin to permit renaturation by oleate.

Taken together these results it seems that, in the absence of sodium azide, heme destabilize the L-FABP structure in aqueous solution through unfolding processes. However, in the presence of azide no interactions are observed. The effect of azide could be attributed to the high aqueous solubility of the heme-azide complex, which reduces its hydrophobic association with the protein.

Comparing the behavior of L-FABP with heme and protoporphyrin, it seems that L-FABP may be structurally unstable, exhibiting gradual unfolding in the presence of both ferriheme and protoporphyrin due to hydrophobic interactions. However, the unfolding induced by ferriheme-induced but not protoporphyrin is reversed upon oleate addition to form holo-oleate LFABP. This phenomenon suggests that protein suffers a larger degree of denaturation with protoporphyrin than with heme, possibly due to an increased hydrophobicity of protoporphyrin. Nevertheless, it is not clear what role the iron has in governing heme-L-FABP interactions.

d) Sterols

No changes were observed in the HSQC spectrum of apo-L-FABP upon titration with 10 eq of cholesterol. Both HSQC spectra look nearly identical, indicating very modest or no interaction between the protein and the water-insoluble sterol. The solution stays clear and there are no evident signs of denaturation, leading to the supposition that, unlike the L-FABP-heme mixture, the protein maintains its structural stability in the presence of cholesterol even though it apparently increases the sterol's solubility (Figure 3.14b). By contrast, small chemical shift perturbations and a few signs of denaturation are observed for residues of apo-L-FABP after adding two equivalents of the bile salt deoxycholate (Figure 3.14c). These preliminary data may

suggest a small environmental change due to weak binding of deoxycholate. Nevertheless, three-dimensional NMR experiments are needed in order to augment provisional assignments made by visual inspection.

e) Phospholipids

Comparison of HSQC spectra for apo-L-FABP, L-FABP with DMPC, and L-FABP with DHPC shows no chemical shift changes for the protein after adding 10 eq of DMPC. However, multiple small peaks and extensive line broadening may be attributed to protein unfolding by DMPC bilayer aggregates (Figure 3.15b). The spectrum of apo-L-FABP with 10 eq of DHPC exhibits chemical shift perturbations that average to 28.4 ± 19.8 Hz for 89 assigned residues (Figure 3.15c). However, a smaller degree of line broadening and peak splitting is observed for L-FABP with DHPC as compared to DMPC.

Spectral differences observed for L-FABP in the presence of DMPC and DHPC may be attributed to the difference in the aqueous solubility of both phospholipids. As evident from HSQC spectra, L-FABP doesn't seem to interact with the long acyl chain of DMPC. Chemical shift perturbations indicate possible interactions with short-chain DHPC. Comparing the DHPC-L-FABP data with caprylate-L-FABP and oleate-L-FABP (Figure 3.16), it is reasonable to invoke weak molecular interactions with these relatively small water-soluble lipids in a way that preserves the folding integrity of the protein but changes the chemical environment for some residues. However, no specific sites of interactions can be mapped from our current perturbation data.

2) Residual Dipolar Couplings for NMR Structural Refinement

Because of ambiguity in the NOE-derived structure of the helical region of apo-L-FABP (He et al., 2007), structural refinement was achieved by measuring residual dipolar couplings to obtain angular constraints for the NH bond vector orientations of the amino acid residues.

No peak splittings were observed in ^{2}H NMR of the HOD solvent for a protein-bicelle solution (Figure 3.17), indicating no alignment of the bicellar media. However, when $C_{12}E_5$/hexanol (0.96:1) or C_8E_5/octanol (0.87:1) were added to ^{15}N-apo-L-FABP, 21.3 and 19.7 Hz peak splittings were measured (Figure 3.18). These peak splittings in ^{2}H NMR indicate a gel-induced alignment of L-FABP in the magnetic field.

NH residual dipolar couplings were measured for 64 residues (of which 57 were included in the structure calculation) of the magnetically aligned apo-L-FABP in $C_{12}E_5$/hexanol by comparing chemical shift differences between the in-phase and anti-phase (IPAP) peaks of apo-L-FABP ^{15}N HSQC spectra in the presence and absence of the aligning gel (Table 3.7). For example, the chemical shift difference (in Hz) of the [(in-phase) - (anti-phase)] shift of the Asn 89 resonance for apo-L-FABP is subtracted from the [(in-phase) - (anti-phase)] shift of Asn 89 for apo-L-FABP in the gel. As shown by the equation and Figure 3.19,

$RDC_{Asn\ 89}$ = ((Asn_{89diff}(in gel)- Asn_{89diff}(no gel)) x (^{15}N frequency) = (116.72-114.93)- (116.76-115.27) x (60.8) = 11.1 Hz.

Some resonances could not be assigned for the remaining residues due to weak or overlapped signals, and thus RDCs could not be measured. However, the measured RDCs covered nearly all regions of the protein structure. Most importantly, 21 of the 57 residues for which RDCs were

measured are located in the structurally ambiguous portal region, which consists of helix I, helix II, and both C-D and E-F turns. In this region, RDCs were measured for residues Glu 16, Phe 18, Met 19, Ala 21, Met 22, Gly 23, Leu 24, Asp 27, Leu 28, Ile 29, Gln 30, Lys 31, Gly 32, Lys 33, Ile 35, Gly 37, Thr 51, Gly 55, Lys 57, Val 58, and Met 74 (Figure 3.20). Measured RDCs for the 64 measured residues ranged between (–15) and (+11) Hz, in accord with prior studies of proteins in these gel media (Ruckert and Otting, 2000).

The 3D structure of apo-L-FABP with dipolar couplings had RMSDs of 0.72 ± 0.25 and 1.24 ± 0.24 for the backbone and all heavy-atoms, respectively. Calculated RMSDs for apo-L-FABP without RDCs were 1.04 ± 0.34 and 1.54 ± 0.28 for the backbone and heavy-atoms, respectively (Figure 3.21; Table 3.8). It is evident from these data and from Figure 3.22 that introducing RDC angular constraints refined the tertiary structure of apo-L-FABP. Importantly, the unambiguous orientations determined for residues in the portal region (helix II and C-D turn) confirm a more open conformation for apo-L-FABP as compared with the holo protein. In addition to the portal region, structural refinement is observed for the B-C, D-F, G-H, and H-I turns. Comparing Ramachandran space results for L-FABP with and without RDCs, a percentage increase in the sterically allowed regions (8.0 to 9.9 %) and a decrease in the disallowed ones (1.2 to 0.2) for L-FABP shows that RDC-derived angular constraints produce a sterically better behaved structure.

Attempts to align holo (oleate)-L-FABP in $C_{12}E_5$/hexanol or C_8E_5/octanol were not successful. Two-dimensional HSQC experiments on L-FABP with ^{13}C-labeled oleate indicated possible expulsion of at least one oleate from the cavity upon adding the gel to the NMR sample containing holo (oleate)-L-FABP. This hypothesis is derived by comparing the spectra of the

holo protein with and without the gel, revealing the disappearance of the alpha and omega carbon signals for one of the two ^{13}C oleates in the middle panel (Figure 3.23).

Our structural refinement for apo-LFABP yields a more open conformation for the portal "lid" region through which apo-L-FABP might facilitate entry of larger size ligands and thus add to L-FABP ligand binding diversity.

3) Membrane mimetic media for NMR structural studies

Bicelles were used in our work for three purposes: and 1) dilute liquid crystalline bicelles (q = 3.0) to induce weak alignment for NMR structural refinement; 2) isotropically tumbling bicelles (q = 0.5) as mimetic media for lipid membranes used in the study of protein-membrane interactions; and 3) isotropic bicelles as test media for conducting high-resolution NMR structural studies on peripheral membrane proteins. The first use was described above in connection with RDC measurements, whereas the second and third uses are discussed below.

a) Quasielastic Light Scattering (QLS) size characterization

In order to validate our bicelle preparations against previously reported aggregates (Jing et al., 2005) and evaluate their suitability for high-resolution NMR studies, QLS measurements of hydrodynamic radius were made for DMPC/DHPC mixtures with q values equal to 0.2, 0.5, and 1.0 and lipid concentrations of 2.5% (w/w). Radius measurements for these bicelles agreed with a recently proposed model (Glover et al., 2001), yielding hydrodynamic radii of 3.2, and, 4.3 and 5.9 nm for q values of 0.2, 0.5, and 1.0, respectively (Figure 3.24).

b) L-FABP

Even though L-FABP is reported to show little or no interaction with lipid membranes during fatty acid transfer under near-physiological conditions (Storch et al., 1996), our research on membrane-FABP interactions began by examining L-FABP behavior in bicellar membrane-mimetic media because L-FABP is well-characterized structurally in our lab and since it has been proposed that such interactions can occur under conditions of low salt buffer and negative bicellar surface charge (Wilkinson et al., 1987). Moreover, the prior studies were not able to determine which regions on the protein's tertiary structure are associated with these membrane interactions. As noted above, small bicelles should be suitable for solution-state NMR studies since they tumble rapidly and isotropically in the magnetic field, minimizing peak broadening of associated protein molecules. Multiple titration experiments have been conducted in our lab in order to identify, both at the secondary structure and individual residue levels, protein regions that interact with bicelles. In order to favor the interactions between L-FABP and bicelle, titrations were carried out in a low ionic strength buffer with acidic bicelles composed of long-chain DMPC (neutral phospholipid), long-chain DMPG (acidic phospholipid), and DHPC (neutral phospholipid).

When 0.5 %, 1 %, and 2 % (0.2, 0.4, and 0.8 molar equivalents, respectively) of acidic bicelle (DMPG/DMPC/DHPC; q=0.5) were titrated into ^{15}N apo-L-FABP in a low ionic strength buffer (10 mM NaH_2PO_4, 50 mM NaCl) at 20 $^{\circ}$C, rather little or no broadening of the peaks was observed (Figure 3.25). The highest percentage corresponds to a bicelle-to-protein ratio of 0.8. HSQC spectra of apo-L-FABP and L-FABP with 0.8 molar equivalent of bicelle revealed a

chemical shift perturbation of 33.2 ± 31.8 Hz for 113 assigned residues (Figure 3.26). Residues with the largest chemical shift perturbation were located in dispersed regions on the protein's tertiary structure (Table 3.8 and Figure 3.27). This value represents an average for apo protein molecules and those species associated with the bicelle.

In order to examine the behavior of bicelles with the liganded form of the protein, holo-L-FABP (with 3 oleate equivalents) was titrated with 0.5 %, 1 %, 2 %, and 3 % (0.2, 0.4, 0.8, and 1.2 molar equivalents, respectively) of q=0.5 acidic bicelles at 20 $^{\circ}$C to assess concentration-dependent changes. Also, 1 % bicelle (0.4 equivalent) was added to a separate NMR sample containing holo-L-FABP (with 3 oleate equivalents), for which HSQC experiments were run after 1 day, 3 days, 1 week, and 4 weeks in order to monitor time-dependent changes in bicelle-L-FABP interactions.

Gradual shifts in the peak positions were observed during this period of time (Figure 3.28). HSQC titration data were compared with spectra of both apo-L-FABP and holo-(oleate) L-FABP. Chemical shift perturbations were calculated with respect to the HSQC spectra of holo-(oleate) L-FABP before and after 1 day and 1 week of adding 1 % bicelle. Also, perturbations were calculated for the holo-L-FABP with bicelle versus apo-L-FABP in order to check for possible release of oleates from L-FABP in the presence of an isotropic bicelle. Since no changes in chemical shift were observed after 1 week, the shifts were assumed to be unchanged 4 weeks after bicelle addition (Figure 3.28d and e).

Chemical shift perturbations of holo-L-FABP with 1 % bicelle after 1 day and 1 week versus holo-L-FABP were 26.1 ± 35.2 Hz and 46.9 ± 53.8 Hz, respectively, reflecting time-dependent alterations of the protein environments in the presence of bicelles. Residues with the largest

perturbation are listed in Table 3.10. Chemical shift perturbation of holo-L-FABP 1 week after bicelle addition versus apo-L-FABP was equal to 43.7 ± 35.2 Hz. By comparison, the chemical shift perturbation between apo-L-FABP and holo-(oleate) L-FABP was equal to 89.2 ± 93.2 Hz (Table 3.1). In addition, it was noticed that assigned peaks in the holo-L-FABP bicelle titration spectra shift toward values that correspond to their apo-L-FABP counterparts (Figures 3.28 and 3.29).

These trends suggest that the holo-protein undergoes time-dependent structural changes upon adding the bicelle, as revealed by the chemical shift changes of its residues. Small peak perturbations within 1-4 weeks suggest that these structural changes are modest yet observable by NMR within this period, before eventual protein aggregation and precipitation at ~ 4 weeks). Residues with the largest perturbations in Table 3.8 are located mainly in the portal region; 6 of these 7 residues are deduced from the crystal structure data to be located within of 5 Å of OLA 128. Also, measurements of the peak volumes for residues with large perturbations in each of the titration spectra (Figures 3.30 and 3.31) indicate a faster decrease in the peak volumes for residues in the portal region as compared with residues in the internal cavity, where the latter are proximal to OLA129 in the crystal structure. Hence, the shift toward the apo-protein spectra indicates that OLA 128 (but not OLA 129) may be released from the protein upon addition of the bicelle throughout the 4-week period before protein precipitation.

c) I-FABP

I-FABP is reported to exhibit stronger interactions than L-FABP with lipid membranes (Hsu et al., 1996), as expected in light of its collisional mechanism for fatty acid transfer. Initial NMR

experiments on L-FABP with acidic bicelles at low salt concentration prompted us to run experiments on I-FABP with varying concentrations of salt and acidic bicelles in order to compare protein-bicelle behavior in these media. NMR experiments were also run on I-FABP with neutral bicelles under both low and high salt conditions to assess the effect of bicelle surface charge on the chemical shift perturbation effects. This information is expected to provide us with insight on the residues and factors responsible for I-FABP interactions with lipid membranes.

Aliquots of 0.2 %, 0.5 %, 1 %, and 2 % (0.1, 0.2, 0.4, and 0.8 molar equivalents, respectively) of acidic (DMPG/DMPC/DHPC) and neutral (DMPC/DHPC) bicelles (q =0.5) were titrated into ^{15}N apo-L-FABP in media containing both low (10 mM NaH_2PO_4, 50 mM NaCl) and high (50 mM NaH_2PO_4, 100 mM NaCl) ionic strength buffers at 20 $^{\circ}$C (Figure 3.32). In all titrations (except I-FABP with acidic bicelle in low salt buffer), the following observations were noted from chemical shift perturbation data (Table 3.11) and from visual inspection of assigned 2D spectra supplemented by 3D experiments). 1) minimal peak broadening was observed throughout the titrations. More than 90 % of the peaks remained as singlets, though a small number of peaks appeared in the random coil region of the HSQC spectra, suggesting protein unfolding or fragmentation. 2) After each step of the titration (~1-6 days apart), peaks exhibited small (<10 Hz) chemical shift changes. 3) Residues with the largest perturbation are located in diverse regions of the protein: Gly31 and Ala32 (helix II), Lys37 (beta strand B (βB)), Arg56, Asn57, and Ile58 (βC-βD turn), Glu63 (βD), Phe68 and Ser71 (βE), Glu77 (βE-βF turn), Thr81 (βF), Phe93 (βG), Leu102, Ala104, Val105, and Arg106 (βG-βH turn), and Leu113 (βJ) (Figures 3.33 and 3.34). However, of these residues, larger perturbations were measured for

amino acids located in helix II, βC-βD, and βD-βE turn. Comparing these bicelle perturbation data for I-FABP with those of L-FABP (Figures 3.26-7 and 3.33-4), more pervasive perturbations for L-FABP but a surprisingly similar overall pattern are observed in light of the contrasting fatty acid transfer mechanisms for the two proteins. However, the similarity may reflect our adjustment of experimental conditions (decrease in ionic strength, introduction of negative surface charge) to promote L-FABP-membrane interactions.

The minimal peak broadening observed in I-FABP bicelle titration spectra is a surprise considering the estimated 40-60 kD size of these bicellar aggregates and their likely enhanced size when the protein is present. Measuring NMR T_2 values for protein signals with bicelles of varying q values could help us determine the nature of the protein-bicelle interactions. If, for example, an increase in q values (increase in bicellar size) leads to a corresponding decrease in T_2 values, possible FABP-bicelle interactions might be inferred in a slowly tumbling complex. Also, these NMR relaxation measurements could augment size measurements of the aggregates by QLS or other physical methods.

In the case of I-FABP with acidic bicelles in low salt buffer, extensive peak broadening was observed upon adding 0.5 % of bicelle and accentuated at subsequent titration steps (Figure 3.35). These broadenings likely result from long tumbling times for particles in the NMR sample, possibly due to bicelle-induced protein aggregation. By the fourth titration point (2 % bicelle) the peaks had lost > 97 % of their intensity. To examine the time-dependent behavior of I-FABP at constant bicelle concentration, 0.5 % bicelle was added to I-FABP and its HSQC spectra were monitored over time. Similar patterns of peak broadening were observed as in the bicelle concentration series, indicating that this broadening increases with time (Figure 3.36).

DHPC was added to the NMR sample of I-FABP with 2 % bicelle to attempt the reversal of this bicelle-induced broadening by adding phospholipid monomers and changing q to a value of 0.2. Indeed, peak sharpening was observed and peaks regained > 90 % of their initial intensity (Figure 3.37). This observation suggests that protein unfolding and/or aggregation events associated with the DMPC-DHPC bicelle caused a substantial increase in particle tumbling time, possibly from interactions with the DMPC. Addition of DHPC was able to reverse this aggregation, possibly by reducing the bilayer region of the bicelle or forming a smaller lipid micelle.

The above observations also raise questions about the morphology of the bicelles under our experimental conditions and about which lipid species is (are) interacting with the protein. The bilayer planar surface and small size of isotropic bicelles are thought to render them suitable for solution-state NMR studies of protein-membrane interactions. However, it would be useful to conduct a careful assessment of the curvature and planarity of the protein-bicelle assemblies using, for example, dynamic light scattering techniques and electron microscopy visualization (Glover et al., 2001). The structural integrity of the protein-containing bicelles could also be examined with ^{31}P NMR, which should exhibit resolved peaks for bilayer and rim locations within the bicelle assembly if the particle size is not prohibitively large.

The possibility that the FABPs are binding to lipid micelles is important in light of differing binding affinities of proteins to micelles as compared to bicelles and the structural strains that micelle curvature might exert on protein conformation (Poget et al., 2007). The presence of lipid monomers or micelles might be detected through comparison with reference ^{31}P chemical shift data on these phospholipids. The hypothesis that the FABP chemical shift

perturbations in DHPC-DMPC mixtures result from binding to the DHPC monomers or micelles could be tested by independently titatrating the protein with DHPC both below and above critical micelle concentration (~1.8 mM without protein present). If that occurred, the bicelle might become depleted of DHPC, increasing its size and promoting precipitation or aggregation with protein molecules.

Since protein-ligand chemical shift perturbations plots were available for L-FABP with ligand (e.g., oleate), these were compared against L-FABP-bicelle plots in order to locate regions with high perturbations on L-FABP's tertiary structure and relate the two sets of data. Figure 3.38 shows residues with large perturbation located in analogous regions on the L-FABP structure, lending support to the theory of protein binding to lipid monomers. However, further testing as described above is needed in order to confirm the identity of the FABP-binding species.

Repeated titration experiments using freshly made phospholipid solution yielded a more stable protein-lipid system containing I-FABP with 2% acidic bicelle in low salt buffer and lasting more than two months at 4 $^{\circ}$C. Previous studies conducted on bicelles in our lab (Glover et al., 2001) have shown that the $DHPC_{monomer}$ - $DHPC_{bicelle}$ equilibrium shifts towards $DHPC_{monomer}$ at low lipid concentrations, leaving a fair amount of water-insoluble DMPC in solution. As shown previously in this dissertation, DMPC induced a larger degree of L-FABP unfolding than DHPC (Figure 3.15). Noting that DHPC undergoes facile hydrolysis in aqueous solutions at neutral pH (Aussenac et al., 2005), it may be proposed that extended FABP stability with freshly made DHPC occurs because of the presence of smaller amounts of hydrolyzed DHPC. An increased concentration of hydrolyzed DHPC might lead in turn to bicelle

disintegration, leaving water-insoluble DMPC in solution where it may promote protein unfolding and aggregation events. Another limitation of these DMPC/DHPC bicelles of fast hyrolysis of their monomers, leading to bicelle disintegration, can be circumvented by using above mentioned ester-linked phospholipids monomers. In fact, current bicelle samples made from these monomers have exhibited long-term stability (over 3 month) in protein NMR samples.

With a stable protein-bicelle system in hand, it was possible to conduct three-dimensional NMR experiments to establish site-specific resonance assignments required for determining the three-dimensional structure of I-FABP in a membrane-mimetic environment. Complete sequence-specific backbone assignments of $^{15}N/^{13}C$-apo-I-FABP with 0.4 eq of neutral bicelle were obtained (Table 3.12). These assignments were made by correlating C^{α} and C^{β} nuclei for i and i-1 (where i is an amino acid and i-1 is an amino acid that precedes it) in HNCACB and CBCACONH experiments and C^{CO} correlations of i and i-1 residues in HNCO and HNCACO experiments. Side-chain assignments will also be obtained by sequence-specific correlations from experiments that include: HCCH-TOCSY, H(CCO)NH-TOCSY and H(CO)NH-TOCSY (Figure 1.17).

Table 3.1: Chemical Shift Perturbation Analysis of L-FABP with Structurally Related Ligands

Holo-L-FABP	Average perturbation ± standard deviation (Hz) vs apo-LFABP	Residues with largest perturbation [1]
apo-L-FABP/ LysoPC	91.0 ± 95.1	**Gly32, Gly37, Ser39, Thr51, Tyr54, Ser56, Lys57, His60, Glu72, Thr75, Gly106, Ile109**
apo-L-FABP/ palmitate	93.3 ± 98.7	**Gly32,** Asp34**, Gly37, Ser39, Thr51, Tyr54, Ser56, Lys57, His60, Glu72, Thr75, Gly106, Ile109**
apo-L-FABP/ oleate	89.2 ± 93.2	**Gly32, Gly37, Ser39, Gly106, Thr51, Tyr54, Ser56, Lys57, His60, Glu72, Thr75,** Val92**, Ile109**

[1]Residues exhibiting changes in chemical shift > mean perturbation + 1 standard deviation. Residues with large perturbations for all three ligands are noted in boldface. For ^{15}N resonating at 60 MHz, 1 ppm = 60 Hz.

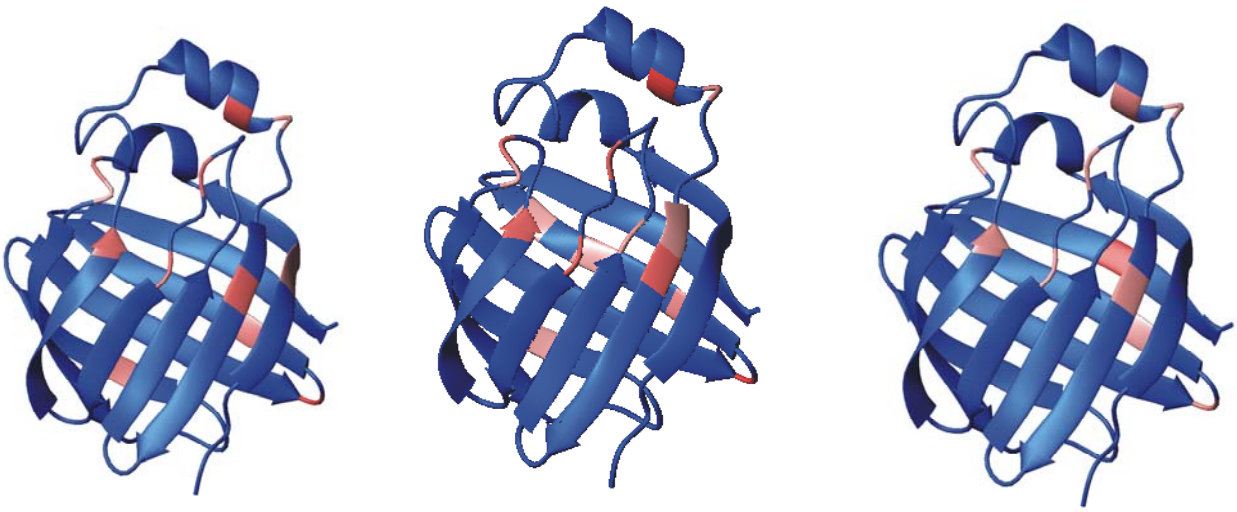

Figure 3.1: Three-dimensional representations of ^{15}N-holo-L-FABP with a) oleate, b) palmitate, and c) lysphosphatidylcholine. Regions highlighted in red represent protein residues with the largest chemical shift perturbations as compared with apo-L-FABP.

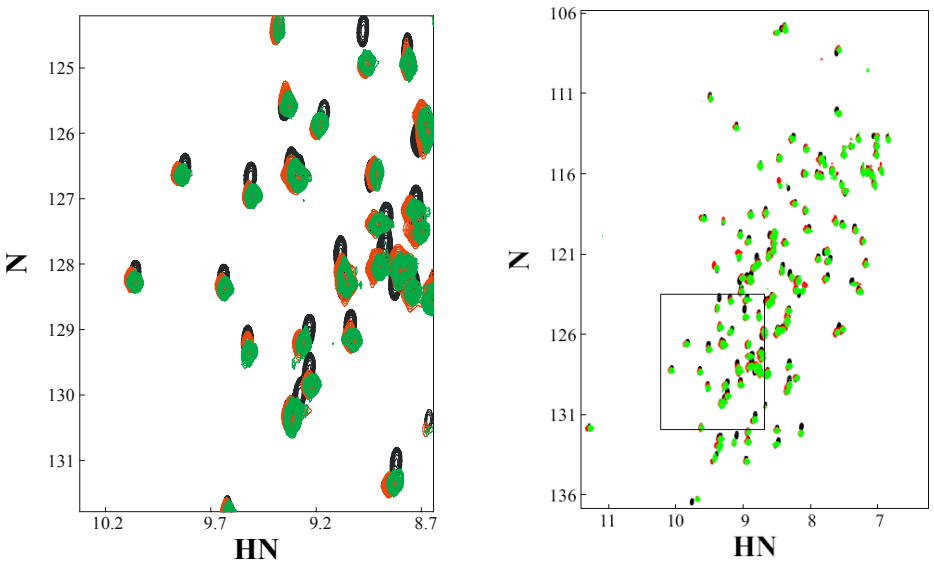

Figure 3.2: An overlay of two-dimensional ^{15}N-HSQC spectra of apo-L-FABP with two equivalents of each of oleic acid (black), palmitic acid (red), and lysoPC (green). Measured chemical shift perturbations for lysoPC-L-FABP vs palmitate-L-FABP, lysoPC-L-FABP vs oleate-L-FABP, and oleate-L-FABP vs palmitate-L-FABP are 9.8 ± 7.1 Hz, 10.9 ± 9.3 Hz, and 13.1 ± 11.7 Hz, respectively. The highlighted portion of the amide NH region is expanded in the lefthand contour plot.

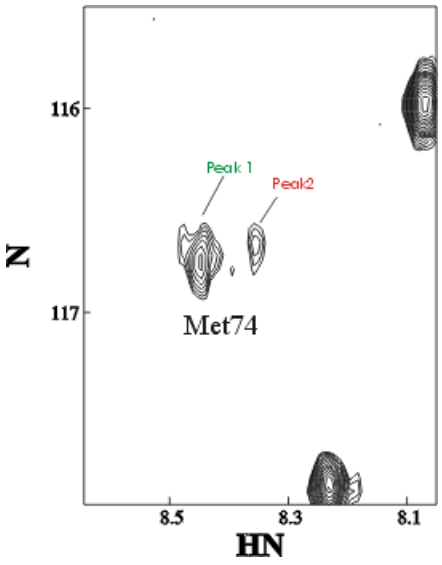

Figure 3.3: Region of an HSQC spectrum of L-FABP with two equivalents of lysoPC, showing two resonance signals for Met 74, coincident with palmitoyl-L-FABP (peak 1) and oleoyl-L-FABP (peak 2).

Table 3.2: Chain Length Distribution For Lysophosphatidylcholine bound to L-FABP

Residue	Pal-lysoPC peak vol a.u	Stearoyl-lysoPC peak vol, a.u	% Stearoyl-lysoPC
Val92	**176.2**	**36.9**	**17.3**
Gln8	**269.5**	**41.4**	**13.3**
Met74	**198.8**	**35.7**	**17.9**
average	**215.6**	**38.1**	**16.1**

Table 3.3: Chemical shift perturbation for L-FABP with long-chain fatty acids [1]

Internal site	δ LysoPC : δ Oleate	δ LysoPC : δ Palmitate	Portal site	δ LysoPC : δ Oleate	δ LysoPC : δ Palmitate
Ser39	**1.01**	**0.98**	**Leu28**	**0.60**	**0.87**
Ile41	**0.99**	**0.90**	**Lys31**	**1.28**	**1.36**
Phe63	**0.92**	**0.95**	**Gly32**	**1.11**	**0.96**
Glu72	**1.03**	**0.95**	**Ile35**	**0.79**	**1.13**
Thr73	**0.95**	**1.11**	**Val52**	**1.19**	**0.98**
Thr93	**0.29**	**1.08**	**Tyr54**	**1.08**	**0.92**
Thr102	**1.23**	**0.95**	**Gly55**	**0.97**	**1.06**
Arg122	**1.44**	**1.11**	**Lys57**	**1.00**	**0.94**
Ser124	**0.92**	**1.00**	**Leu113**	**1.13**	**0.97**
			Arg122	**1.44**	**1.11**

[1] Residues within 5 Å of an oleate chain in the X-ray crystal structure. Arg 122 is within 5 Å of oleate chains at both sites.

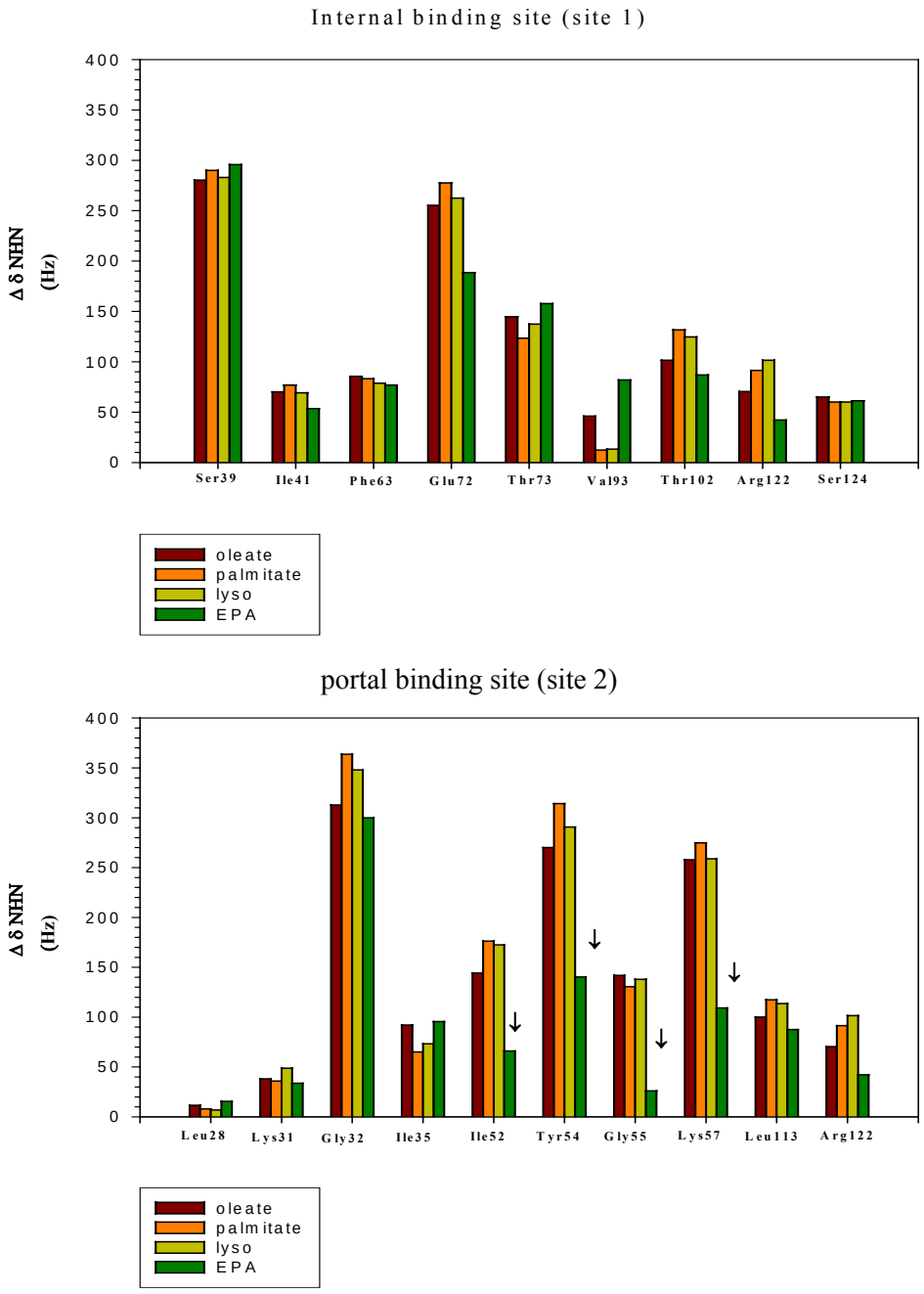

Figure 3.4: Chemical shift perturbation bar plots of ^{15}N apo-L-FABP titrated with 2 equivalents of oleate, palmitate, lysoPC, and EPA at internal and portal binding sites. The selected residues lie within 5 Å of an oleate chain, as judged from the x-ray crystal structure (Thompson et al., 1997). Residues Ile52, Tyr54, Gly55, and Lys57 of EPA are marked by arrows to indicate large perturbation differences with the remaining ligands. Arg122 is located proximally to oleates at both sites.

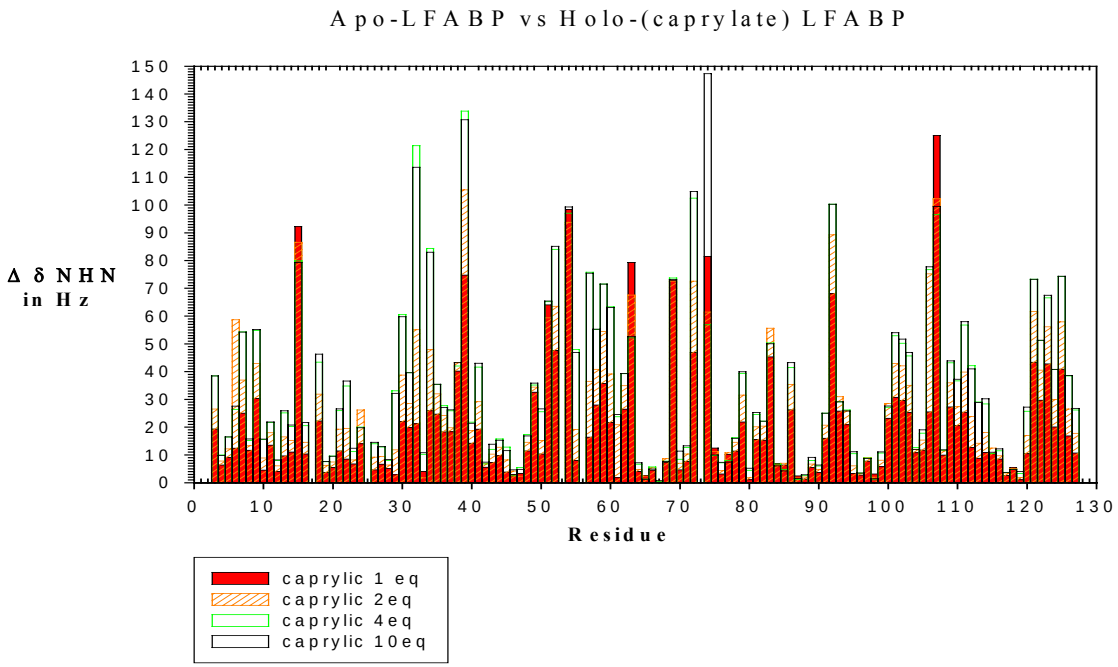

Figure 3.5: Chemical shift perturbation bar plot of ^{15}N apo-L-FABP titrated with 1, 2, 4, and 10 equivalents of caprylic acid with average perturbations of 19.8 ± 22.0, 26.2 ± 23.6, 32.3 ± 28.1, and 33.4 ± 29.8 Hz, respectively.

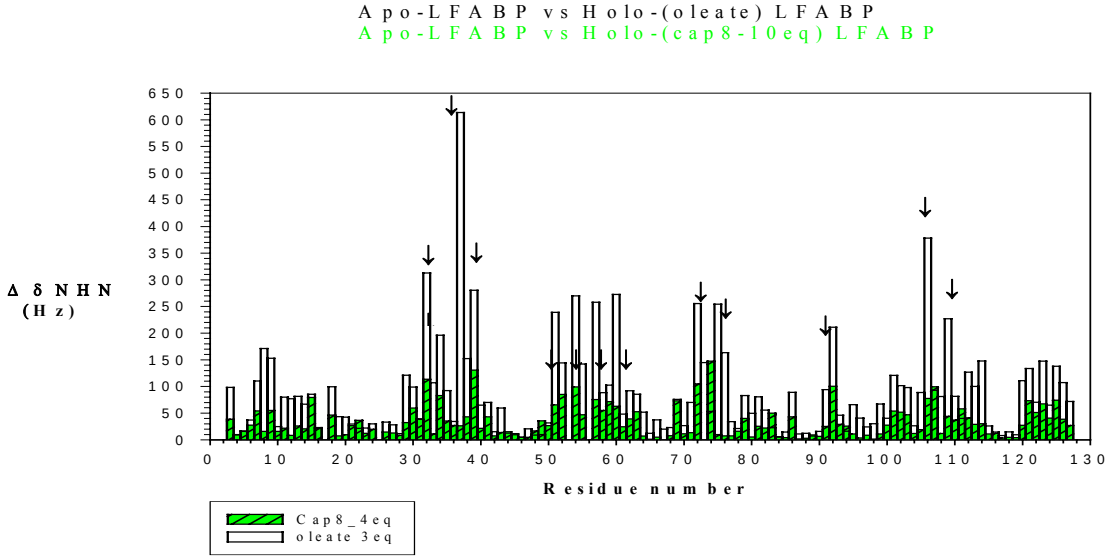

Figure 3.6: Chemical shift perturbation bar plot of ^{15}N apo-L-FABP with 4 equivalents of caprylic acid (green bars) and 3 equivalents of oleic acid (white bars). Measured perturbations are 33.4 ± 29.8 and 89.2 ± 93.2 Hz, for L-FABP with caprylic and oleic acid, respectively. Residues with large perturbations for both ligands are marked by arrows.

Table 3.4: Chemical shift perturbation of ^{15}N L-FABP with Shortened Fatty Acid Chain Length

apo-L-FABP with 4 equivalents of caprylic acid		apo-L-FABP with 3 equivalents of oleic acid	
Residue	**Perturbation (Hz)**	**Residue**	**Perturbation (Hz)**
Phe 15	**79.8**	***Gly 32**	**312.8**
***Gly 32**	**121.3**	***Asp 34**	**196.2**
***Asp 34**	**84.3**	**Gly37**	**613.8**
***Ser 39** [1]	**133.8**	***Ser 39**	**280.2**
***Thr 51**	**65.2**	***Thr 51**	**278.8**
Ile 52	**84.0**	***Tyr 54**	**343.9**
***Tyr 54**	**97.1**	**Ser 56**	**338.7**
***Lys 57**	**75.7**	***Lys 57**	**257.9**
Ile 59	**71.5**	***His 60**	**272.7**
***His 60**	**62.2**	***Glu 72**	**255.4**
Cys 69	**73.7**	**Thr 75**	**255.4**
***Glu 72**	**102.4**	***Val 92**	**210.9**
Met 74	**56.9**	***Gly106**	**378.2**
*** Val 92**	**100.3**	**Ile 109**	**226.8**
***Gly 106**	**76.7**		
Asp 107	**96.5**		
Lys 121	**73.2**		
Lys 125	**74.6**		
Mean value For all residues	**27.1**	**Mean value For all residues**	**89.2**

[1]Residues with large perturbations (1 standard deviation beyond the mean) are shown with (*).

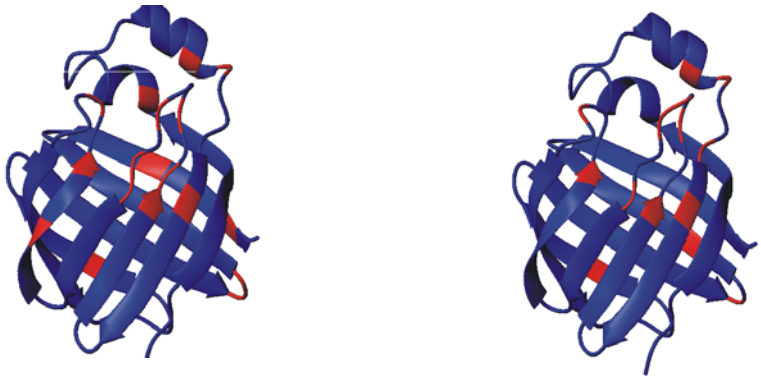

A B

Figure 3.7: Three-dimensional representation of holo-(oleate)-L-FABP from the crystal structure (Thompson et al., 1997). Regions highlighted in red show residues with chemical shift perturbation > mean perturbation + 1 standard deviation with A) 4 equivalents of caprylic acid and B) 3 equivalents of oleic acid added to apo-L-FABP, respectively.

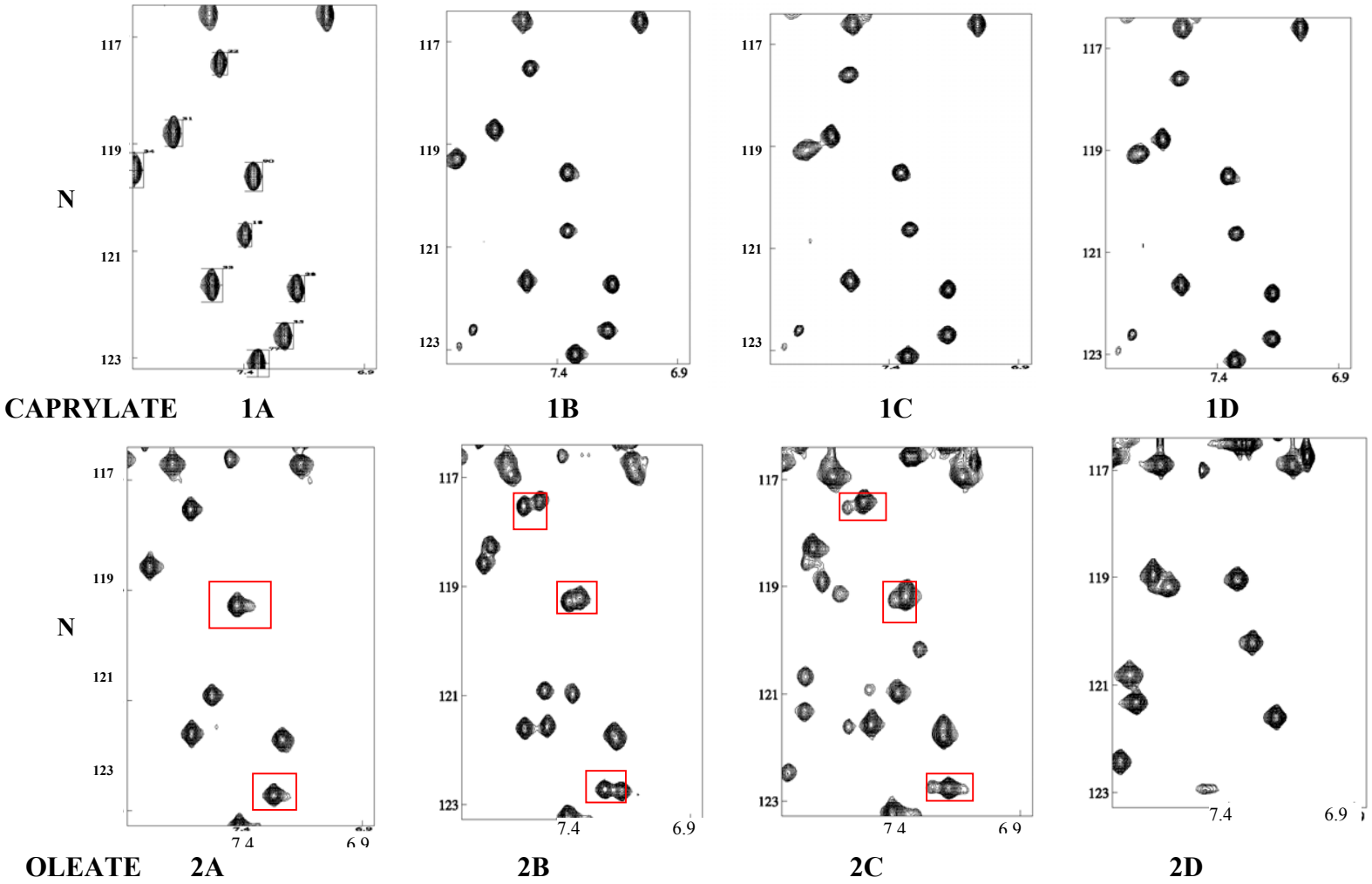

Figure 3.8: Regions of the HSQC spectra of ^{15}N apo-LFABP titrated with 1) caprylic acid and 2) oleic acid. Protein is titrated with 0, 1, 4, and 10 equivalents of caprylic acid in graphs 1A, 1B, 1C, and 1D, respectively. In 2, protein is titrated with 0, 0.4, 0.8, and 3.0 equivalents with oleic acid, respectively.

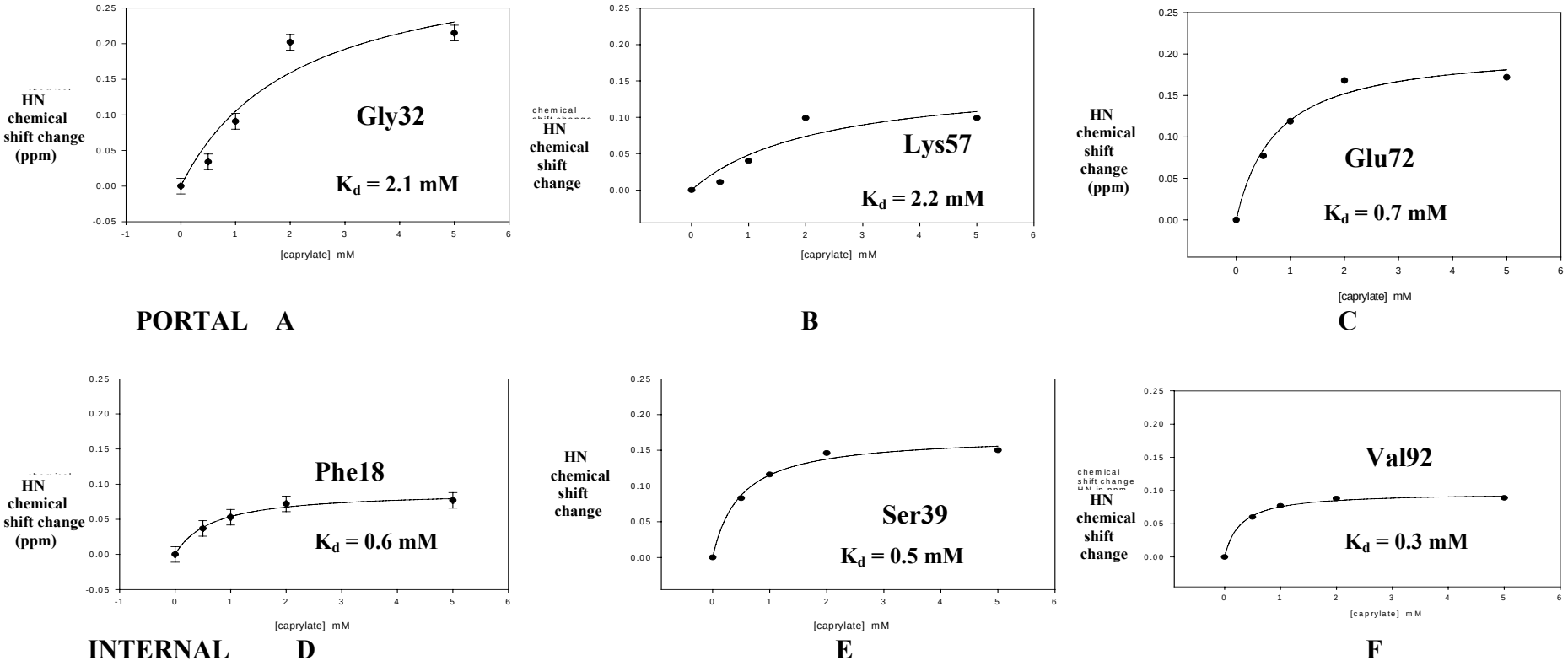

Figure 3.9: Plots of $\Delta\delta_{HN}$ for residues of apo-L-FABP upon titration with 1, 2, 4, and 8 molar equivalents of caprylic acid. Plots (a-c) are for residues at the portal binding site (Gly32, Lys57, and Glu72), whereas plots (d-f) denote those at the internal binding site (Phe18, Ser39, and Val92). Additional residues monitored for determination of K_d were Asp34, Thr51, and Ile52 (portal site) and Cys69, Asp107, and Lys121 (internal site). Error bars reflect limitations of digital resolution on determinations of peak position and likely impact of pipetting errors on caprylate concentrations. Error limits are estimated 0.013 ppm and 0.011 mM for chemical shift change and caprylate concentration, respectively, producing uncertainties n the K_d values of 1.3-10.0 %.

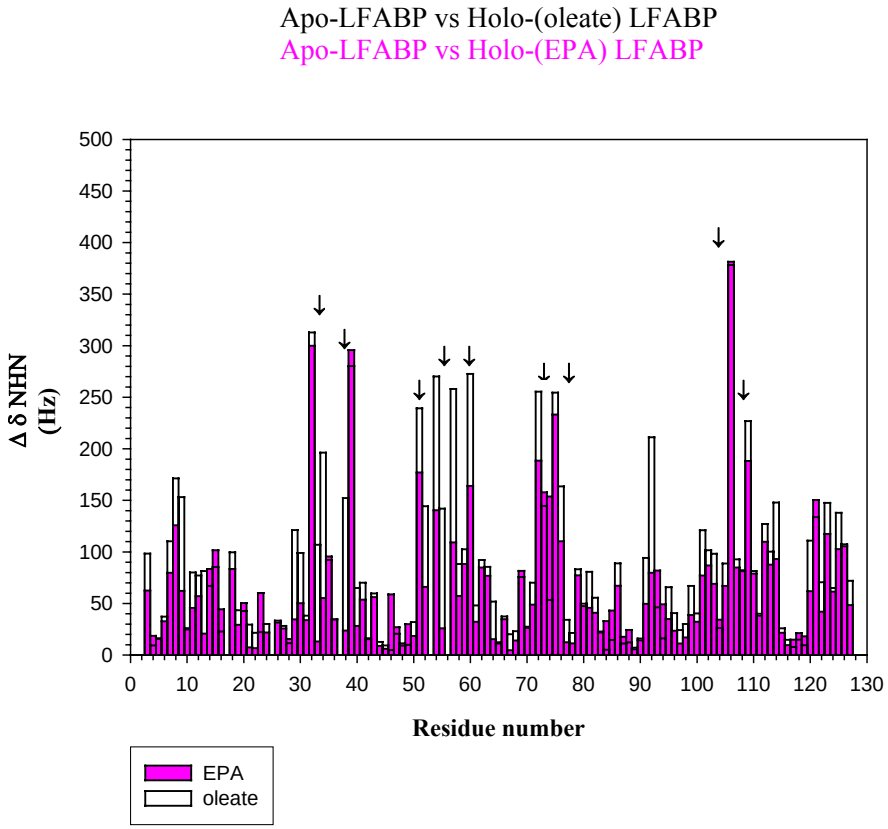

Figure 3.10: Chemical shift perturbation bar plot of ^{15}N apo-L-FABP with 5 equivalents of EPA (purple bars) and 3 equivalents of oleic acid (white bars). Observed average perturbations are 62.8 ± 61.8 Hz and 89.2 ± 93.2 Hz, for EPA and oleic acids, respectively. Residues with large perturbations for both ligands are marked by arrows.

Table 3.5: Chemical Shift Perturbation of L-FABP for FAs with Augmented Chain Length

apo-L-FABP with 5 eq EPA		apo-L-FABP with 3 eq OLA	
Residue	**Perturbation (Hz)[1]**	**Residue**	**Perturbation (Hz) [1]**
Gln 8	**125.8**	***Gly 32**	**312.8**
***Gly 32**	**299.9**	**Asp 34**	**196.2**
Ile35	**95.5**	**Ile35**	**92.1**
***Ser 39**	**295.7**	**Gly37**	**613.8**
***Thr 51**	**176.9**	***Ser 39**	**280.2**
Val52	**66.1**	***Thr 51**	**278.8**
***Tyr 54**	**140.3**	**Val52**	**144.2**
Gly55	**25.9**	**Tyr54**	**270.0**
Lys57	**109.1**	**Gly55**	**141.9**
***His 60**	**163.9**	**Ser 56**	**338.7**
***Glu 72**	**188.5**	**Lys 57**	**257.9**
Thr 73	**157.7**	***His 60**	**272.7**
Met 74	**153.7**	***Glu 72**	**255.4**
***Thr 75**	**233.3**	***Thr 75**	**255.4**
***Gly106**	**381.4**	**Val 92**	**210.9**
***Ile 109**	**188.3**	***Gly106**	**378.2**
Lys 121	**150.4**	***Ile 109**	**226.8**

[1] Measured perturbations for all residues are 62.8 ± 61.8 Hz and 89.2 ± 93.2 Hz, for EPA and oleic acids respectively. The 8 residues marked with (*) display large chemical shift perturbations upon addition of either fatty acid.

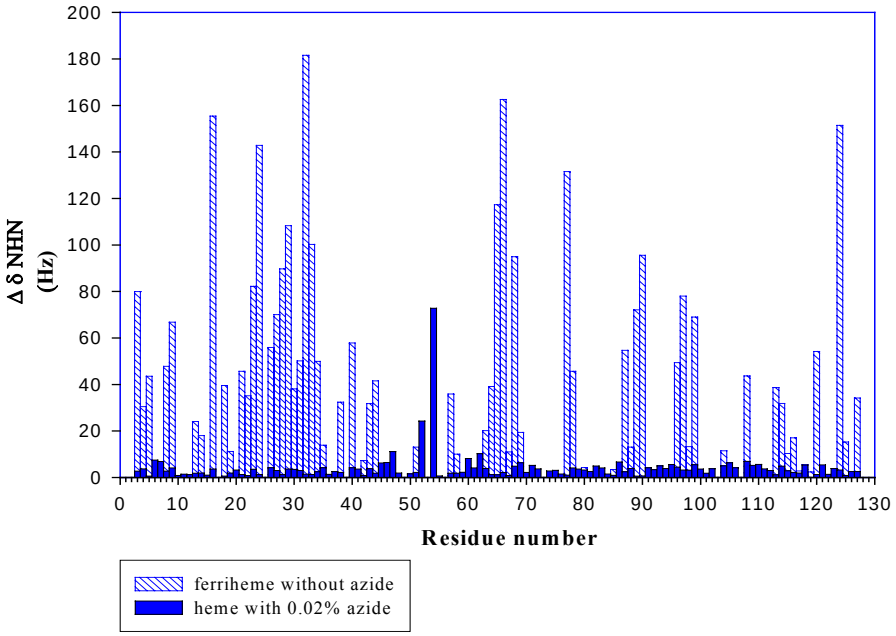

Figure 3.11: Chemical shift perturbation bar plot of ^{15}N apo-LFABP versus ^{15}N apo-LFABP with one equivalent of ferric heme. Measured chemical shift perturbations are 3.9± 7.0 Hz and 48.2 ± 44.3 Hz in the presence and absence of azide, respectively.

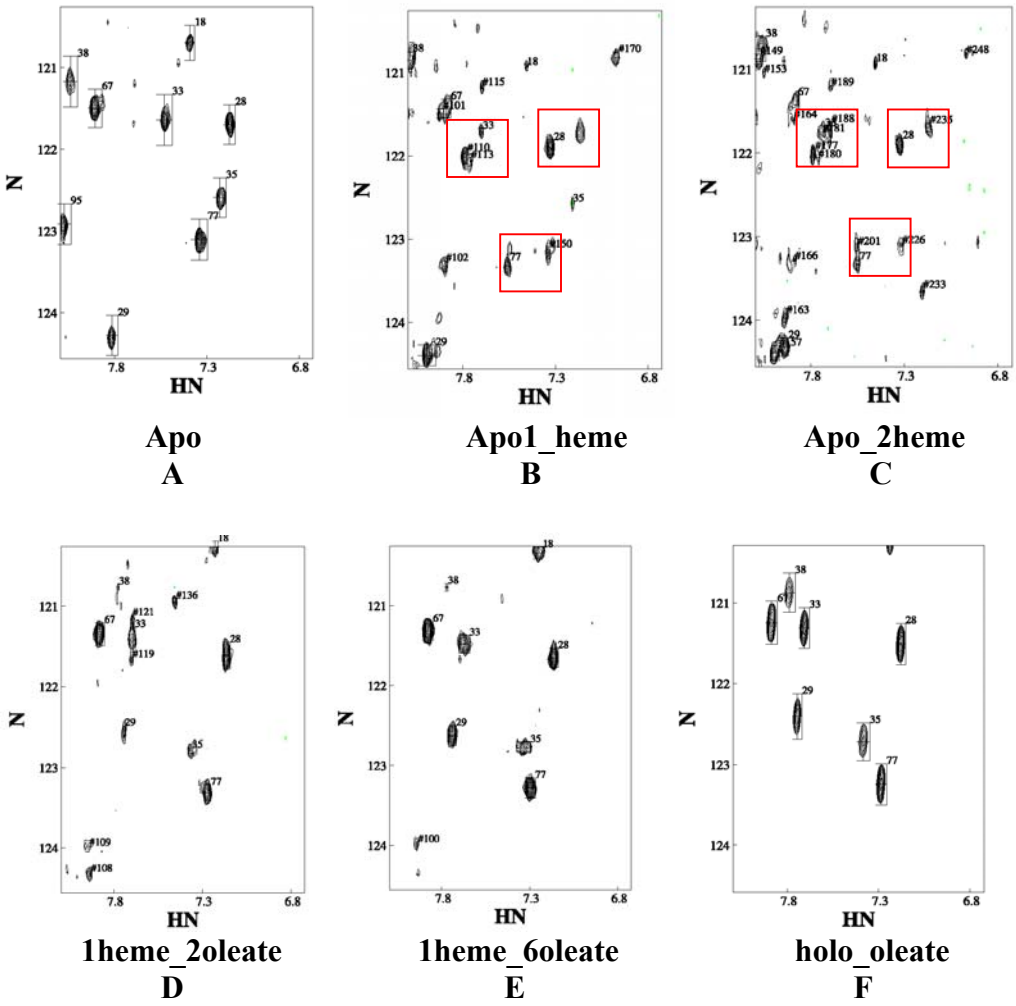

Figure 3.12: ^{15}N HSQC contour plots in the absence of azide of a) ^{15}N apo-L-FABP with b) one and c) two molar equivalents of heme d) two and e) six equivalents of oleate. Measured chemical shift perturbations for the spectra of ^{15}N apo-L-FABP with two equivalents of heme and ^{15}N holo-oleate L-FABP's are 73.1 ± 68.6 Hz and 9.0 ± 4.5 Hz, respectively, both measured with respect to ^{15}N apo-L-FABP. Doubled peaks are highlighted in boxes.

Table 3.6: Chemical shift perturbations of ^{15}N apo-L-FABP with ferriheme

Residue	Perturbation (Hz)[1]
Gly 32	**181.6**
***Gly 66**	**162.6**
***Glu 16**	**155.4**
***Ser 124**	**151.4**
***Leu 24**	**142.3**
Glu 77	**131.5**
Leu 65	**117.3**
Ile 29	**108.2**
Lys 33	**100.3**
***Lys 90**	**95.5**
***Glu 68**	**95.0**
Leu 28	**89.7**
average	**48.2**

[1] The tabulated residues show perturbations greater than 1 standard deviation above the mean of 48.2 ± 44.3 Hz after addition of 1 equivalent in the presence of azide. The six residues highlighted in red show less than 10 Hz chemical shift perturbation between apo-L-FABP and oleate-L-FABP, reflecting regions of structural stability.

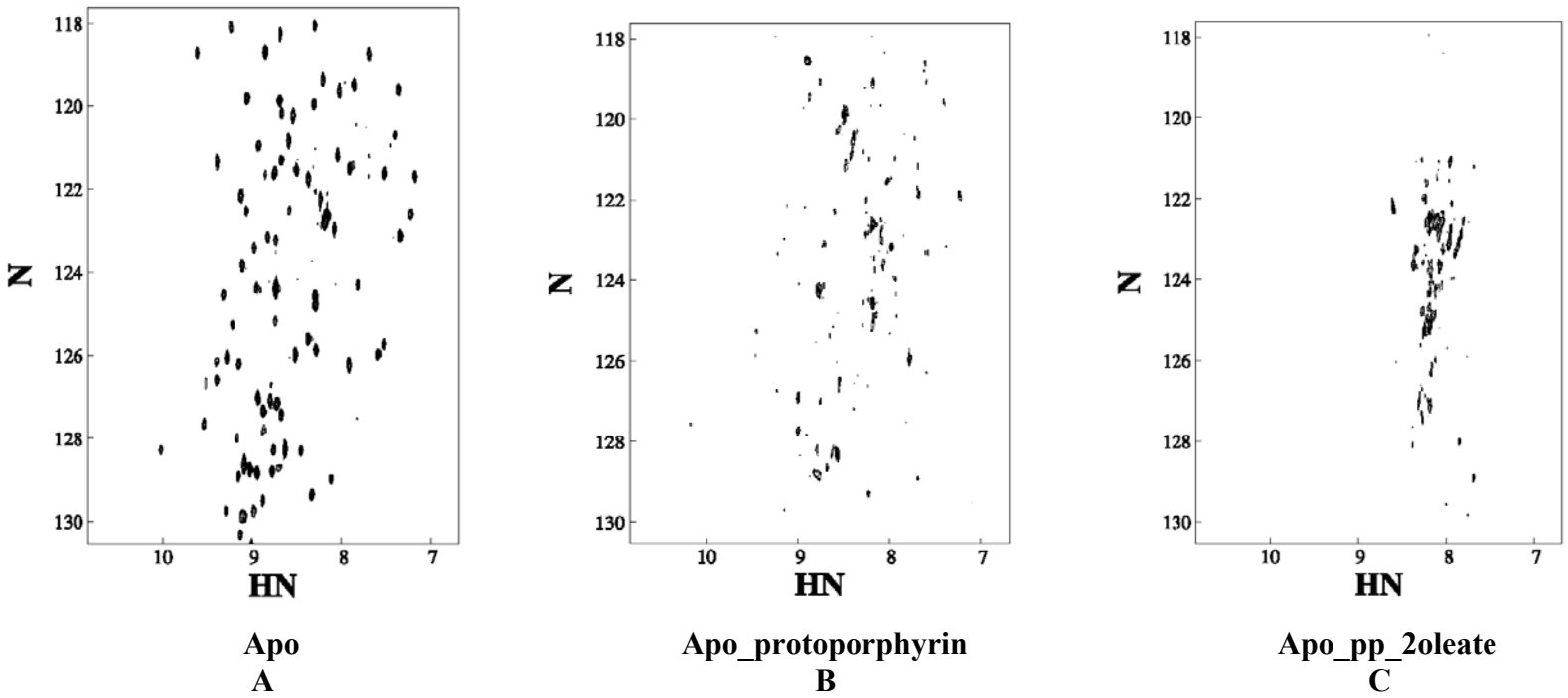

Figure 3.13: HSQC spectra of a) ^{15}N apo-L-FABP with b) two equivalents of protoporphyrin, and c) two equivalents of protoporphyrin followed by two equivalents of oleate. No azide was present.

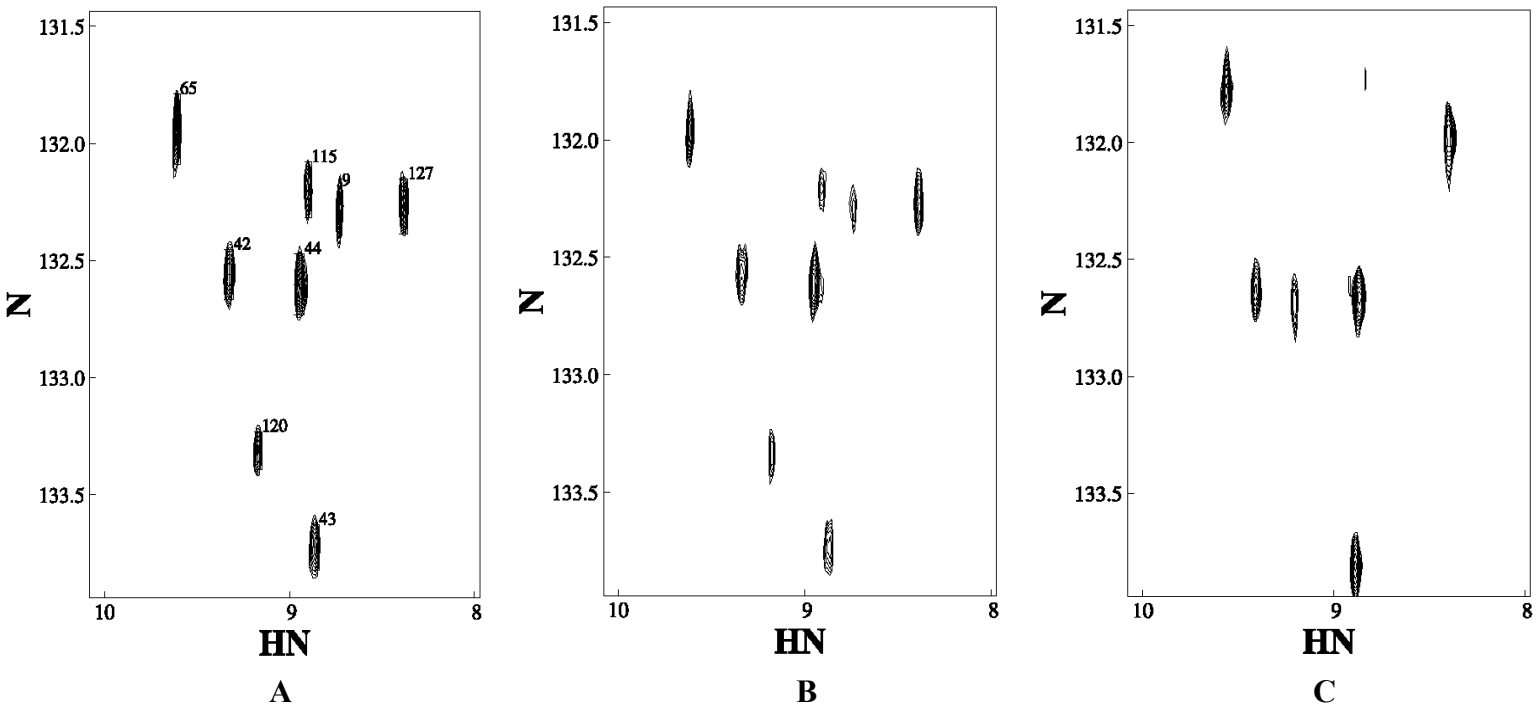

Figure 3.14: ^{15}N HSQC spectra of a) ^{15}N apo-L-FABP's with b) 10 equivalents of cholesterol, and c) two equivalents of deoxycholate.

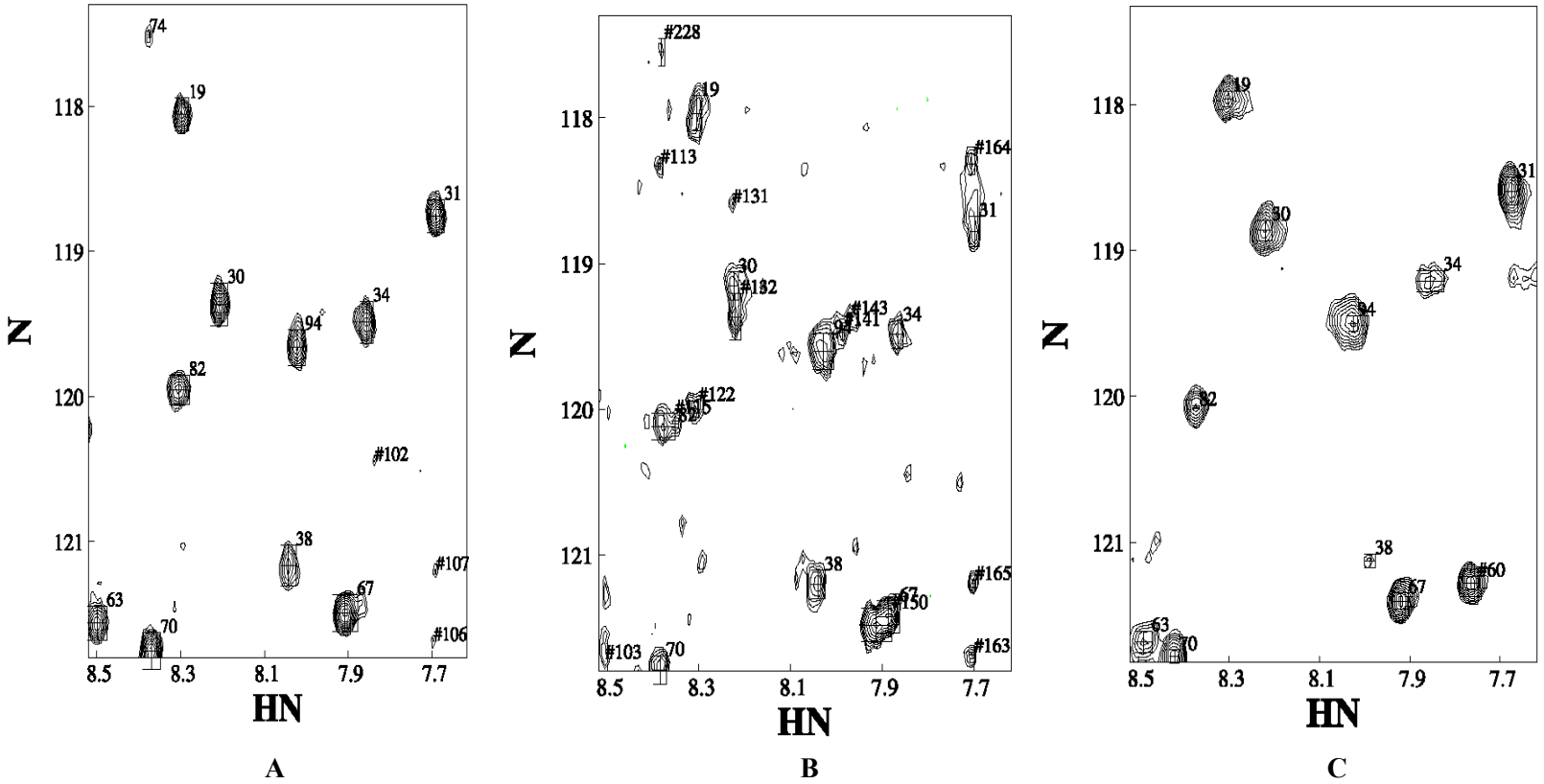

Figure 3.15: HSQC spectra of a)^{15}N apo-L-FABP with 10 equivalents each of b) DMPC and c) DHPC.

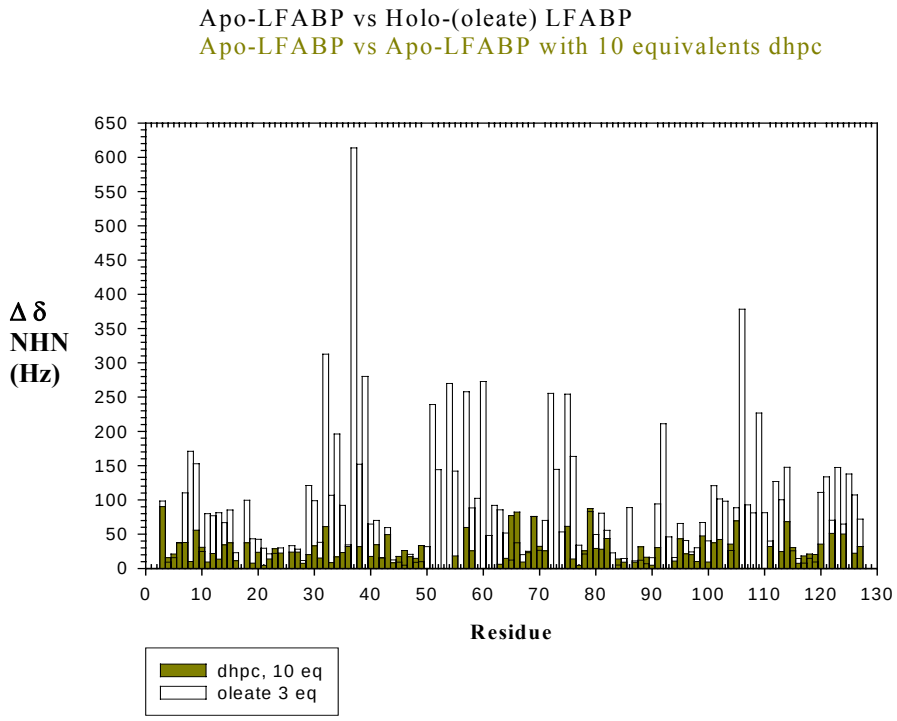

Figure 3.16: Chemical shift perturbation bar plot of ^{15}N apo-L-FABP with ten equivalents of dihexanoylphosphatidylcholine (DHPC) (green bars) and three equivalents of oleic acid (white bars). Measured perturbations are 28.4± 19.8 Hz and 89.2 ± 93.2 Hz, for DHPC and oleic acid, respectively.

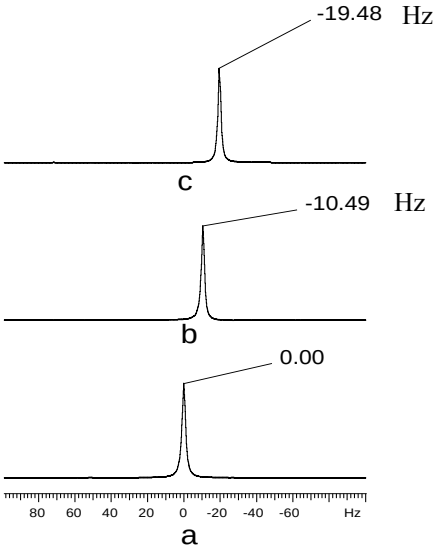

Figure 3.17: 1D ^{2}H NMR spectra of the HOD solvent in a solution of ^{15}N-apo-L-FABP with DMPC/DHPC bicelle (q = 3, 5 % (w/w)): 10°C, b) 20 °C, and c) 30 °C.

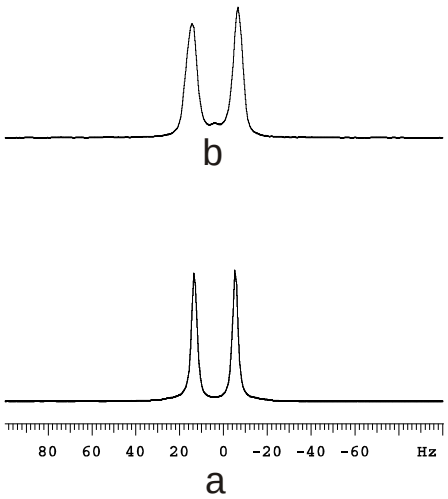

Figure 3.18: 1D ^{2}H NMR spectra of HOD in ^{15}N-apo-L-FABP with 5 % (w/w) gel media: a) $C_{12}E_5$/hexanol b) C_8E_5/octanol.

Table 3.7: NH Residual Dipolar Couplings for Apo-L-FABP

#	Residue	RDC (Hz)[1]	#	Residue	RDC (Hz)[1]
1	Ser 4	- 16.5	43	Glu 86	6.93
2	Gly 5	7.23	44	Gly 87	0.31
3	Gln 8	6.26	45	Asn 89	11.2
4	Val 9	9.67	46	Lys 90	- 11.0
5	Gln 10	0.42	47	Gly 97	- 15.7
6	Ser 11	- 14.0	48	Lys 99	- 11.4
7	Glu 13	- 8.95	49	Asn 105	- 5.29
8	Asn 14	- 7.05	50	Thr 108	- 3.71
9	Glu 16	5.01	51	Leu 115	6.08
10	Phe 18	7.78	52	Gly 116	- 8.08
11	Met 19	1.21	53	Asp 117	- 6.63
12	Ala 21	4.98	54	Val 119	- 7.11
13	Met 22	5.41	55	Tyr 120	8.08
14	Gly 23	5.59	56	Ser 124	- 4.62
15	Leu 24	5.47	57	Ile 127	1.15
16	Asp 27	4.01	58		
17	Leu 28	7.28	59		
18	Ile 29	- 0.48	60		
19	Gln 30	- 7.96	61		
20	Lys 31	6.14	62		
21	Gly 32	3.40	63		
22	Lys 33	- 7.66	64		
23	Ile 35	6.65	67		
24	Gly 37	9.24	68		
25	Glu 40	4.62	69		
26	Ile 41	5.89	70		
27	Val 42	4.43	71		
28	His 43	5.59	72		
29	Glu 44	- 2.19	73		
30	Gly 55	3.77	74		
31	Lys 57	3.58	75		
32	Val 58	4.92	76		
33	Leu 65	2.49	77		
34	Gly 66	- 14.8	78		
35	Glu 67	4.80	79		
36	Glu 68	- 4.98	80		
37	Met74	1.82	81		
38	Glu 77	- 0.33	82		
39	Lys 78	4.50	83		
40	Val 79	4.68	84		
41	Val 82	- 0.73	85		
42	Met 85	- 12.4	86		

[1]Measured in IPAP-HSQC experiments for ^{15}N-apo-L-FABP in 5 % $C_{12}E_5$/hexanol aligning media at 30 $^{\circ}$C.

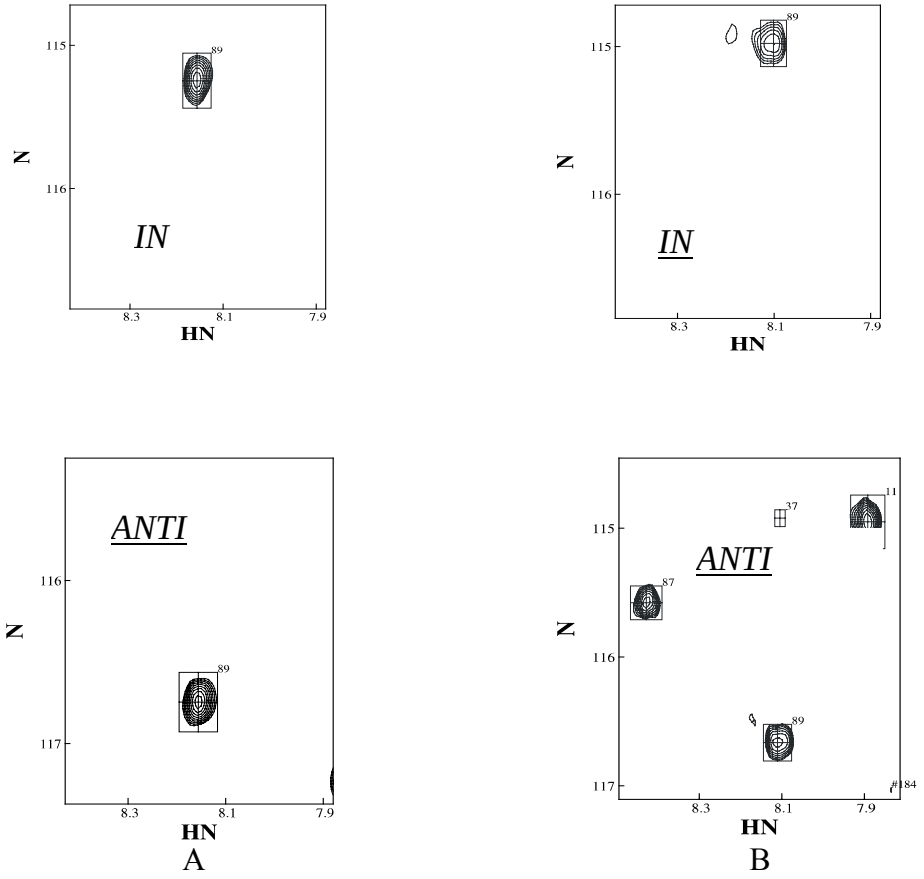

Figure 3.19: Portions of spectra of IPAP-HSQC for Asn 89. a) ^{15}N-apo-L-FABP in-phase (top panel) and anti-phase (bottom panel) and b) ^{15}N-apo-L-FABP with 5 % $C_{12}E_5$/hexanol aligning media in-phase (top panel) and anti-phase (bottom panel) at 30 $^{\circ}$C.

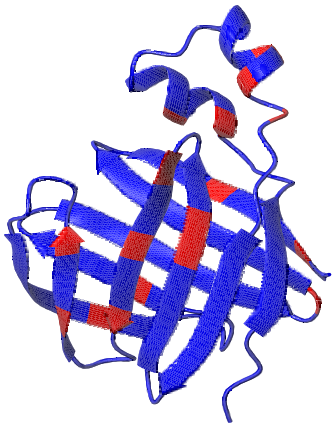

Figure 3.20: Three-dimensional drawing of apo-(oleate)-L-FABP from the crystal structure (Thompson, 1997). Regions highlighted in red represent residues with measured RDCs to refine diverse regions of the apo protein structure.

		Apo	Apo+RDCs	Holo
Restraints				
NOEs:	medium-range (i<4)	270	270	222
	long-range	642	642	601
	total NOEs	2462	2462	2614
H-bonds		90	90	68
^{3}J coupling		86	86	62
RDCs		----	57	----
RMSD :	Backbone	1.04 ± 0.34	0.72 ± 0.25	0.81± 0.17
	Heavy atoms	1.54 ± 0.28	1.24 ± 0.24	1.33 ± 0.15
Ramachandran space				
Most favored (%)		89.5	88.6	90.4
Additionally allowed (%)		8.0	9.9	7.0
Generously allowed (%)		1.3	1.4	1.8
Disallowed (%)		1.2	0.2	0.8

Table 3.8: NMR structural statistics for apo-L-FABP with and without RDC angular constraints and holo-L-FABP with two bound oleates.

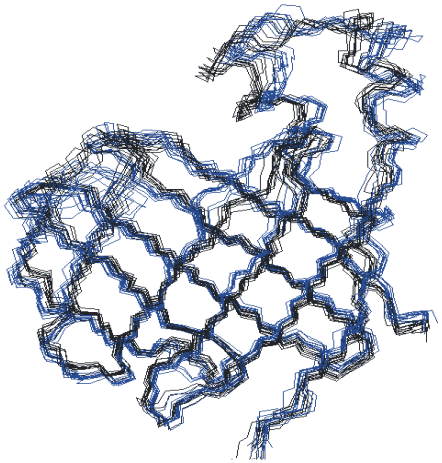

Figure 3.21: Three-dimensional backbone traces of 20 NOE-derived NMR structures of apo-L-FABP (blue) and apo-L-FABP with RDC angular constraints (black). A total of 100 NMR structures were calculated with each set of restraints (He et al., 2007).

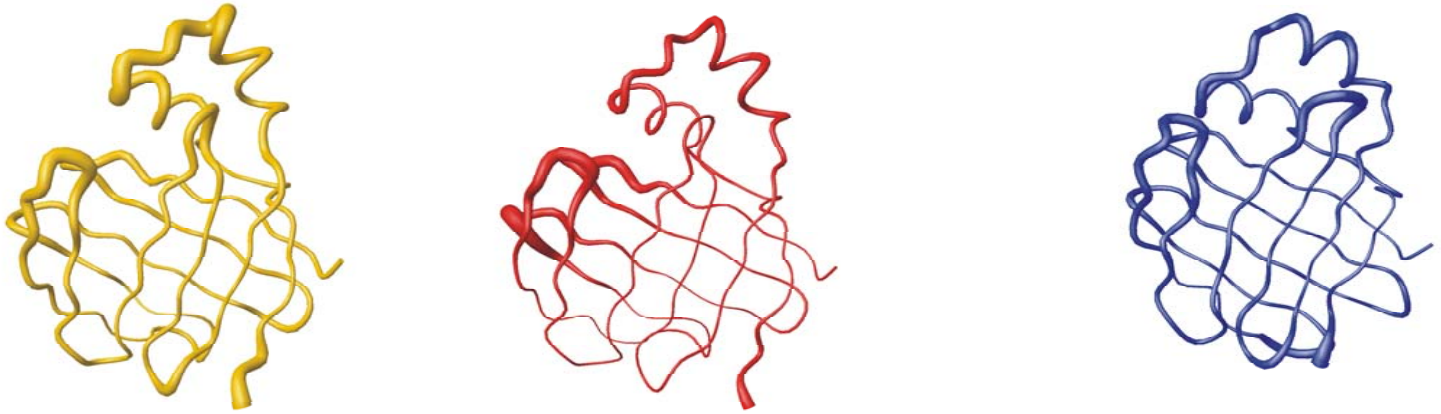

A apo B apo+ RDC C holo

Figure 3.22: Three-dimensional 'worm plot' representations of the NMR-derived structures of a) apo-L-FABP, b) apo-L-FABP with RDC, and c) holo (oleate)-L-FABP. Backbone RMSDs equal 1.04 ± 0.34, 0.72 ± 0.25, and 0.81± 0.17, for a, b, and c, respectively. The thickness of the traces reflects the square of the backbone RMSD, emphasizing regions of large structural variability.

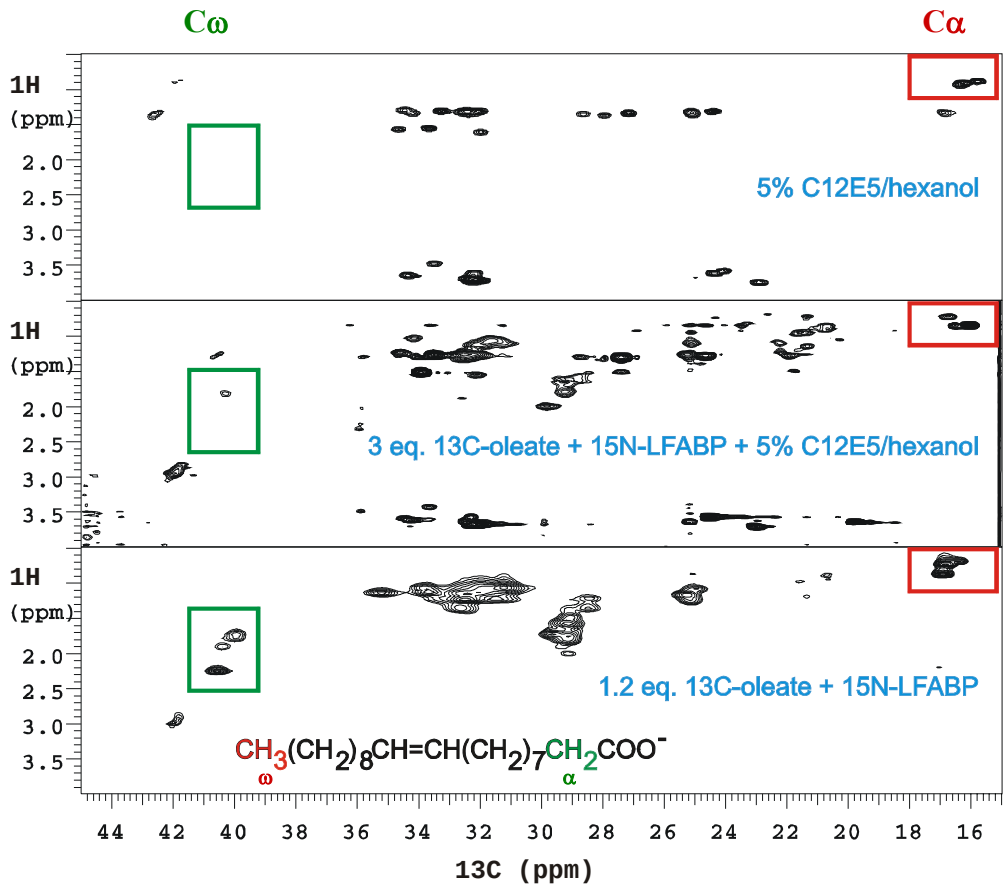

Figure 3.23: ^{13}C HSQC spectra of $C_{12}E_5$/hexanol (top panel), holo (oleate)-L-FABP in 5 % $C_{12}E_5$/hexanol (middle panel), and holo (oleate)-L-FABP (bottom panel). Red squares denote resonances for C_ω, whereas green squares correspond to C_α.

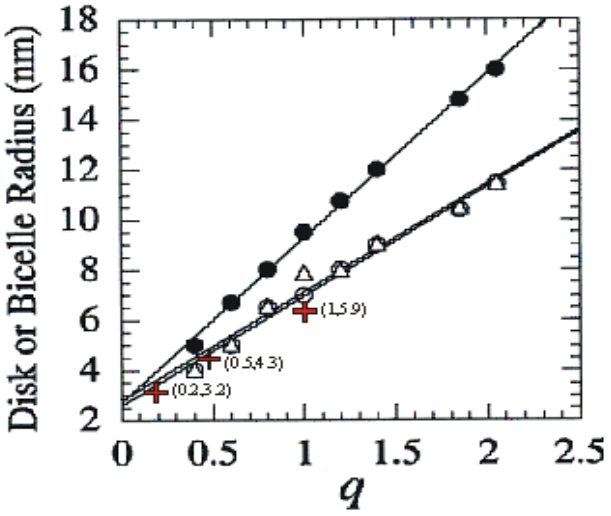

A

Mean Diam. 11.9 (nm)
Rel. Var. 0.012
Skew 0.430
RmsError 5.2855e-04

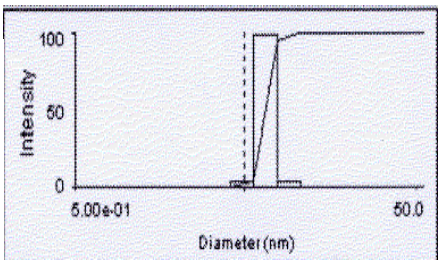

q = 1.0

B

Mean Diam. 8.6 (nm)
Rel. Var. 0.038
Skew 0.430
RmsError 1.4546e-03

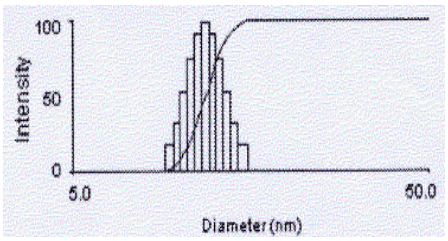

q = 0.5

C

Mean Diam. 6.5 (nm)
Rel. Var. 0.010
Skew 1.388
RmsError 2.1658e-03

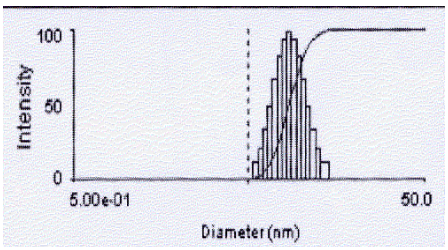

q = 0.2

D

Figure 3.24: a) Variation in bicelle radius (r) with phospholipid ratio (*q*) (q = [long chain phospholipids]/[short chain phospholipids]) as determined from QLS measurements (Δ)(Glover et al., 2001), an ideal bicelle theoretical model (•), a refined bicelle model accounting for phospholipid head group surface area (o), and current QLS measurements (+). Bicelles with q values equal to b) 0.2, c) 0.5, and d) 1.0 and 2.5 w/w lipid have hydrodynamic radii of 3.2, 4.3, and 5.9 nm, respectively.

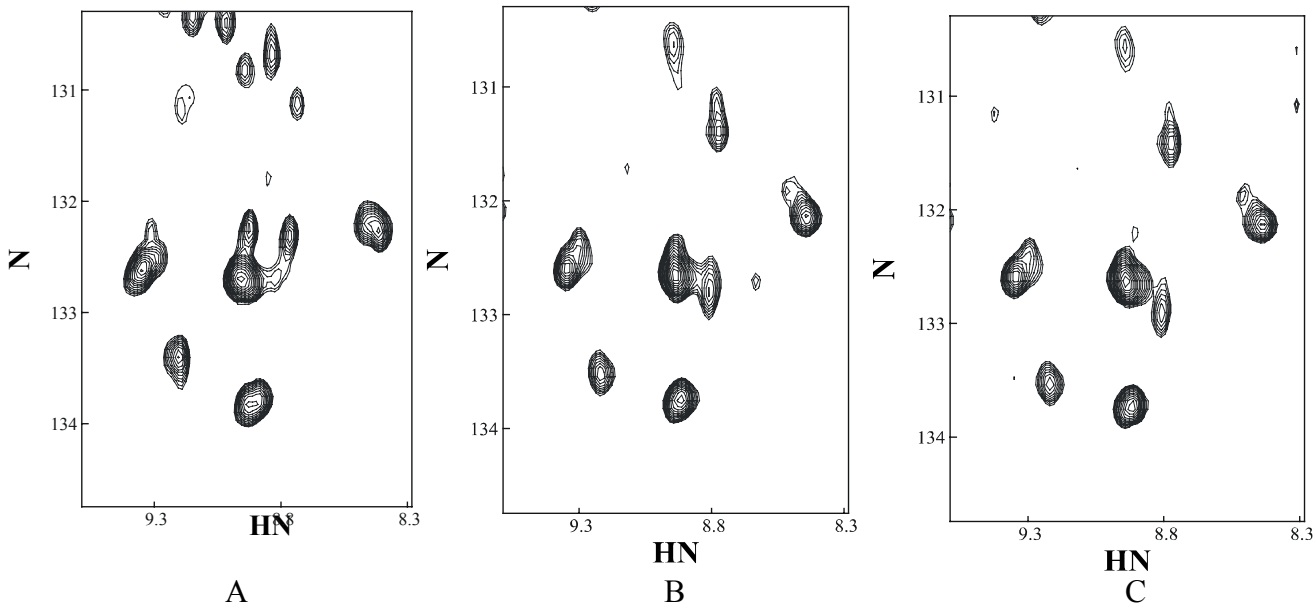

Figure 3.25: ^{15}N HSQC spectra of ^{15}N-apo-L-FABP titrated with q = 0.5 bicelles a) 0.2, b) 0.4, and c) 0.8 molar equivalents of acidic phospholipid bicelle at 20 °C.

Table 3.9: Highly Perturbed Sites of L-FABP in Isotropic Phospholipid Bicelles

Residue	Perturbation (Hz) [1]
Phe 3	**106.2**
Gly 32	**75.0**
Val 38	**77.3**
Ser 39	**159.7**
Ile 52	**73.5**
Ser 56	**133.5**
His 60	**110.9**
Glu 62	**81.7**
Glu 72	**95.0**
Thr 73	**140.4**
Val 92	**96.7**
Ile 109	**99.1**
Asn 111	**60.6**
Lys 121	**97.3**
Val 123	**85.3**
Lys 125	**77.9**
Average for all residues	**33.2**

[1] Measured for ^{15}N apo-L-FABP with 0.8 molar equivalent of acidic bicelle at 20 $^{\circ}$C.

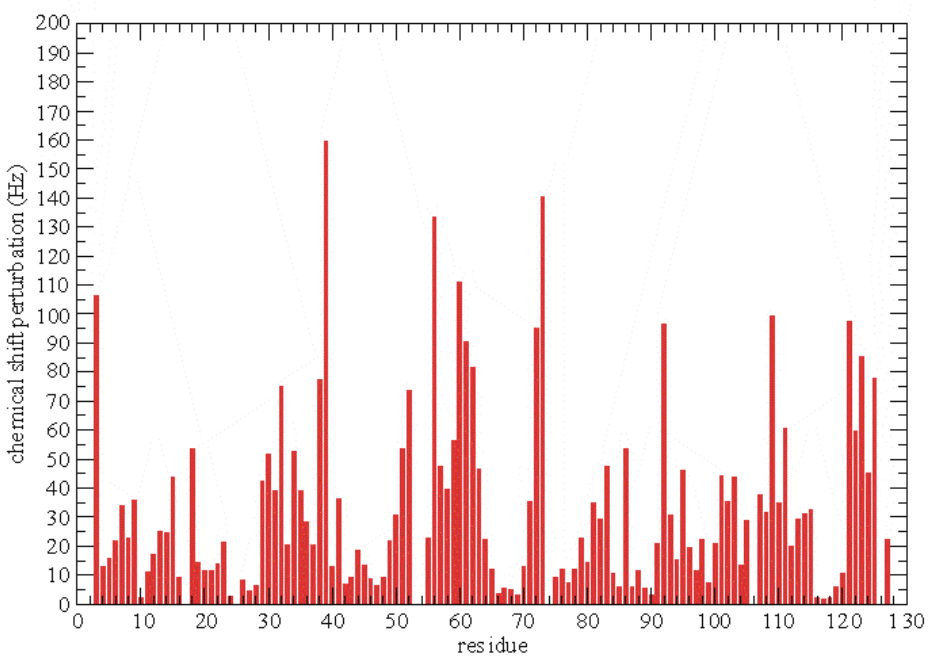

Figure 3.26: Chemical shift perturbation bar plot of ^{15}N L-FABP with 0.4 molar equivalent of q=0.5 acidic bicelle versus ^{15}N apo-L-FABP. Chemical shift perturbations average 33.2 ± 31.8 Hz.

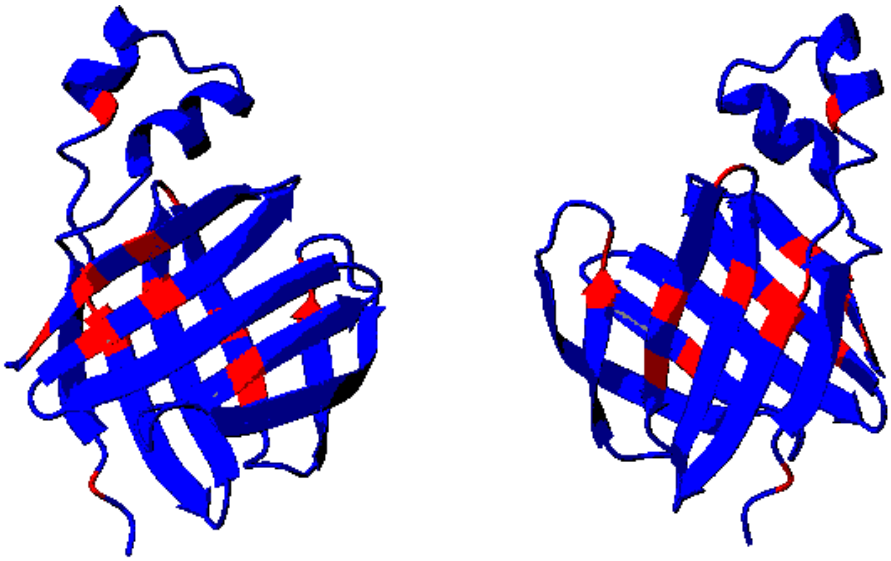

Figure 3.27: Two views of the crystal structure of ^{15}N L-FABP. Regions encoded in red represent residues with chemical shift perturbation in excess of 1 standard deviation beyond the mean for ^{15}N L-FABP with 0.4 molar equivalent of acidic bicelle.

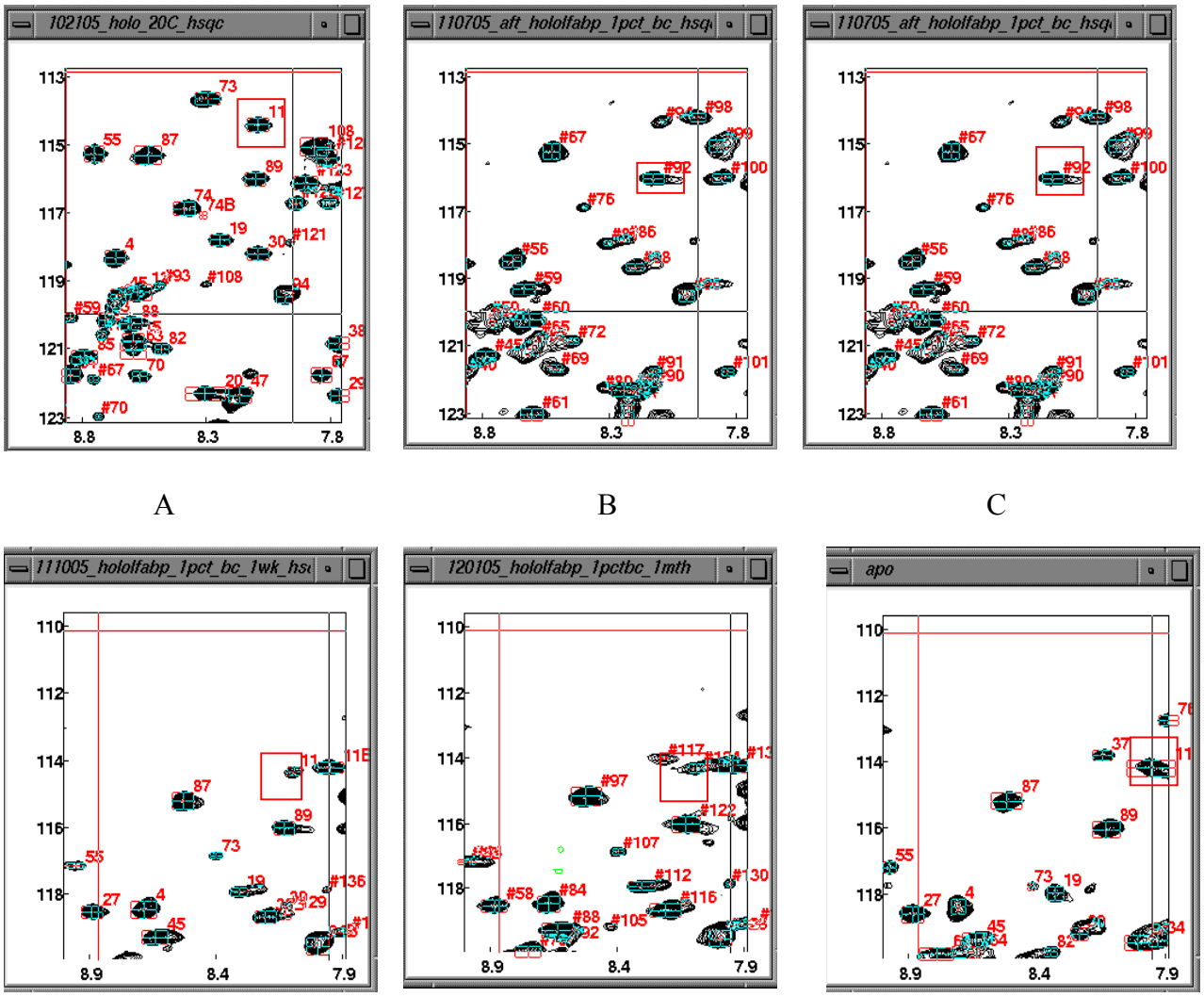

Figure 3.28: Portions of HSQC spectra of ^{15}N holo-(oleate)-L-FABP with 0.4 equivalents of acidic bicelle: a) immediately after sample preparation; and after b) 1 day; c) 3 days; d) 7 days; and e) 30 days of bicelle addition 20 $^{\circ}$C as compared with f) ^{15}N apo-L-FABP (no bicelle). Changes in peak positions with time are illustrated by the boxes in each spectrum.

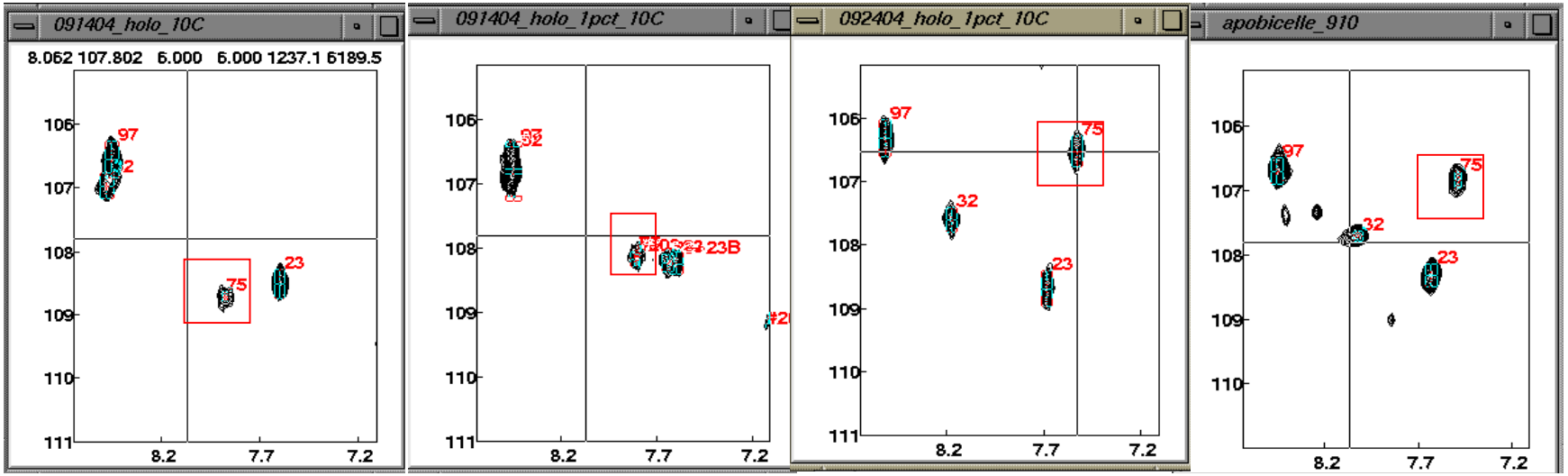

Figure 3.29: Portions of HSQC spectra of a) ^{15}N holo-(oleate)-L-FABP; after b) 4 days; c) 14 days of adding 0.4 equivalents of acidic bicelle 10 $^{\circ}$C as compared with d) ^{15}N apo-L-FABP (with 0.4 eq acidic bicelle), under similar conditions. Changes in peak positions with time are shown by the boxes in each spectrum.

Table 3.10: Chemical shift perturbation of HSQC spectra of holo-(oleate)-L-FABP versus time for highly perturbed residues [1]

holo-L-FABP vs holo-L-FABP / 1 % bicelle (1 day)		holo-L-FABP vs holo-L-FABP / 1 % bicelle (1 week)	
Residue	Perturbation (Hz)	Residue	Perturbation (Hz)
Gly 32	109.2	Gly 32	281.3
Asp 34	134.4	Asp 34	179.6
Ser 56	128.5	Ser 56	128.9
Lys 57	176.6	Lys 57	214.7
Glu 72	52.00	Glu 72	73.0
Thr 73	205.8	Thr 73	206.1

[1] Mean chemical shift perturbations were 26.1 and 46.9 Hz after 1 day and 1 week, respectively, after addition of 1 % bicelle.

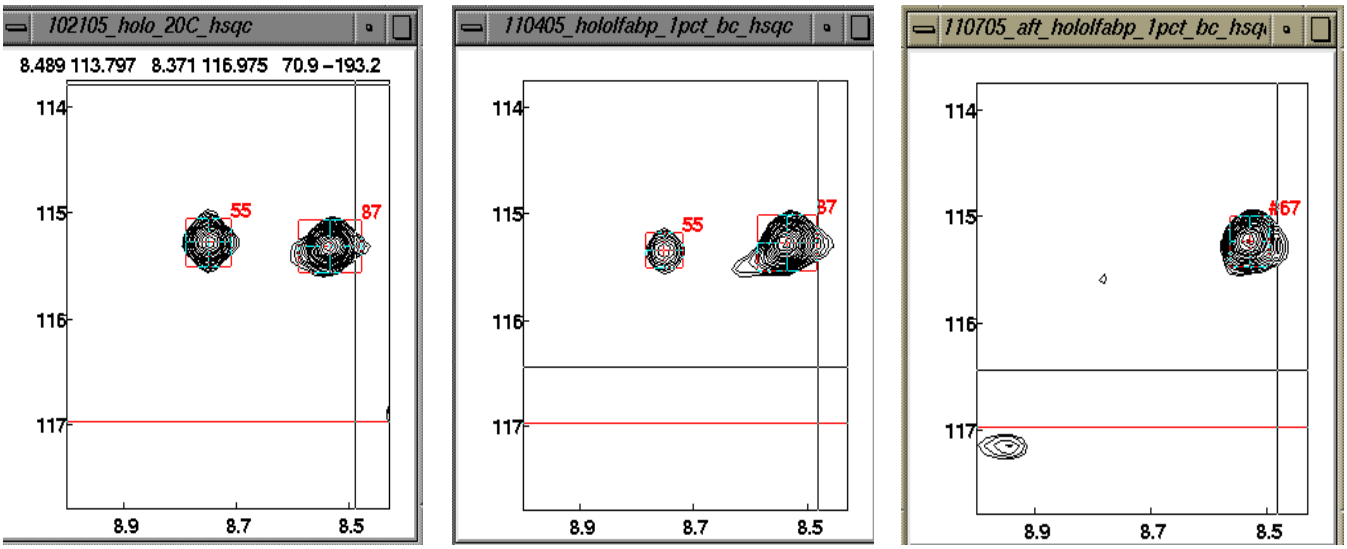

HN
A

HN
B

HN
C

Figure 3.30: Portions of the HSQC spectra of a) ^{15}N holo-(oleate)-L-FABP with 0.4 equivalents of acidic bicelle after b) 1 day, and c) 3 days of bicelle addition.

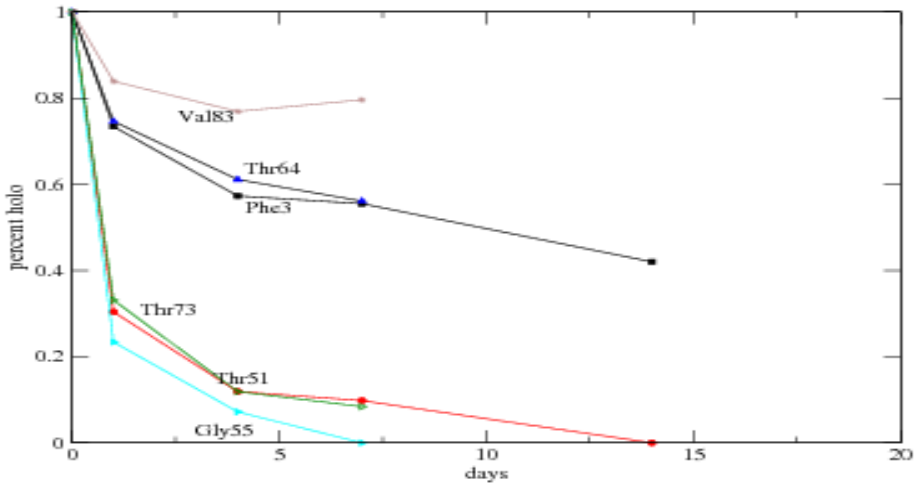

Figure 3.31: Change in ratio of peak volumes of holo-L-FABP to holo-L-FABP with 1 % acidic bicelle after 1 day, 3 days, 7 days, and 30 days of 1 % acidic bicelle addition (Figure 3.28a, b, c, and d, respectively) for residues at the internal binding site (Thr 64, Val 83), and in portal site (Thr 51, Gly 55, and Thr 73).

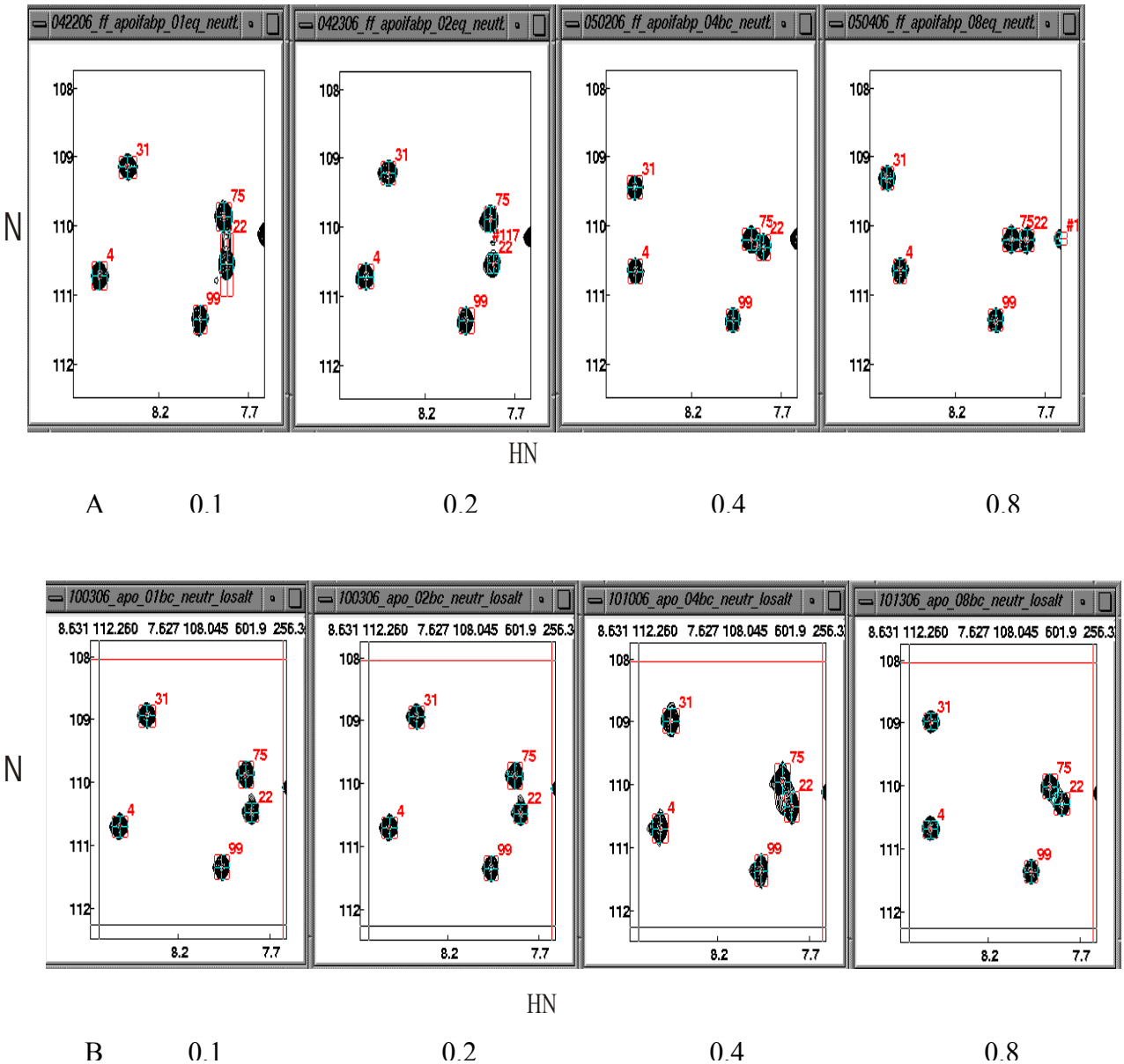

Figure 3.32: Regions of the HSQC spectra of ^{15}N-I-FABP for titrations with neutral bicelles in a) high salt (50 mM NaH_2PO_4, 100 mM NaCl); b) low salt (10 mM NaH_2PO_4, 50 mM NaCl); c) acidic bicelle in high salt. In all titrations, protein was titrated with 1) 0.1, 2) 0.2, 3) 0.4, and 4) 0.8 molar equivalents of bicelle at 20 C. All spectra were compared with d) ^{15}N-apo-I-FABP.

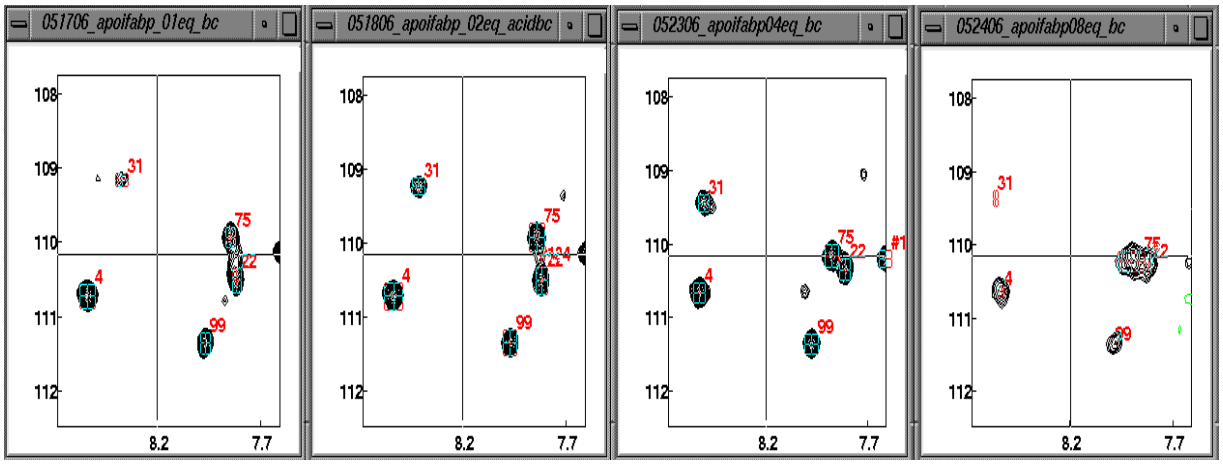

C 0.1 0.2 0.4 0.8

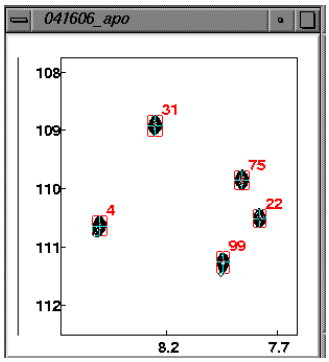

D

Figure 3.32: Regions of the HSQC spectra of ^{15}N-I-FABP for titrations with neutral bicelles in a) high salt (50 mM NaH_2PO_4, 100 mM NaCl); b) low salt (10 mM NaH_2PO_4, 50 mM NaCl); c) acidic bicelle in high salt. In all titrations, protein was titrated with 1) 0.1, 2) 0.2, 3) 0.4, and 4) 0.8 molar equivalents of bicelle at 20 C. All spectra were compared with d) ^{15}N-apo-I-FABP.

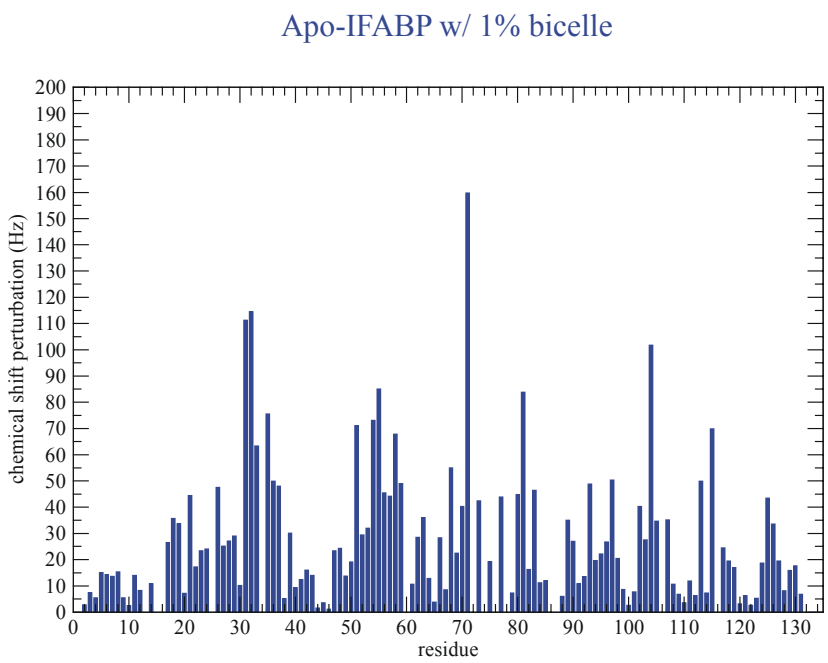

Figure 3.33: Chemical shift perturbation bar plot of ^{15}N apo-IFABP with 0.4 molar equivalent of q=0.5 acidic bicelles versus ^{15}N apo-IFABP. Measured chemical shift perturbations average 35.4 ± 27.8 Hz.

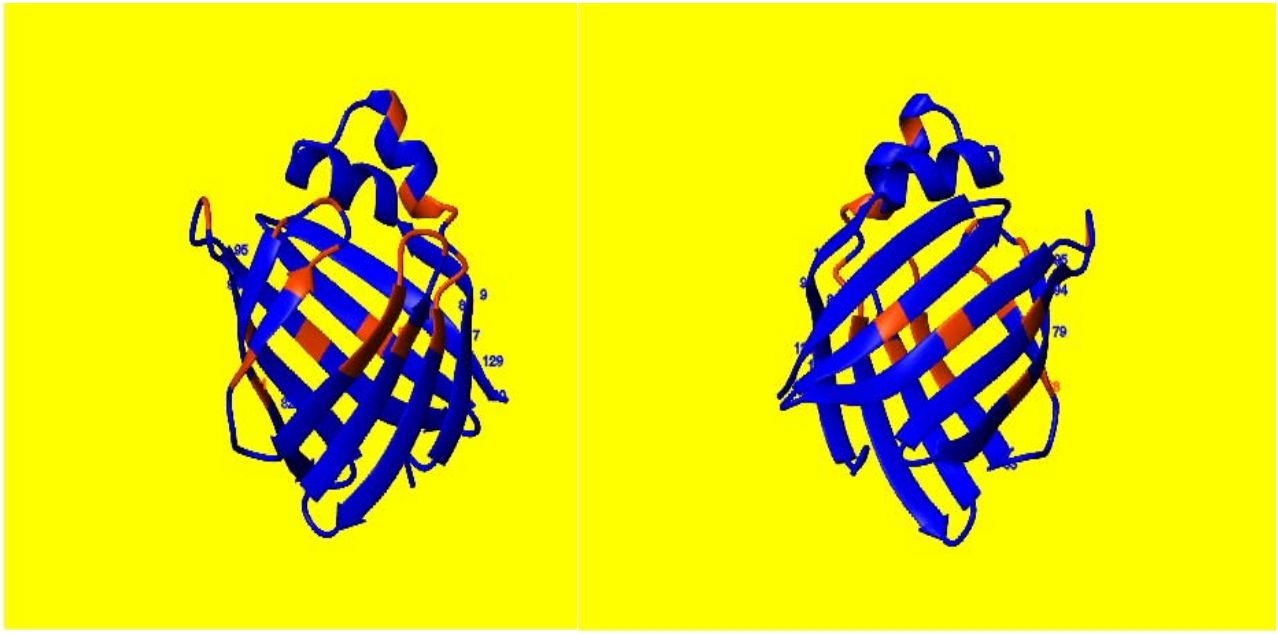

Figure 3.34: Two views of the crystal structure of I-FABP. Regions encoded in red present residues with chemical shift perturbation in excess of 1 standard deviation beyond the mean for ^{15}N I-FABP with 0.4 molar equivalent of q=0.5 acidic bicelle.

Table 3.11: Chemical shift perturbation of apo-I-FABP with phospholipid bicelles [1]

-	0.1 eq	0.2 eq	0.4 eq	0.8 eq	residues with largest perturbation [2]
a) apo-I-FABP/ acidic bicelle (50 mM NaH_2PO_4,100 mM NaCl)	**37.3±36.6**	**40.3±39.1**	**45.7±50.1**	**48.2±51.5**	**Gly31, Ala32, Lys37, Arg56, Asn57, Ile58, Glu63, Phe68, Ser71, Glu77, Thr81, Phe93, Leu102, Ala104, Val105, Arg106, Leu113**
b) apo-I-FABP/ neutral bicelle (50 mM NaH_2PO_4,100 mM NaCl)	**36.4±35.7**	**40.2±39.3**	**43.6±47.0**	**46.2±48.5**	
c) apo-I-FABP/ neutral bicelle (10 mM NaH_2PO_4,50 mM NaCl)	**38.2±34.1**	**43.2±37.0**	**44.6±46.7**	**48.7±42.4**	

[1] Mean chemical shift perturbation ± standard deviation (Hz) values for HSQC spectra of ^{15}N-apo-I-FABP versus ^{15}N-apo-I-FABP with bicelles in high salt buffer with a) acidic and b) neutral bicelles and in c) low salt buffer with neutral bicelle. The table also includes residues with the largest chemical shift perturbation.

[2] Residues whose peaks shift > mean perturbation + 1 standard deviation.

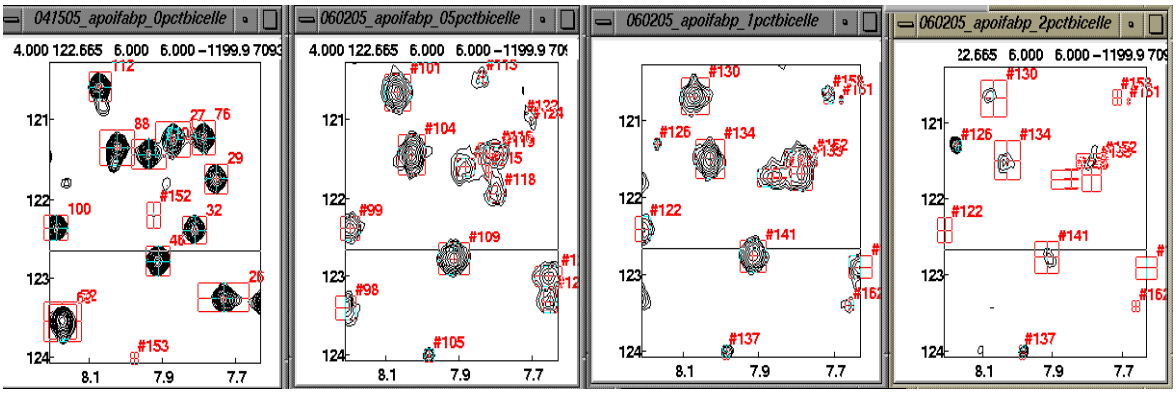

A B C D

Figure 3.35: Regions of the HSQC spectra of a) ^{15}N-apo-I-FABP titrated with b) 0.5 %, c) 1.0 %, and d) 2 % of acidic bicelle in low salt (10 mM NaH_2PO_4, 50 mM NaCl) buffer. Note that all spectra are displayed at the same contour level.

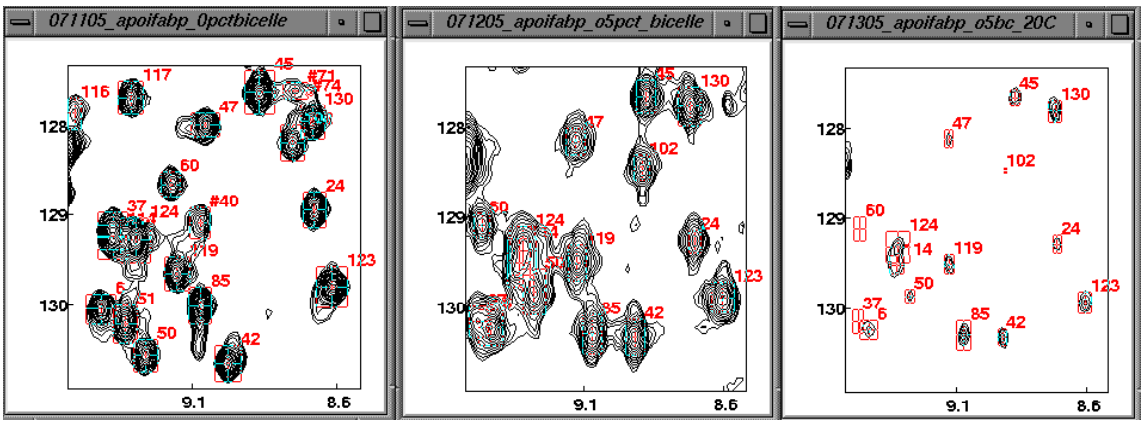

A B C

Figure 3.36: Regions of the HSQC spectra of a) ^{15}N-apo-I-FABP (0 % bicelle) titrated with 0.5 % (0.2 equivalent) acidic bicelle in low salt buffer (10 mM NaH_2PO_4, 50 mM NaCl) after b) 1 day and c) 2 days of bicelle addition. Note that all spectra are displayed at the same contour level.

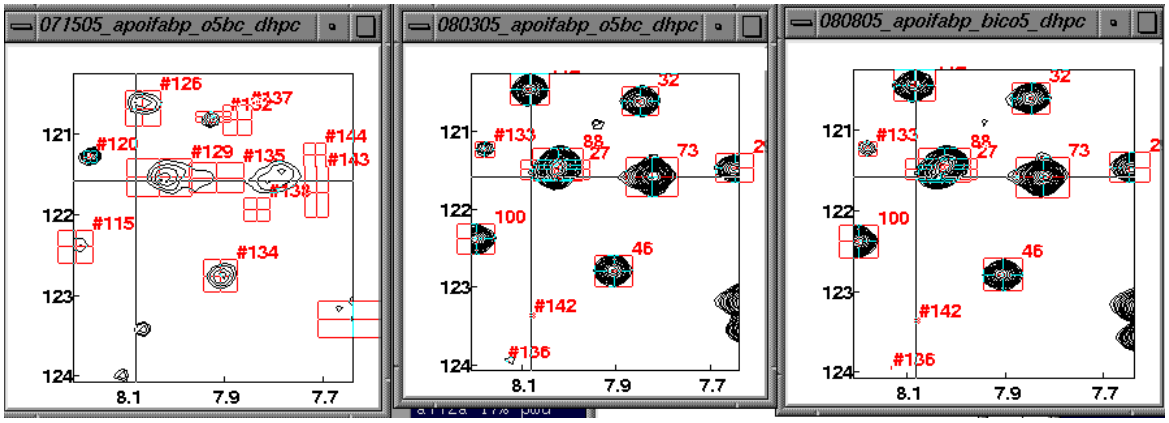

A B C

Figure 3.37: Regions of the HSQC spectra of ^{15}N-apo-I-FABP with 2 % (1.3 equivalents) (correct) of acidic bicelle in low salt (10 mM NaH_2PO_4, 50 mM NaCl) buffer after a) 1 day b) 1 week, and c) 4 weeks of adding DHPC. Note that all spectra are displayed at the same contour level.

Residue	^{15}N	^{1}HN	^{13}CO	$^{13}C^{\alpha}$	$^{13}C^{B}$	Residue	^{15}N	^{1}HN	^{13}CO	$^{13}C^{\alpha}$	$^{13}C^{B}$
Ala[1]			173.8	52.3	19.2	Gly[31]	108.0	8.64	174.6	47.2	
Phe[2]	117.4	9.33	174.1	59.7	40.0	Ala[32]	120.3	7.81	177.6	53.7	18.7
Asp[3]	117.0	7.96	176.4	55.2	41.5	His[33]	117.9	7.49	173.4	53.8	28.2
Gly[4]	109.3	8.54	171.5	43.9		Asp[34]	118.6	7.40	176.4	54.9	41.3
Thr[5]	117.7	8.34	172.4	62.7	69.9	Asn[35]	119.7	9.18	174.6	53.8	37.6
Trp[6]	128.8	9.46	175.3	55.0	31.6	Leu[36]	120.0	7.03	174.5	57.3	42.3
Lys[7]	125.1	9.64	176.7	54.9	35.6	Lys[37]	128.7	9.54	175.2	54.9	36.1
Val[8]	129.9	8.76	173.1	65.0	31.5	Leu[38]	124.0	9.43	177.2	52.6	45.9
Asp[9]	128.1	9.73	175.0	55.3	46.5	Thr[39]	121.4	9.11	174.6	62.7	70.2
Arg[10]	114.2	7.78	172.4	55.2	32.3	Ile[40]	130.2	9.61	175.9	61.4	40.1
Asn[11]	118.2	8.73	175.1	51.6	43.4	Thr[41]	123.5	8.83	172.4	61.5	71.6
Glu[12]	121.1	9.51	175.6	55.9	32.2	Gln[42]	129.0	8.95	174.9	54.5	29.7
Asn[13]	124.1	9.43	175.6	54.6	39.7	Glu[43]	130.4	8.94	176.0	55.3	30.8
Tyr[14]	121.9	8.35	177.4	59.9	40.2	Gly[44]	118.4	9.04	173.6	47.3	
Glu[15]	120.9	9.02	178.8	61.4	28.1	Asn[45]	126.2	8.87	173.6	53.2	38.9
Lys[16]	120.2	8.08	179.7	58.7	31.5	Lys[46]	121.5	7.95	174.7	55.6	34.5
Phe[17]	121.8	7.67	175.9	62.0	40.5	Phe[47]	126.8	9.16	174.5	56.4	43.0
Met[18]	118.7	8.30	177.9	60.1	34.3	Thr[48]	115.6	8.32	173.8	62.0	70.3
Glu[19]	120.2	8.31	180.4	59.9	29.4	Val[49]	128.8	9.72	175.4	61.9	34.5
Lys[20]	124.3	8.10	178.8	57.3	31.8	Lys[50]	128.8	9.33	176.0	55.6	32.1
Met[21]	115.6	7.54	176.3	56.1	32.4	Glu[51]	130.0	9.36	175.1	55.4	30.6
Gly[22]	108.8	7.81	174.3	45.5		Ser[52]	122.3	9.11	172.6	56.7	65.3
Ile[23]	122.3	7.43	176.1	60.6	37.1	Ser[53]	121.9	9.10	174.5	56.9	68.0
Asn[24]	128.3	8.77	175.7	54.1	39.2	Asn[54]	116.5	9.00	176.1	54.7	37.9
Val[25]	121.3	8.43	176.5	66.2	31.9	Phe[55]	115.3	8.14	176.0	59.0	40.7
Val[26]	121.6	7.64	178.9	66.2	31.9	Arg[56]	114.0	7.50	172.5	55.7	31.0
Lys[27]	119.2	7.88	179.0	58.9	32.6	Asn[57]	119.9	8.53	174.6	53.2	40.8
Arg[28]	120.8	8.57	178.6	59.6	30.8	Ile[58]	119.0	8.89	173.0	59.9	43.1
Lys[29]	120.1	7.68	179.4	59.5	32.1	Asp[59]	123.6	8.56	175.3	53.3	41.7
Leu[30]	120.6	7.43	180.3	57.2	42.2	Val[60]	127.5	9.49	174.0	62.5	34.2

Residue	^{15}N	^{1}HN	^{13}CO	$^{13}C^{\alpha}$	$^{13}C^{B}$	Residue	^{15}N	^{1}HN	^{13}CO	$^{13}C^{\alpha}$	$^{13}C^{B}$
Val[61]	127.0	8.25	175.5	60.2	34.4	Lys[92]	125.8	7.58	174.8	55.2	33.1
Phe[62]	122.3	8.39	172.5	55.5	40.9	Phe[93]	124.3	8.71	174.8	55.9	43.6
Glu[63]	120.9	9.61	177.9	53.5	31.9	Lys[94]	121.5	9.35	177.2	55.0	35.9
Leu[64]	125.6	8.96	178.7	56.6	41.3	Arg[95]	124.2	8.85	178.8	56.8	31.0
Gly[65]	109.3	9.27	173.7	46.2		Val[96]	126.6	8.47	177.6	65.5	32.4
Val[66]	123.2	8.02	176.5	62.6	33.0	Asp[97]	119.2	9.15	178.9	56.6	38.8
Asp[67]	133.0	8.89	175.3	55.3	41.3	Asn[98]	117.8	8.62	177.6	51.6	39.2
Phe[68]	122.3	9.55	171.6	56.4	41.6	Gly[99]	110.0	8.00	174.3	46.5	
Ala[69]	122.0	8.31	176.6	50.6	21.4	Lys[100]	121.0	8.23	176.4	56.9	34.1
Tyr[70]	124.3	8.63	172.3	57.9	43.2	Glu[101]	120.6	8.50	175.0	56.6	31.9
Ser[71]	122.3	7.68	174.5	55.9	65.0	Leu[102]	127.7	9.08	174.5	54.9	46.4
Leu[72]	124.8	8.72	179.3	55.4	42.6	Ile[103]	126.2	8.54	175.2	59.0	39.2
Ala[73]	124.1	9.28	177.1	55.0	18.0	Ala[104]	131.7	9.33	175.3	49.5	23.5
Asp[74]	113.9	7.66	176.1	53.8	40.4	Val[105]	121.6	8.97	176.2	61.0	36.1
Gly[75]	109.1	7.92	174.7	44.4		Arg[106]	125.8	9.47	173.7	55.0	34.0
Thr[76]	120.4	7.90	173.8	65.2	67.9	Glu[107]	121.1	8.58	172.9	54.6	34.4
Glu[77]	129.5	8.56	175.6	56.7	30.4	Ile[108]	124.5	8.81	177.0	58.5	37.4
Leu[78]	124.5	9.34	177.3	53.6	46.7	Ser[109]	123.7	8.98	175.6	56.6	63.9
Thr[79]	112.1	8.57	173.9	60.0	71.2	Gly[110]	120.4	9.28	174.3	47.7	
Gly[80]	112.2	8.55	169.9	46.8		Asn[111]	124.0	8.89	174.2	53.3	38.8
Thr[81]	197.3	6.59	173.2	59.8	72.9	Glu[112]	119.0	8.14	173.6	55.3	33.0
Trp[82]	123.6	9.26	176.2	56.2	33.2	Leu[113]	124.7	8.25	174.9	54.0	43.5
Thr[83]	114.3	9.22	172.7	60.8	72.2	Ile[114]	128.2	9.38	175.9	61.3	39.3
Met[84]	122.9	8.97	176.0	54.6	33.5	Gln[115]	130.2	9.27	174.2	54.2	31.6
Glu[85]	128.8	9.12	176.6	54.9	30.4	Thr[116]	122.7	9.09	173.8	61.4	70.3
Gly[86]	117.8	9.10	174.3	47.5		Tyr[117]	125.3	9.27	175.6	54.6	42.8
Asn[87]	124.5	8.83	174.4	53.2	38.6	Thr[118]	116.5	9.24	174.3	62.3	71.0
Lys[88]	120.0	8.05	174.7	55.7	35.3	Tyr[119]	128.1	9.14	173.6	58.2	43.5
Leu[89]	124.3	8.49	175.8	53.8	44.4	Glu[120]	126.7	9.56	175.9	56.6	28.4
Val[90]	125.2	9.54	174.8	62.7	33.9	Gly[121]	103.4	8.62	174.2	45.4	
Gly[91]	124.1	10.2	171.5	45.0		Val[122]	124.3	8.38	173.5	62.6	32.9

Residue	^{15}N	^{1}HN	^{13}CO	$^{13}C^{\alpha}$	$^{13}C^{B}$	Residue	^{15}N	^{1}HN	^{13}CO	$^{13}C^{\alpha}$	$^{13}C^{B}$
Glu^{123}	128.3	8.66	175.6	54.0	33.0	Phe^{128}	127.7	10.0	175.4	56.3	42.9
Ala^{124}	128.0	9.33	176.0	50.5	24.1	Lys^{129}	120.5	9.02	176.2	55.0	36.0
Lys^{125}	116.8	9.00	176.2	54.8	37.9	Lys^{130}	126.7	8.75	176.9	56.9	33.3
Arg^{126}	120.3	9.25	173.5	61.4	39.9	Glu^{131}	132.2	8.45	181.0	58.1	31.2
Ile^{127}	124.8	8.86	174.9	61.4	39.9						

Table 3.12: Backbone chemical shift assignments of ^{15}N/^{13}C-apo-I-FABP with 0.4 eq of neutral bicelle in low salt (10 mM NaH_2PO_4, 50 mM NaCl) buffer at pH 7.0 and 25 $^{\circ}$C.

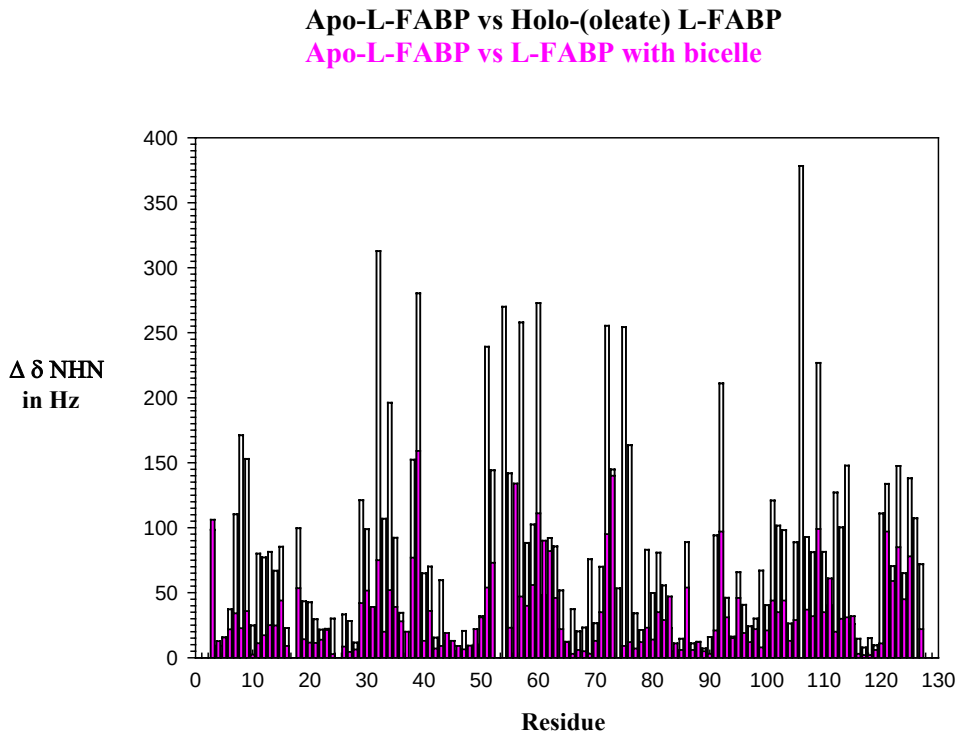

Figure 3.38: Chemical shift perturbation bar plot of ^{15}N L-FABP with 3 equivalents of oleic acid (white bars) and 0.8 equivalents of acidic bicelles (pink bars). Measured perturbations are 89.2 ± 93.2 Hz with oleic acid and 33.24 ± 31.8 for L-FABP with bicelles.

Conclusions

L-FABP can accommodate long-chain fatty acids (≥ 16 carbons) within its binding cavity, reaching a 2:1 FA: protein stoichiometry. Small degrees of alkyl chain unsaturation does not seem to affect the site or degree of environmental perturbation observed from NMR chemical shifts of particular protein residues. However, shortening of the carbon chain (caprylate), introducing multiple unsaturation (EPA), or introducing a bulky headgroup (lysoPC) all compromise L-FABP ligand binding. These trends are likely to reflect steric constraints, hydrophobic interactions, and solubility considerations. Even though the regions of chemical shift perturbation for L-FABP with these ligands are generally consistent with predictions from the crystal structure of holo-(oleate) L-FABP, particular residues that are located in close proximity to the FA chain cannot be identified from our NMR data alone. The change in chemical environment for the protein residues reflected in holo-L-FABP amide NH HSQC spectra may result from a direct effect of ligand binding or from expulsion of water from the protein cavity upon ligand entry. Conversely, ligands could affect sidechain sites and leave the amide NH environments unchanged.

Our NMR results showing L-FABP possible unfolding events with both heme and protoporphyrin and maintenance of native conformation with oleate, palmitate, and lysoPC suggest that L-FABP prefers long-chain fatty acids and lysophospholipid ligands, although binding constants cannot be determined from these NMR data. Published reports of stronger L-FABP affinity for heme than oleate are not confirmed by our NMR experiments, but the discrepancies could reflect differences in protein concentration as well as salt content.

In addition, our finding of specific binding to lysophospholipids, which like fatty acids, are products of phospholipase hydrolysis and can be cytotoxic if present intracellularly at elevated concentrations, strengthens the view of L-FABP as not just a lipid transporter protein but also as a buffer against high lipid concentration in the cell. Although our results do not explain the binding of all reported ligands, they illustrate site-specific L-FABP binding and elucidate the factors that govern the ligand recognition that is involved in L-FABP's diverse functions (e.g., regulation of lipid metabolism).

Measured RDCs for the apo form of L-FABP have removed orientational ambiguities in the structure of its portal region, confirming a more open lid conformation than is typical of most iLBPs. This striking result may explain L-FABP's ability to accommodate two ligands in its binding cavity but nevertheless permit facile exchange with the bulk fatty acid. In addition, these angular constraints achieve structural refinement in the turns between its beta strands. A lower percentage of sterically disallowed regions of L-FABP with RDCs in the Ramachandran plot also indicates a better quality structure. No analogous measurements were possible for the holo form of L-FABP because the alignment media caused expulsion of one oleate ligand, but the structure was well determined in any case. Results for the apo protein confirm the advantage of RDC constraints as complementary to NOE distance constraints in a high resolution NMR-derived structure, especially in structure determination of proteins with multi- or highly mobile domains.

A system of isotropically tumbling bicelles has been examined for the study of FABP interactions with lipid membranes. The suitability of these bicelles for NMR structural studies is attributed to their small size and limited spectral broadening effects, which facilitate NMR data

interpretation. Our approach combines the advantage of NMR as a highly sensitive technique for detecting macromolecular conformation and interactions with the choice of lipid media that resemble physiological lipid membranes morphologically and chemically. The neutral lipid system at low ionic strength is relatively stable (3-10 weeks) with FABPs, a class of water-soluble proteins that interact with lipids. This stability makes possible complete backbone resonance assignments for I-FABP in the bicellar medium, laying the groundwork for a full structure determination. However, structural evaluation of the complex is needed in order to validate this bicellar system and compare it with protein-micelle or protein-monomer aggregates. In addition, the applicability and stability of these media with integral membrane proteins are just beginning to be tested (Poget, et al., 2007).

Our NMR data are consistent with the reported role of FABP's portal region in lipid membrane interactions: residues in this region exhibit large chemical shift perturbations for I-FABP as expected for a favored collisional mechanism, but L-FABP shows a more dispersed pattern of perturbation under low salt conditions, consistent with its diffusional ligand-transfer mechanism in cells. Nonetheless, the similar degrees of average perturbation in neutral bicelles at both high and low ionic strength and in acidic bicelles at high ionic strength are surprising given the contrasting fatty acid transfer mechanism for these two FABPs. The minimal line broadening observed in most bicelle titration experiments is also unexpected for an assembly that is expected to be 40-50 kDa in molecular weight, suggesting that the proteins may actually bind to DHPC monomers or micelles rather than the bicelle assembly. Finally, the smaller degree of perturbation observed for L-FABP with bicelles as compared with long-chain fatty acid ligands may indicate a smaller degree of environmental change upon lipid association.

Bibliography

Abraham, R.J., Fisher, J., and Loftus P. (1988) Introduction to NMR spectroscopy. *John Wiley and Sons,* New York.

Amri, E.Z., Teboul, L., Vannier, C., Grimaldi, P.A., and Ailhaud, G. (1996) Fatty acids regulate the expression of lipoprotein lipase gene and activity in preadipose and adipose cells, *Biochem. J.* **314,** 541-546.

Andersson, A., and Mäler, L. (2002) NMR solution structure and dynamics of motilin in isotropic phospholipid bicellar solution, *J. Biomol. NMR.* **24,** 103-112.

Andersson, A. (2005) The applications of isotropic bicelles as model membranes, *Doctoral Thesis in Biophysics.* Stockholm University.

Aussenac, F., Lavigne, B., and Dufourc, E.J. (2005) Toward bicelle stability with ether-linked phospholipids: temperature, composition, and hydration diagrams by 2H and ^{31}P solid-state NMR*, Langmuir. 21,* 7129-7135.

Bachmann, P., Aue, W.P., Muller, L., and Ernst, R.R. (1977) Phase separation in two-dimensional NMR spectroscopy, *J. Magn. Reson.* **28,** 29-39.

Balla, G., Vercellotti, G.M., Muller-Eberhard, U., Eaton, J., and Jacob, H.S. (1991) Exposure of endothelial cells to free heme potentiates damage mediated by granulocytes and toxic oxygen species, *Lab. Invest.* **64,** 648-655.

Ballendiran, G.K., Schnutgen, F., Scapin, G., Borchers, T., Xhong, N., Lim, K., Gogbout, N., Spener, F., and Sacchettini, J. (2000) Crystal structure and thermodynamic analysis of human brain fatty acid-binding protein, *J. Biol. Chem.* **275,** 27045-27054.

Ballou, D., Veeger, C., Hoeven, T.A., and Coon, M.J. (1973) Properties of partially purified liver microsomal cytochrome *P*-450: acceptance of two electrons during anaerobic titration, *FEBS Letters* **38,** 337-340.

Banaszak, L.J., Winters, N., XU, Z., Bernlohr, D., Cowan, S., Jones, A. (1994) Lipid-binding proteins: a family of fatty acid and retinoid transport proteins, *Adv. Protein. Chem.* **45,** 89-151.

Barrientos, L.G., Dolan, A., and Gronenborn, A.M. (2000) Characterization of surfactant liquid crystal phases suitable for molecular alignment and measurement of dipolar couplings, *J. Biomol. NMR.* **16,** 329-337.

Bass, N.M. (1985) Function and regulation of hepatic and intestinal fatty acid binding proteins, *Chem. Phys. Lipid* **38,** 95-114.

Bax. A., Kontaxis, G., Tjandra, N. (2001) Dipolar couplings in macromolecular structure determination, *Methods Enzymol.* **339,** 127-174.

Benjamin, C. (1991) Laser Light Scattering: Basic Principles and Practice, *Academic Press Inc.,* London, U.K.

Bernolhr, D.A., Simpson, M.A., Hertzel, A.V., and Banaszak, L. (1997) Intracellular lipid-binding proteins and their genes, *Annu, Rev. Nutr.* **17,** 277-303.

Binnig, G., Quate, C.F., and Gerber, C. (1986) Atomic force microscope. *Phys. Rev. Lett.* **56,** 930-933.

Bloch, F., Hansen, W.W., and Packard, M.E. (1946) Nuclear induction, *Phys. Rev.* **69,** 127.

Blouin, A., Bolender, R.P., and Weibel, E.R. (1977) Distribution of organelles and membranes between hepatocytes and nonhepatocytes in the rat liver parenchyma: A stereological study, *J. Cell. Biol.* **72,** 441-455.

Borchers, T., and Spener, F. (1993) Involvement of arginine in the binding of heme and fatty acids to fatty acid-binding protein from bovine liver, *Mol. Cell. Biochem.* **123,** 23-27.

Bovey, F. (1988) Nuclear Magnetic Resonance, Second edition. *Academic Press Inc.,* London, U.K.

Brown, R.L., Wuthrich, K. (1977) NMR and ESR studies of the interactions of cytochrome c with mixed cardiolipin-phosphatidylcholine vesicles, *Biochim. Biophys. Acta.* **468,** 389-410.

Cavanagh, J., Fairbrother. W., Palmer, A., and Skelton, N. (2006) Protein NMR Spectroscopy: principles and practice. *Prentice Hall,* Upper Saddle River, New Jersey.

Cheng, L., Qian, S., Rothschild, C., Avignon, A., Lefkowith, J., Gordon, L, and Li, E. (1992) Alteration of the binding specificity of cellular retinol-binding protein II by site-directed mutagenesis, *J. Biol. Chem.* **267,** 24404-24412.

Chou, J.J., Kaufman, J.D., Stahl, S.J., Wingfield, P.T., and Bax, A. (2002) Micelle-induced curvature in a water-insoluble HIV-1 Env peptide revealed by NMR dipolar coupling measurement in stretched polyacrylamide gel, J. *Am. Chem. Soc.* **124,** 2450-2451.

Chmurzynska, A. (2006) The multigene family of fatty acid-binding proteins (FABPs): Function, structure and polymorphism, *J. Appl. Genet.* **47,** 39-48.

Clore, G.M., Groneborn, A.M., and Tjandra, N. (1998) Direct structure refinement against residual dipolar couplings in the presence of rhombicity of unknown magnitude, *J. Magn. Reson.* **131,** 159-162.

Corr, P.B., Gross, R.W., and Sobel, B.E. (1984) Amphipathic metabolites and membrane dysfunction in ischemic myocardium. *Circul. Res.* **55,** 135-154.

Corsico, B., Cistola, D.P., Frieden, C., and Storch, J. (1998) The helical domain of intestinal fatty acid binding protein is critical for collisional transfer of fatty acids to phospholipid membranes, *Proc. Natl. Acad. Sci. USA.* **95,** 12174-12178.

Corsico, B., Liou, H.L., and Storch, J. (2004) The alpha-helical domain of liver fatty acid binding protein is responsible for the diffusion-mediated transfer of fatty acids to phospholipid membranes, *Biochemistry* **43,** 3600-3607.

Cowan, S.W., Newcomer, S.E., and Jones, T.A. (1993) Crystallographic studies on a family of cellular lipophilic transport proteins. Refinement of P_2 myelin protein and the structure determination and refinement of cellular retinol-binding protein in complex with all-trans-retinol, *J. Mol. Biol.* **230,** 1225-1246.

Davies, J.K., Thumser, A., and Wilton, D.C. (1999) Binding of Recombinant Rat Liver Fatty Acid-Binding Protein to Small Anionic Phospholipid Vesicles Results in Ligand Release: A Model for Interfacial Binding and Fatty Acid Targeting. *Biochemistry* **38,** 16932-16940.

Davies, J.K., Roberts, Hagan, R.M., and Wilton, D.C. (2002) Effect of charge reversal mutations on the ligand- and membrane-binding properties of liver fatty acid-binding protein, *J. Biol. Chem.* **277,** 48395-48402.

Delaglio, F., Grzesiek, S., Vuister, Z.W., Zhu, G., Pfeifer, J., and Bax, A. (1995) NMRPipe: a multidimensional spectral processing system based on UNIX pipes, *J. Biomol. NMR.* **6,** 277-293.

Dennis, E.A., Rhee, S.G., Billah, M.M., and Hanoun, Y.A. (1991) Role of phospholipase in generating lipid second messengers in signal transduction, *FASEB. J.* **5,** 2068-2077.

Epstein, L.F., Bass, N.M., Iwahara, S., Wilton, D.C. (1994) Immunological identity of rat liver cytosolic heme-binding protein with purified and recombinant liver fatty acid binding protein by western blots of two-dimensional gels. *Biochem. Biophys. Res. Comm.* **204,** 163-168.

Freeman, R. (1987) A Handbook of Nuclear Magnetic Resonance, *John Wiley and Sons*, New York.

Garbuzynskiy, S.O., Melnik, S., Lobanov, Y., and Oxana V. (2005) Comparison of X-ray and NMR structures: Is there a systematic difference in residue contacts between X-ray- and NMR-resolved protein structures? *Proteins* **60,** 139-147.

Gericke, A., Smith, E.R., Moore, D.J., Mendelsohn, E.R., and Storch J. (1997) Adipocyte fatty acid-binding protein: interaction with phospholipid membranes and thermal stability studied by FTIR spectroscopy, *Biochemistry* **36,** 8311-8317.

Glatz, J.F., Janssen, A.M., Baerwaldt, C.C., and Veerkamp, J.H. (1985) Purification and characterization of fatty-acid-binding proteins from rat heart and liver, *Biochim. Biophy. Acta.* **837,** 57-66.

Glatz, J.F., Vork, M.M., Cistola, D.P., and Van der Vusse, G.J. (1993) Cytoplasmic fatty acid binding protein: significance for intracellular transport of fatty acids and putative role on signal transduction pathways, *Prostagland. Leukot. Essent. Fatty Acids* **48**, 33-41.

Glatz, J.F., and Van der Vusse, G.J. (1996) Cellular fatty acid-binding proteins: their function and physiological significance, *Prog. Lipid Res.* **35,** 242-282.

Glover, K.J., Whiles, J.A., Wu.G., Yu, J., Deems, R., Struppe, J.O., Stark, R.E., Komives, E.A., and Vold, R.R. (2001) Structural evaluation of phospholipid bicelles for solution-state studies of membrane-associated biomolecules, *Biophys. J.* **81,** 2163-2171.

Grzesiek, S., and Bax, A. (1992) Correlating backbone amide and side chain resonances in larger proteins by multiple relayed triple resonance NMR, *J. Am. Chem. Soc.* **114,** 6291-6293.

Hagan, R., Davies, J., and Wilton, D.C. (2002) The Effect of Charge Reversal Mutations in The α- Helical Region of Liver Fatty Acid Binding Protein on The Binding of Fatty-Acyl CoA, Lysophospholipids and Bile Acids. *Mol. Cell. Biochem*. **239,** 55-60.

Hansen, M.R., Mueller. L., Pardi, A. (1998) Tunable alignment of macromolecules by filamentous phage yields dipolar coupling interactions. *Nat. Struct. Biol.* **5,** 1065-1074.

He, Y. (2000) NMR studies of rat liver fatty acid-binding protein (L-FABP), *Doctoral dissertation*, City University of New York.

He, Y., Yang, X., Wang, H., Estephan, R., Francis, F., Kodukula, S, Storch, J., and R.E. Stark, (2006) Solution-State Molecular Structure of Apo and Oleate-Liganded Liver Fatty Acid-Binding Protein, *to be submitted to Biochemistry.*

Herr, F.M., Aronson, J., and Storch, J. (1996) Role of portal region lysine residues in electrostatic interactions between heart fatty acid binding protein and phospholipid membranes, *Biochemistry* **35,** 1296-1303.

Hodsdon, M.E., Toner, J.J., and Cistola, D.P. (1996) ^{1}H, ^{13}C and ^{15}N assignments a and chemical shift-derived secondary structure of intestinal fatty acid-binding protein, *J. Biomol. NMR.* **6, 1**98-210.

Hodsdon, M.E., Ponder, J.W., and Cistola, D.P. (1996) The NMR solution structure of intestinal fatty acid-binding protein complexed with palmitate: application of a novel distance geometry algorithm, *J. Mol. Biol.* **264,** 585-602.

Hsu, K.T., and Storch, J. (1996) Fatty acid transfer from liver and intestinal fatty acid-binding proteins to membranes occurs by different mechanisms, *J. Biol. Chem.* **271,** 13317-13323.

Jakoby, M.G., Miler, K.R., Toner, J.J., Bauman, A., Cheng, L., Li, E., and Cistola, D.P. (1993) Ligand-protein electrostatic interactions govern the specificity of retinol- and fatty acid-binding proteins, *Biochemistry* **32,** 872-878.

Jing, W., Prenner, E.J., Vogel, H.J., Waring, A.J., Lehrer, R.I., Lohner, K. (2005) Headgroup structure and fatty acid chain length of the acidic phospholipids modulate the interaction of membrane mimetic vesicles with the antimicrobial peptide protegrin-1, *J. Pept. Sci.* **11,** 735-743.

Johnson, B.A., and Blevins, R.A. (1994) NMRView : a computer program for the visualization and analysis of NMR data, *J. Biomol. NMR.* **4,** 603-614.

Kaikaus, R.M., Bass, N.M., and Ockner, R.K. (1990) Functions of fatty acid binding proteins. *Experientia.* **46,** 617-630.

Kay, L.E., Xu, G.Y., Singer, A.U., Muhandiram, D.R., and Foreman-Kay, J.D. (1993) A gradient-enhanced HCCH-TOCSY experiment for recording side-chains ^{1}H and ^{13}C correlations in H2O samples of proteins, *J. Magn. Res. Ser*. B **101,** 333-337.

Kay, L.E., Xu, G.Y., and Yamazaki, T. (1994) Enhanced-sensitivity triple-resonance spectroscopy with minimal H_2O saturation, *J. Magn. Res. Ser. A* **109,** 129-133.

Ketterer, B., Ross-Mansell, P., and Whitehead, J.K. (1967) The isolation of carcinogen-binding protein from livers of rats given 4-dimethylaminoazobenzene, *Biochem. J.* **103,** 316-324.

Kim, H.K., and Storch, J. (1992) Mechanism of free fatty acid transfer from rat heart fatty acid-binding protein to phospholipid membranes. Evidence for a collisional process, *J. Biol. Chem.* **267,** 20051-20056.

Kim, H.K., Cistola, P., and Frieden, C. (1996) Intestinal fatty acid-binding protein: the structure and stability of a helix-less variant, *Biochemistry* **35,** 7553-7558.

Koppel, D.E. (1972) Analysis of macromolecular polydispersity in intensity correlation spectroscopy: the method of cumulants, *J. Chem. Phys.* **57,** 4814-4820.

Koradi, R., Billeter, M., and Wuthrich, K. (1996) MOLMOL: a program for display and analysis of macromolecular structures, *J. Mol. Graph.* **14,** 51-55.

Lalonde, J.M., Levenson, M., Roe, J.J., Bernolhr, D.A., and Banaszak, L. (1994) Adipocyte lipid-binding protein complexed with arachidonic acid. Titration calorimetry and X-ray crystallographic studies, *J. Biol. Chem.* **269,** 25339-25347.

Lawrence, J.W., Kroll, D.J., and Eacho, P.I. (2000) Ligand-dependent interaction of hepatic fatty acid binding protein with the nucleus, *J. Lipid Res.* **41**, 1390-1401.

Lehrer, R.I., Ganz, T. (1997) Endogenous vertebrate antibiotics. Defensins, protegrins, and other cysteine-rich antimicrobial peptides, *Ann. NY. Acad. Sci.* **797,** 228-239.

Lindberg, M., Biverståhl, H., Gräslund, A., and Mäler, L. (2003) Structure and positioning comparison of two variants of penetratin in two different membrane mimicking systems by NMR, *Eur. J. Biochem.* **270,** 3055-3063.

Lipsitz, R.S., and Tjandra, N. (2004) Residual dipolar couplings in NMR structural; analysis, *Annu. Rev. Biophys. Biomol. Struct.* **33,** 387-413.

Lu, J., Lin, C.L., Tang, C., Ponder, J.W., Kao, J.L., Cistola, D.P., and Li, E. (1999) The structure and dynamics of rat apo-cellular retinol-binding protein II in solution: comparison with the X-ray structure, *J. Mol. Biol.* **286**, 1179-1195.

Luchette, P.A., Vetman, T.N., Prosser, R.S., Hancock, R.E.W., Nieh, M.P., Glinka, C.J., Krueger, S., and Katsaras, J. (2001) Morphology of fast-tumbling bicelles: a small angle neutron scattering and NMR study, *Biochim. Biophys. Acta.* **1513,** 83-94.

Lucke, C., Lassen, D., Kreienkamp, H.J., Spener, F., and Ruterjans, H. (1992) sequence-specific 1H-NMR assignment and determination of the secondary structure of bovine heart fatty-acid-binding protein, *Eur. J. Biochem.* **210,** 901-910.

Mandal, P.K., and Majumdar, A. (2004) Acomprehensive discussion of HSQC and HMQC sequences, *Concepts. Magn. Resonan. Part A.* **20A,** 1-23.

Marley, J., Lu, M., and Bracken, C. (2001) A method for efficient isotopic labeling of recombinant proteins, *J. Biomol. NMR.* **20,** 71-75.

Mauffret, O., Tevanian, G., and Fermandian, S. (2002) Residual dipolar coupling constants and structure determination of large DNA duplexes, J. Biomol. NMR. **24**, 317-328**.**

Miller, K.R., and Cistola, D.P. (1993) Titration calorimetry as a binding assay for lipid-binding proteins, *Mol. Cell. Biochem.* **123,** 29-37.

Miyake, R., and Gross, R.W. (1992) Multiple phospholipase A_2 activities in canine vascular smooth muscle. *Biochem. Biophys. Acta.* **2,** 167-176.

Morris G, and Freeman, R. (1979) Enhancement of nuclear magnetic resonance signals by polarization transfer, *J. Am. Chem. Soc.* **101**, 760 –762.

Morrison, I.D., Grabowski, E.F., and Herb, C.A. (1985) Improved techniques for particle size determination by QELS, *Langmuir.* **1,** 496-501.

Myers-Payne, S.C., Hubbel, T., Pu, L., Schnutgen, F., Borchers, T., Wood, W.G., Spener, F., Schroeder, F. (1996) Isolation and characterization of two fatty acid binding proteins from mouse brain, *J. Neurochem.* **66,** 1648-1656.

Nagle, J.F., and Tristram-Nagle, S. (2000) Structure of lipid bilayers, *Biochim. Biophys. Acta.* **1469,** 159-195.

Nemecz. G., and Schroeder, F. (1991) Selective binding of cholesterol by recombinant fatty acid binding proteins. *J. Biol. Chem.* **266,** 17180-17186.

Newcomer, M.E., Jones, T.A., Aqvist, J., Eriksson, U., Rask, I., and Peterson, P.A. (1984) The three-dimensional structure of retinol-binding protein, *J. EMBO*. **7,** 1451-1454.

Norris, A. W., and Spector, A. (2002) Very long chain n-3 and n-6 polyunsaturated fatty acids bind strongly to liver fatty acid-binding protein. *J. Lip. Res.* **43,** 646-65.

Ockner, R.k., and Manning, J.A. (1972) A binding protein for fatty acids in cytosol of intestinal mucosa, liver, myocardium, and other tissues, *Science* **177,** 56-58.

Ottiger, M., Bax, A. (1998) Characterization of magnetically oriented phospholipid micelles for measurement of dipolar couplings in macromolecules. *J. Biomol. NMR.* **12,** 361-372.

Ottiger, M., Delaglio, F., and Bax, A.(1998) Measurement of J and dipolar couplings from simplified two-dimensional NMR spectra, *J. Magn. Reson.* **131,** 373-378.

Pääkkönen, K. (2003) Applications of residual dipolar couplings in structural studies of proteins, *Academic dissertation.* University of Helsinki.

Pecora, R. (1985) Dynamic Light Scattering: Applications of Photon Correlation spectroscopy. *Plenum Press,* New York.

Pervushin, K., Riek, R., Wider, G., and Wuthrich, K. (1997) Attenuated T_2 relaxation by mutual cancellation of dipole–dipole coupling and chemical shift anisotropy indicates an avenue to NMR structures of very large biological macromolecules in solution. *Proc. Natl Acad. Sci. USA.* **94, 1**2366–12371.

Poget, F., Cahill., S., and Girvin., M. (2007) Isotropic bicelles stabilize the functional form of a small multidrug-resistance pump for NMR structural studies, *JACS.* **129,** 2432-2433.

Prestegard, J. H., Al-Hashimi, H. M., Tolman, J. R. (2000) NMR structures of biomolecules using field oriented media and residual dipolar couplings *Q. Rev. Biophys.* **33,** 371-424.

Prestegard, J. H., Kishore, A.I.. (2001) Partial alignment of biomolecules: an aid to NMR characterization, Corr. *Opin. Chem. Biol.* **5,** 584-590.

Prestegard, J. H., Bougault, C.M., and Kishore, A.I. (2004) Residual dipolar couplings in structural determination of biomolecules, *Chem. Rev.* **104,** 3519-3540.

Prinden, C.F.M., Veerkamp, and J.H. (1996) Fatty acid binding and conformational stability of mutants of human muscle fatty acid-binding protein, *Biochem. J.* **314,** 253-260.

Prosser, R.S., Losonczi, J.A., and Shiyanovskaya, I.V. (1998) Use of a Novel Aqueous Liquid Crystalline Medium for High-Resolution NMR of Macromolecules in Solution, *J. Am. Chem. Soc*. **120,** 11010-11011.

Provencher, S.W. (1982) A constrained regularization method for inverting data represented by linear algebraic or integral equations, *Comput. Phys. Commun.* **27,** 213-228.

Purcell, E.M., Torrey, H.C, and Pound, R.V. (1946) Resonance absorption by nuclear magnetic moment in a solid, *Phys. Rev.* **69,** 37-38.

Rich, M.R., and Evans, J.S. (1996) Molecular dynamics simulations of adipocyte lipid-binding protein: effect of electrostatics and acyl chain unsaturation, *Biochemistry* **35,** 1506-1515.

Richieri, G.V., Ogata, R.T., and Kleinfeld, A.M. (1994) Equilibrium constants for the binding of fatty acids with fatty acid-binding proteins from adipocyte, intestine, heart, and liver measured with the fluorescent probe ADIFAB, *J. Bio. Chem.* **269,** 23918-23930.

Richieri, G.V., Low, P.J., Ogata, R.T., and Kleinfeld, A.M. (1997) Mutants of rat intestinal fatty acid-binding protein illustrate the critical role played by enthalpy-entropy compensation in ligand binding, *J. Biol. Chem.* **272,** 16737-16740.

Richieri, G.V, Ogata, R.T, Zimmermann, A.W, Veerkamp, J., and Kleinfeld, A. (2000) Fatty acid binding proteins from different tissues show distinct patterns of fatty acid interactions. *Biochem.* **39,** 7197-7130.

Roberts, G.C.K. (1993) NMR of macromolecules: a practical approach, *Oxford University Press,* Oxford, U.K.

Rolf, B., Oudenampsen-Kruger, E., Borchers, T., Faergeman, N.J., Knudsen, J., Lezius, A., and Spener, F. (1995) Analysis of the ligand binding properties of recombinant bovine liver-type fatty acid binding protein*, Biochim. Biophys. Acta.* **1259,** 245-253.

Ruckert, M., Otting., G. (2000) Alignment of Biological Macromolecules in Novel Nonionic Liquid Crystalline Media for NMR Experiments, *J. Am. Chem. Soc.* **122,** 7793-7797.

Sacchettini, J.C., Gordon, J.I., Banaszak, L.J. (1989) Refined apoprotein structure of rat intestinal fatty acid binding protein produced in Escherichia coli. *Proc. Natl. Acad. Sci. U S A* **86,** 7736-7740.

Sacchettini, J.C., Gordon, J.I., Banaszak, L.J. (1989) Crystal structure of rat intestinal fatty-acid-binding protein. Refinement and analysis of the Escherichia coli-derived protein with bound palmitate, *J. Mol. Biol*. **208,** 327-339.

Sacchettini, J.C., Hauft, S.M., Van Camp, S.L., Cistola, D.P., and Gordon, J.I. (1990) Developmental and structural studies of an intracellular lipid binding protein expressed in the ileal epithelium, *J. Biol. Chem.* **265,** 19199-19207.

Salzmann, M., Pervushin, K., Wider, G., Senn, H., and Wuthrich, K. (1998) TROSY in triple-resonance experiments: new perspectives for sequential NMR assignment of large proteins, *Proc. Natl Acad. Sci. USA.* **95,** 13585–13590.

Sass, J., Cordier, F., Hoffmann, A., Rogowski, M., Cousin, A., Omichinski, J. G., Lowen, H., and Grzesiek, S. (1999) Purple Membrane Induced Alignment of Biological Macromolecules in the Magnetic Field, *J. Am. Chem. Soc.* **121,** 2047-2055.

Sass, J., Musco, G., Stahl, S.J., Wingfield, P.T., and Grzesiek, S. (2000) Solution NMR of proteins within polyacrylamide gels: diffusional properties and residual alignment by mechanical stress or embedding of oriented purple membranes*, J. Biomol. NMR.* **18,** 303-309.

Schmitz, K. S. (1990) An Introduction to Dynamic Light Scattering by Macromolecules. *Academic Press,* Boston.

Slichter, C.P. (1978) Principles of Magnetic Resonance. Springer Publishing, New York.

Sorof, S. (1994) Modulation of mitogenesis by liver fatty acid binding protein, *Cancer. Metastasis. Rev.* **13,** 317-336.

Sprecher, H. (2000) Metabolism of highly unsaturated n-3 and n-6 fatty acids. *Biochim. Biophys. Acta.* **1486,** 219-231.

Stafford, R.E., and Dennis, E.A. (1988) Interfacial properties and critical micelle concentration of lysophospholipids. *Colloid. Surfaces* **28,** 5113-5120.

Storch, J. (1993) Diversity of fatty acid-binding protein structure and function: studies with fluorescent ligands, *Mol. Cell. Biochem.* **123,** 45-53.

Storch, J., Herr, F.M., and Hsu, K.T. (1996) The role of membranes and intracellular binding proteins in cytoplasmic transport of hydrophobic molecules, *Comp. Biochem. Physiol.* **115,** 333-339.

Storch, J., and Thumser, A.E. (2000) The fatty acid transport function of fatty acid-binding proteins, *Biochim. Biophys. Acta.* **1486,** 28-44.

Struppe, J., Whiles, J.A., and Vold, R.R. (2000) Acidic phospholipid bicelles: a versatile model membrane system, *Biophys. J.* **78,** 281-289.

Styliani, H., Muller-Eberhard, U. (1985) A protein of the Z class of the liver cytosolic proteins in the rat that preferentially binds heme. *J. Biol. Chem.* **260,** 14521-14528.

Tan, N.S., Shaw, N.S., Venckenbosch, N., Liu, P., Yasmin, R., Desvergne, B., Wahli, W., Noy, N. (2002) Selective cooperation between fatty acid binding proteins and peroxisome proliferator-activated receptors in regulating transcription, *Mol. Cell. Biol.* **22,** 5114-5127.

Thompson, J., Winter, N., Terwey, D., Bratt, J., and Banaszak, L. (1997) The crystal structure of the liver fatty acid-binding protein. A complex with two bound oleates, *J. Biol. Chem.* **272,** 7140-7150.

Thompson, J., Ory, J., Reese-Wagner, A., and Banaszak, L. (1999) The fatty acid binding protein-comparison of cavity properties of intracellular lipid-binding proteins, *Mol. Cellular. Biochem.* **192,** 9-16.

Thompson, J., Reese-Wagoner, A., and Banaszak, L. (1999) Liver Fatty Acid Binding Protein: Species Variation and The Accommodation of Different Ligands. *Biochem. Biophys. Acta.* **1441,** 117-130.

Thumser, A.E., Voysey, J.E., and Wilton, D.C. (1994) The binding of lysophospholipids to rat liver fatty acid-binding protein and albumin, *Biochem. J.* **301,** 801-806.

Thumser, A.E., Evans, C., Worral, A.F., and Wilton, D.C. (1994) Effect on ligand binding of arginine mutations in recombinant rat liver fatty-acid binding protein. *Biochem. J.* **297,** 103-107.

Thumser, A.E, and Wilton, D.C. (1995) The binding of natural and fluorescent lysophospholipids to wild-type and mutant rat liver fatty acid-binding protein and albumin, *Biochem. J.* **307,** 305-311.

Thumser, A.E, and Wilton, D.C. (1996) The binding of cholesterol and bile salts to recombinant rat liver fatty acid-binding protein. *Biochem. J.* **320,** 729-733.

Thumser, A.E., and Storch, J. (2000) Liver and intestinal fatty acid-binding proteins obtain fatty acids from phospholipid membranes by different mechanisms, *J. Lipid Res.* **41,** 647-656.

Tipping, E., Ketterer, B., Christodoulides, L., Enderby, G. (1976) The interactions of haem with ligandin and Aminoazo-dye-binding protein A. *J. Biochem.* **157,** 461-467.

Tipping, E., and Ketterer, B. (1981) The influence of soluble binding proteins on lipophile transport and metabolism in hepatocytes, *Biochem. J.* **195,** 441-452.

Tjandra, N., Bax, A. (1997) Direct measurement of distances and angles in biomolecules by NMR in a dilute liquid crystalline medium. *Science* **278,** 1111- 1114.

Tycko, R., Blanco, F.J., and Ishii, Y. (2000) Alignment of Biopolymers in Strained Gels: A New Way To Create Detectable Dipole-Dipole Couplings in High-Resolution Biomolecular NMR, *J. Am. Chem. Soc.* **122,** 9340-9340.

Van Holde, K., Johnson, W.C., and Ho, P.S. (1998) Principle of physical Biochemistry, *Prentice Hall,* Upper Saddle River, New Jersey.

Vancura, A., Haldar, D. (1992) Regulation of mitochondrial and microsomal phospholipid synthesis by liver fatty acid-binding protein, *J. Biol. Chem.* **5,** 14353-14359.

Vincent, S.H., and Muller-Ebberhard. (1985) A protein of the Z class of liver cytosolic proteins in the rat that preferentially binds heme, *J. Biol. Chem.* **260,** 14521-14528.

Vold, R.R., Prosser, S.R., and Deese, A.J. (1997) Isotropic solutions of phospholipid bicelles: a new membrane mimetic for high-resolution NMR studies of polypeptides, *J.Biomol. NMR.* **9,** 329-335.

Vorum, H., Brodersen, R., Kragh-Hansen, U., and Pedersen, A.O. (1992) Solubility of long-chain fatty acids in phosphate buffer at pH 7.4, *Biochim. Biophys. Acta.* **1126,** 135-142.

Wang, H., He, Y., Hsu, K.T., Magliocca, J.F., Storch, J., and Stark, R.E. (1998) ^{1}H, ^{15}N, and ^{13}C resonance assignments and secondary structure of apo liver fatty acid-binding protein, *J. Biomol. NMR.* **12,** 197-199.

Wang, H., He, Y., Kroenke, C.D, Kodukula, S., Palmer, A., Storch, J., and Stark, R.E. (2002) Titration and exchange studies of liver fatty acid-binding protein with ^{13}C-labeled long-chain fatty acids, *Biochemistry* **12,** 197-199.

Weisiger, R.A., and Zucker, S.D. (2002) Transfer of fatty acids between intracellular membranes: roles of soluble binding proteins, distance, and time, *Am. J. Physiol. Gastrointest. Liver Physiol.* **282,** G105-15.

Whiles, J.A., Brasseur, R., Glover, K.J., Melacini, G., Komives, E.A., and Vold, R.R. (2001) Orientation and effects of mastoparan X on phospholipid bicelles, *Biophys. J.* **80,** 280-293.

Wilkinson, T.C., Wilton, D.C. (1987) Studies on fatty acid-binding proteins. The binding properties of rat liver fatty acid-binding protein, *Biochem. J.* **247,** 485-488.

Wilson, M.D., Rudel, L.L. (1994) Review of cholesterol absorption with emphasis on dietary and biliary cholesterol, *J. Lipid Res.* **35,** 943-955.

Wishart, D.S., Bigam.C.G., Yao.J., Abildgaard, F., Dyson, H.J., Oldfield, E., Markley, J.L., and Sykes, B.D. (1995) 1H, 13C and 15N chemical shift referencing in biomolecular NMR, *J. Biomol, NMR* **6,** 135-140.

Wolfrum, C., Borrman, C.M., Börchers, T., and Spener, F. (2001) Fatty acids and hypolipidemic drugs regulate peroxisome proliferator activated receptors α- and γ-mediated gene expression via liver fatty acid binding protein: a signaling path to the nucleus, *Proc. Natl. Acad. Sci. USA.* **98,** 2323-2328.

Wuthrich, K., Brown. R.L., and Bosch, C. (1980) Conformational studies of lipid-bound polypeptides by elucidation of proton-proton cross-relaxation networks, *Biochem. Biophys. Res. Commun.* **95,** 1504-1509.

Xu, Y., Yushmanov, V.E., Tang, P. (2002) NMR Studies of Drug Interaction with Membranes and Membrane-Associated Proteins, *Bioscience Reports* **22,** 175-196.

Young, A.C., Scapin, G., Kromminga, A., Patel, S.B., Veerkamp, J.H., and Sacchettini, J.C. (1994) Structural studies on human muscle fatty acid binding protein at 1.4 A resolution: binding interactions with three C18 fatty acids, *Structure* **6,** 523-534.

Zhang, F., Lucke, C., Baier, L.J., Sacchettini, J.C., and Hamilton, J.A. (1997) Solution structure of human intestinal fatty acid binding protein: implications for ligand entry and exit, *J. Biomol. NMR* **3,** 213-228.

Zscheische, W., Kleine, A.H., Spitzer, E., Veerkamp, J.H., and Glatz, J.C.E. (1995) Histochemical localization of heart-type fatty-acid binding protein in human and murine tissues, *Histochem. Cell. Biol.* **103,** 147-156.